Development of an Electrochemical Sensor for Detection of 2,4-Dinitrotoluene

A DISSERTATION
SUBMITTED TO THE FACULTY OF THE GRADUATE SCHOOL
OF THE UNIVERSITY OF MINNESOTA
BY

Eric James Olson

IN PARTIAL FULFILLMENT OF THE REQUIREMENTS
FOR THE DEGREE OF
DOCTOR OF PHILOSOPHY

Philippe Bühlmann, Adviser

July 2012

Acknowledgements

During the course of my doctoral work, I have received the assistance and support from the following people:

First and foremost, I am truly indebted to my adviser, Philippe Bühlmann. His undying dedication to science and insatiable thirst for knowledge has been an inspiration to me over the last five years. More than that, the guidance, support, and, most importantly, friendship that Phil has provided has greatly benefitted my development both as a person and as a scientist.

I must give special thanks to Dr. Paul Boswell and Dr. Scott Thorgaard for helping me get started in the lab and teaching me best practices for performing electrochemistry experiments.

I would also like to thank the following people for their specific contributions to the work described in this thesis:

Our collaborator, Professor Andreas Stein, for the many hours that he has spent discussing our collaborative research. His insight and unique point of view has been extremely useful.

Dr. Bradley Givot at the 3M Corporate Research Laboratory for measuring the dielectric spectra presented in Chapter 2.

Dr. Letitia Yao of the University of Minnesota Chemistry NMR Lab for her assistance with measuring the self-diffusion coefficient of perfluoro(methylcyclohexane) in Chapter 2.

Peter Ness of the University of Minnesota Physics Machine Shop for his assistance in designing the microcell described in Chapter 3.

Teng Xiong for performing the initial work that led us to question the traditional interpretation of the interaction of 2,4-dinitrotoluene with amines.

Amanda Zeise and Jing-Lei Zhang for their preliminary contributions to the UV-Vis studies presented in Chapter 4.

Professor Christopher Cramer for performing the DFT studies in Chapter 4.

Melissa Fierke for the synthesis, chemical modification, and characterization of the three-dimensionally ordered macroporous carbon electrodes used for the selective detection of 2,4-dinitrotoluene.

I would also like to thank my colleagues in the Bühlmann research group for their friendship and support. The people that I have had the opportunity to work with over the last five years have made my graduate studies a truly enjoyable experience.

Lastly, I owe a great deal to my family. Without their love, devotion, and support, I would not be where I am today.

Dedication

This dissertation is dedicated to Amber Rose Olson.

Table of Contents

List of Tables

List of Figures

List of Symbols and Abbreviations

3DOM	3-dimensionally ordered macroporous
A	area
A	absorbance
a_x	activity of species x
$BArF_{104}^-$	tetrakis[3,5-bis(perfluorohexyl)phenyl]borate
CV	cyclic voltammogram
C_x	concentration of species x
d	optical path length
DFT	density functional theory
DMF	*N,N*-dimethylformamide
DMSO	dimethyl sulfoxide
DNT	2,4-dinitrotoluene
DOSY	diffusion ordered NMR spectroscopy
DSC	differential scanning calorimetry
D_x	diffusion coefficient of species x
E	electrical potential
E^o	standard reduction potential
$E^{o'}$	formal reduction potential
F	Faraday's constant
f	mole fraction
Fc	ferrocene
Fc^+	ferrocenium
FC-72	perfluorohexanes
i	current
i_p	peak current
k_b	backward rate constant
k_B	Boltzmann constant

K_{Eq}	equilibrium constant
k_f	forward rate constant
k^o	standard heterogeneous rate constant
K_p	precursor formation constant
l	length
n	number of electrons
NBu_4^+	tetrabutylammonium
NEt_4^+	tetraethylammonium
NHE	normal hydrogen electrode
NHx_4^+	tetrahexylammonium
PMMA	poly(methyl methacrylate)
PVC	poly(vinyl chloride)
q	charge
R	ideal gas constant
r_o	radius of an electrode
R_u	uncompensated resistance
r_x	effective radius of species x
SWV	square wave voltammetry
T	absolute temperature
t	time
TNT	2,4,6-trinitrotoluene
u_i	mobility of ion i
UME	ultramicroelectrode
XPS	X-ray photoelectron spectroscopy
z_i	formal charge of ion i
ΔG	Gibbs free energy
ΔG^o	standard Gibbs free energy
Γ	surface excess
α	transfer coefficient

ε	molar absorptivity
ε_∞	infinite frequency dielectric constant
$\tilde{\varepsilon}(\nu)$	frequency-dependent dielectric permittivity
$\varepsilon'(\nu)$	real component of the frequency-dependent dielectric permittivity
$\varepsilon''(\nu)$	dielectric absorption
ε_s	static dielectric constant
η	viscosity
κ_{EL}	adiabicity parameter
ν	scan rate
τ_D	Debye solvent relaxation time
τ_L	longitudinal solvent relaxation time

List of Publications

The results presented in this thesis have been published in the following:

Olson, E. J.; Boswell, P. G.; Givot, B. L.; Yao, L. J.; Bühlmann, P. "Electrochemistry in Media of Exceptionally Low Polarity: Voltammetry with a Fluorous Solvent" *Journal of Electroanalytical Chemistry*, **2010**, 639, 154-160.

Olson, E. J.; Bühlmann, P. "Minimizing Hazardous Waste in the Undergraduate Analytical Laboratory: A Microcell for Electrochemistry" *Journal of Chemical Education*, **2010**, 87, 1260-1261.

Olson, E. J.; Xiong, T. T.; Cramer, C. J.; Bühlmann, P. "Interaction of a Weakly Acidic Dinitroaromatic with Alkylamines: Avoiding the Meisenheimer Trap" *Journal of the American Chemical Society*, **2011**, 133, 12858-12865.

Olson, E. J.; Bühlmann, P. "Getting More out of a Job Plot: Determination of Reactant to Product Stoichiometry in Cases of Displacement Reactions and *n:n* Complex Formation" *Journal of Organic Chemistry* **2011**, 76, 8406-8412.

Fierke, M. A.; Olson, E. J.; Bühlmann, P.; Stein, A. "Receptor-Based Detection of 2,4-Dinitrotoluene using Modified Three-Dimensionally Ordered Macroporous Carbon Electrodes" *Manuscript Submitted.*

1 CHAPTER ONE

Introduction

1.1 Chapter Overview

In this chapter, the background and underlying theory of this thesis are described. Since this work builds a foundation for the selective recognition and sensing of 2,4-dinitrotoluene (DNT), the importance of detecting this molecule is first introduced. Ultimately, the intended sensor will rely upon electrochemical detection of DNT; therefore, the basics of electron transfer are then described. Once a foundation on electron transfer at an electrode has been built, the concept of cyclic voltammetry will then be introduced. The theories that govern voltammetry of an adsorbed species are presented before the more complicated concepts behind voltammetry of a dissolved species are introduced. Because the ultimate goal of this work is to develop a sensor based on low-polarity sensing media, a brief primer on the consequences of performing electrochemistry with solutions containing a low electrolyte concentration is then presented. Finally, the remainder of this thesis is briefly outlined.

Because the work presented in this thesis covers a wide range of concepts, this introduction is not meant to be comprehensive for all chapters. Instead, this introduction focuses largely on the theory, design and interpretation of electrochemical experiments. A more detailed background for the research presented in each chapter will be provided.

There are several good reference books that give far more detailed backgrounds than could possibly be presented in this thesis. For an extremely technical introduction to electrochemistry and the various techniques that are available, the author recommends the book *Electrochemical Methods: Fundamentals and Applications, 2nd Edition* by Allen J. Bard and Larry R. Faulkner.[1] The books *Electrochemistry for Chemists, 2nd Edition* by Donald T. Sawyer, Andrzej Sobkowiak, and Julian L. Roberts, Jr.[2] and *Nonaqueous Electrochemistry* edited by Doron Aurbach[3] provide less technical application-based introductions to a variety electrochemistry techniques, including those that are utilized in this work. Lastly, the book *Binding Constants: The Measurement of Molecular Complex Stability* by Kenneth A. Connors[4] is an excellent reference for methods of determining the binding complex of a host–guest system.

1.2 2,4-Dinitrotoluene as an Analyte

Development of a rapid and sensitive method for detecting explosives is a major concern for national security, military, and environmental remediation applications.[5] One of the most commonly used industrial and military explosives worldwide is 2,4,6-trinitrotoluene (TNT).[5,6] Commercially, TNT (**1**) is produced by the three-step nitrification of toluene according to Figure 1.[7]

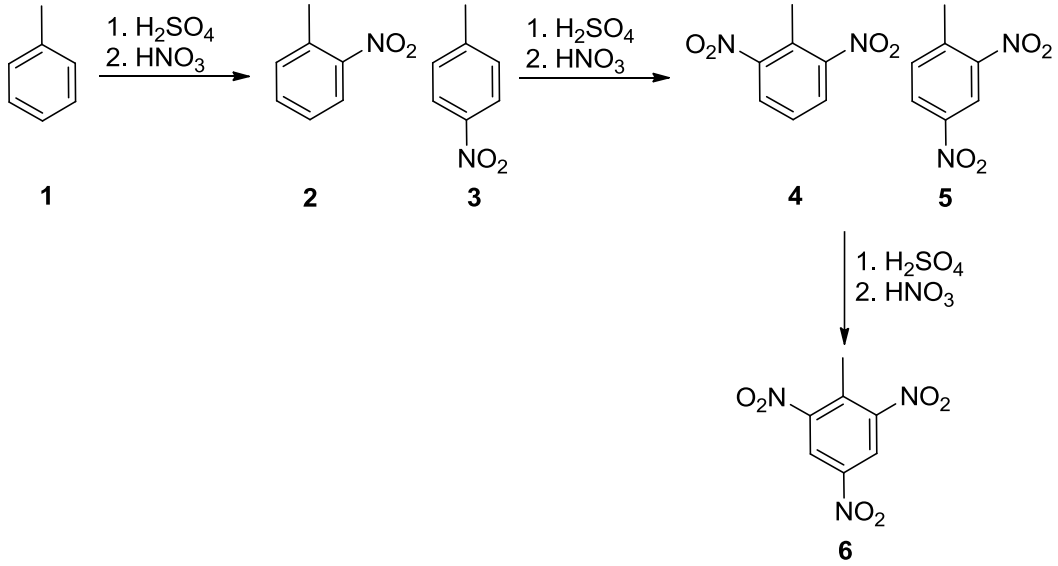

Figure 1: Synthetic scheme for the production of TNT

There has been a wide variety of sensing schemes for TNT presented in the literature;[8-13] however, due to the extremely low volatility of TNT makes direct detection of TNT rather difficult. Fortunately, incomplete nitrification of dinitrotoluenes **4** and **5** during TNT synthesis combined with poor purification of synthesized TNT results in nearly all commercially-produced TNT containing these byproducts.[7] Many efforts to detect TNT-based devices focus upon the detection of 2,4-dinitrotoluene (DNT) rather than TNT itself. In fact, dogs that are trained to smell TNT-containing devices have been shown to smell DNT rather than TNT.[14] There have been many approaches reported for DNT detection, including photoluminescence and fluorescence quenching,[15,16] detection

of reduction or degradation products,[17-19] vapor adsorption on a modified microcantilever,[20] electronic noses and sniffers,[5,21] electrochemical impedance detection,[22] and detection by combining capillary electrophoresis and electrochemical detection with a porous carbon-modified electrode.[23] For the purpose of miniaturization, electrochemical detectors are attractive as sensing devices. [22-27] Fortunately, the electroactive nature of the nitro substituents allows for electrochemical detection of DNT at relatively modest potentials.[28] Indeed, several explosive sensing devices that rely upon electrochemical detection have been presented in the literature.[18,22-25,29,30] This research focuses upon first developing a scheme for selective molecular recognition of DNT and adapting that scheme to chemically modify an electrode for electrochemical detection.

1.3 An Introduction to Electrochemistry

Consider the electrode reaction:

$$O + n\,e^- \rightleftharpoons R \tag{1}$$

where O and R are Oxidized and Reduced species, respectively, and n is the number of electrons transferred. Charge signs have been omitted on O and R for simplicity although one or both of these species would clearly carry a formal charge. For chemical systems that are coupled such as this, O and R are commonly referred to as a *redox couple*. The reaction Gibbs Free Energy (ΔG) of this reaction is then given by:

$$\Delta G = \Delta G^o + RT \ln\left(\frac{a_R}{a_O}\right) \tag{2}$$

where ΔG^o is the standard Gibbs Free Energy for Reaction 1, R is the ideal gas constant, T is the absolute temperature and a_x is the activity of species x. Dividing both sides of Equation 2 by $-nF$, where F is Faraday's constant, results in:

$$E = E^o - \frac{RT}{nF} \ln\left(\frac{a_R}{a_O}\right) \tag{3}$$

since $E = -\Delta G/nF$ and $E^o = -\Delta G^o/nF$ where E signifies the electrical potential at the electrode and E^o is the standard potential of reaction 1 versus a normal hydrogen electrode (NHE). This familiar result is the Nernst equation. Extracting activity coefficients from the logarithmic term in Equation 3 results in:

$$E = E^{o'} - \frac{RT}{nF}\ln\left(\frac{C_{\mathrm{R}}}{C_{\mathrm{O}}}\right) = E^{o'} - 0.059\log\left(\frac{C_{\mathrm{R}}}{C_{\mathrm{O}}}\right) \quad \{\text{For } T = 25\,^{\circ}\mathrm{C}\} \tag{4}$$

where C is the concentration of the species at the electrode and $E^{o'}$ is the formal reduction potential of the couple.

1.3.1 The Electrochemical Cell

The relationship between concentration and potential presented in Equation 4 provides the fundamental basis for determining the ratio between O and R in any solution. Should an electrically conducting material (an *electrode*) be inserted into a solution containing fixed concentrations of O and R, such as depicted in Figure 2a, the potential obtained at the interface between the electrode and solution will be determined by the relative concentrations of O and R.

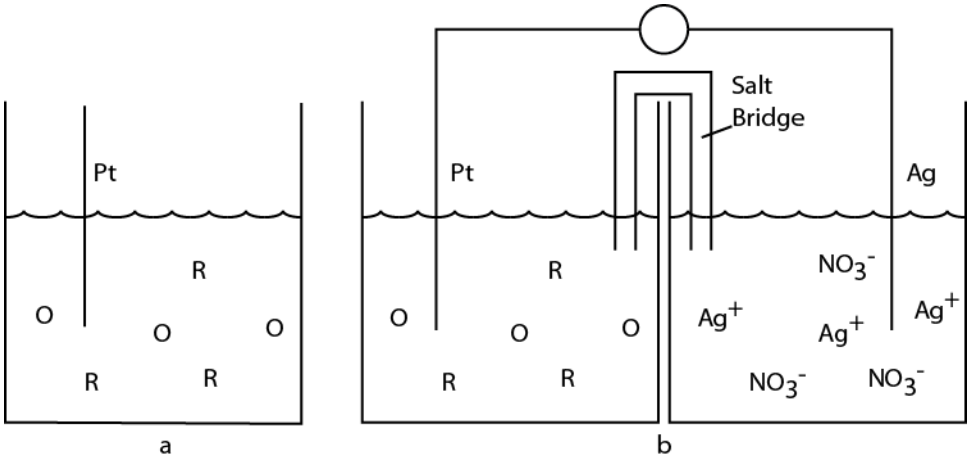

Figure 2: Depiction of an electrochemical half-cell (a) and a full electrochemical cell (b)

Unfortunately, because an electrical potential E is measured as the difference between two points in a circuit, it is impossible to directly measure the electrical potential of the platinum wire in Figure 2a. Instead, the electrical potential must be measured over a complete electrical circuit. An example of a completed circuit, as would be used in an electrochemistry experiment, is depicted in Figure 2b. This complete circuit is commonly referred to as an *electrochemical cell*. In this example, the compartment on the left contains a platinum electrode immersed in the generic O and R redox couple from Equation 1 while the compartment on the right contains a silver electrode immersed into a silver nitrate solution.

In this example, a *salt bridge* is used to provide a *liquid junction* between the two compartments. The purpose of the salt bridge is to allow ionic conductivity between the two half-cells while preventing the cross-contamination of the cells by slowing the transport of solutes through across the junction. This junction may take many forms, such as a liquid-filled capillary, an agar gel matrix, or as is the case for the work presented in this thesis, a piece of fritted glass. Ideally, the liquid junction does not contribute to the overall potential of the system; in practice, the contribution is either kept extremely small or corrected by calculation.[31] Also, in some of the experiments performed in this work, a liquid junction is not necessary, as will be discussed.

Treating the right compartment as a chemical reaction of the form presented in Equation 1 gives

$$Ag^+ + e^- \rightleftharpoons Ag \tag{5}$$

The overall chemical reaction occurring in the electrochemical cell is thus

$$Ag + O \rightleftharpoons Ag^+ + R \tag{6}$$

This reaction is referred to as the *cell reaction*. Because Equations 1 and 5 each make up half of the cell reaction, these reactions are commonly referred to as *half-reactions*.

To make the depiction of electrochemical cells easier, it is common to utilize what is known as *line notation*. For the cell shown in Figure 2, the line notation would be

$$\text{Pt}|x \text{ mM O}, y \text{ mM R}||z \text{ mM } AgNO_3|\text{Ag} \tag{7}$$

In this notation, a single vertical bar indicates a phase boundary (such as the boundary between a metal and an aqueous solution) a comma separates two species in the same solution, and a double vertical bar indicates a liquid junction (such as a salt bridge).

If the two electrodes are then connected to a high-impedance voltmeter, the overall difference between the interfacial potential of the two electrodes may be measured. This potential is referred to as the *open circuit potential* and is presented in volts (V). In a typical experiment, the interfacial potential of only one of the electrodes is of interest (rather than the overall cell potential). This electrode is generally referred to as the *working electrode.* Fortunately, maintaining one half-cell under identical controlled conditions from one experiment to the next allows for standardization of the cell potential. This half-cell is referred to in such experiments as the *reference electrode*. In fact, the right half-cell in Figure 2 is a cell depiction of a Ag/Ag^+ reference electrode, commonly used for experiments in nonaqueous solutions (see Section 1.3.2).

1.3.2 The Reference Electrode

In an electrochemical cell, the role of the reference electrode is to provide a stable potential against which the working electrode may be measured and reported.[32] While many specific configurations exist, all reference electrodes fall into one of three classes: electrodes of the first kind, electrodes of the second kind, and quasi- or pseudo-reference electrodes.

A reference electrode of the first kind consists of a metal or soluble species in electrochemical equilibrium with its soluble oxidized species. In a reference electrode of this type, the reference potential is determined by the phase boundary potential between the electroactive species and its oxidized counterpart. The most notable example of this type is the *normal hydrogen electrode* (NHE) as this reference electrode is the basis for which the standard reduction potential of all other redox couples is reported. The NHE half-cell is as follows:

$$Pt/H_2\ (1\ atm)/H_2O,\ H^+\ (activity\ =1) \qquad (8)$$

Because use of a NHE involves maintaining a partial pressure of H_2 of 1 atm, the experimental use of a NHE is quite challenging. Therefore, experimental measurements and the potentials reported therein are generally based upon other types of reference electrodes. In organic samples, a commonly used reference electrode of the first type consists of a Ag wire inserted into a solution of a known concentration of Ag^+ (paired with a lipophilic anion).[1,3,33] When this reference is utilized, potentials are typically reported with respect to Ag/*n* mM Ag^+. To minimize the liquid junction potential arising from a concentration gradient of ionic species, the inner filling solution is typically prepared to be as close in composition to the sample solution as possible. Because much of the electrochemistry work presented in this thesis involves organic solvents, a Ag/10 mM Ag^+ reference electrode is used extensively.

A reference electrode of the second kind consists of a metal coated by and in equilibrium with its sparingly soluble salt. Two very common examples of this kind are the calomel electrode ($Hg/HgCl_2$) and the Ag/AgCl electrodes. The Ag/AgCl electrode is constructed by coating a Ag wire with AgCl and inserting that wire into a saturated solution of KCl. This reference electrode is widely used due to its relatively small temperature dependence along with being much less toxic than the calomel electrode. The internal solution of this type of reference electrode is typically aqueous rather than organic due to the large formation constant of species such as $AgCl_2^-$ in typical organic solvents used for electrochemistry, such as acetonitrile. For this reason, either an electrode of the first kind or a quasi-reference electrode is commonly used for non-aqueous solutions. Because all of the electrochemistry work presented in this thesis is performed with nonaqueous solutions, this type of reference electrode is not used in this work.

Quasi-reference electrodes, also referred to as *pseudo-reference electrodes*, consist simply of a metal wire inserted into the solution of interest. These types of electrodes are especially handy for solvents for which there exists no good reference electrode. Moreover, (and especially pertinent to this work) the small size of a bare wire makes

quasi-reference electrodes extremely well suited for samples of extremely small volumes. Because the Nernst equation is poorly defined for a metal inserted into a solution without an active redox couple, the potential of the quasi-reference electrode is extremely difficult to predict. Fortunately, the potential of a quasi-reference is often reproducible for the same sample solution and rather stable over the course of a typical experiment.[3] Often, results obtained using a quasi-reference electrode are calibrated against the ferrocene/ferrocenium (vs. Fc/Fc^+) redox couple, assuming that the standard reduction potential of the system does not change appreciably with changes in solvent.[34]

1.3.3 Application of an External Voltage

If a variable voltage source is now introduced into the electrochemical cell between the two electrodes, as shown in Figure 3, the potential of the working electrode may be perturbed.

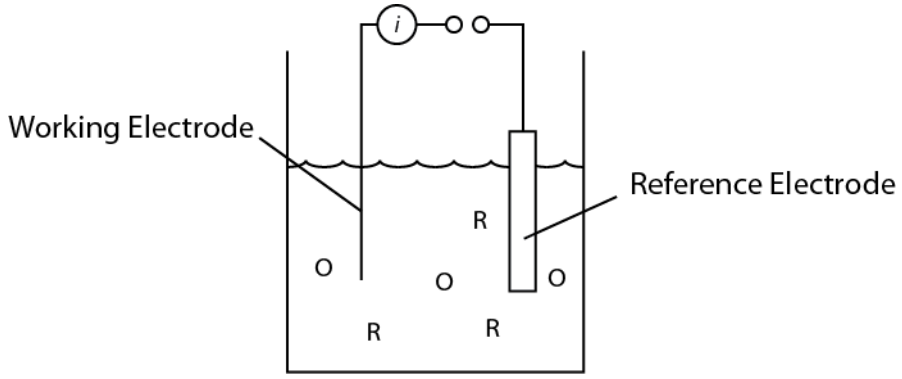

Figure 3: A two electrode cell with a variable voltage source and ammeter added to the circuit.

By varying the potential at the working electrode/solution boundary, the ratio of C_R to C_O must also adjust such that the Equation 4 remains true. This change in concentration may be monitored by the passage of electrons either into or out of the working electrode. Under conditions where electrons pass *into* the electrode (R is being oxidized to O) the working electrode is considered an *anode* and the current is thus *anodic.* By contrast, if

electrons are passing from the working electrode into the solution (O is being reduced to R), the electrode is considered a *cathode* and the current is thus considered *cathodic.* In electrochemistry, cathodic currents are generally considered to be positive.

While the two electrode cell depicted in Figure 3 is suitable for many techniques involving either constant applied voltage between the two electrodes or monitoring the interfacial potential at the working electrode, it is not suitable for techniques that require precise control over the potential of the working electrode. This is because, as current starts to flow through the reference electrode, the potential of the reference electrode often changes to accommodate this flow. Therefore, for techniques that require precisely controlling the potential of the working electrode while passing a significant amount of current, a third electrode (referred to as the *auxiliary electrode*) must be added to the system.

In a three-electrode setup such as shown in Figure 4, the three electrodes immersed in solution are connected to a device known as a *potentiostat*.

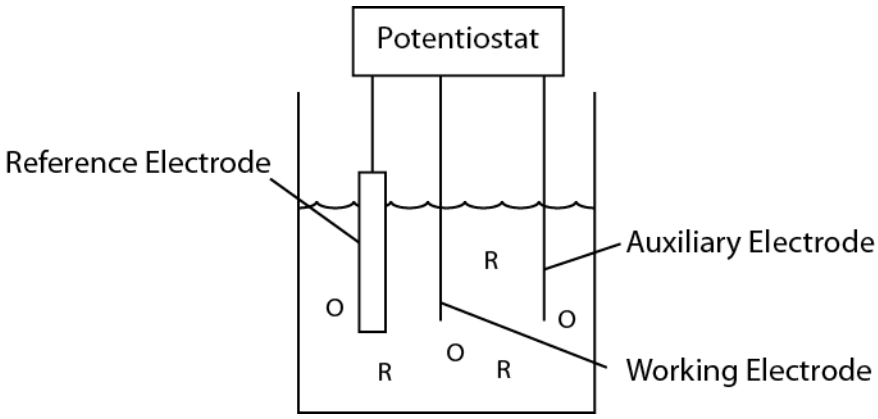

Figure 4: Depiction of a three-electrode setup.

Instruments of this type allow for the controlled adjustment of the potential between the working and reference electrode. Upon reaching potentials at which oxidation or reduction occurs at the working electrode current is passed through the auxiliary electrode to complete the circuit. Because the input impedance (electric resistance) of the

reference electrode connection is made very high in such instruments, the amount of current that passes through the reference electrode is negligible. In this way, a stable reference potential is maintained regardless of current flowing at the working electrode. Provided that the electrochemical process occurring at the auxiliary electrode does not interfere with the overall measurement, the chosen material for the auxiliary electrode is unimportant. Generally, a high surface area of a good electron conductor is chosen; for example, in the work presented in this thesis, a coil of Pt wire is used.

1.3.4 Cyclic Voltammetry

Now that a method for precisely measuring and controlling the interfacial potential at a working electrode has been established, more complex experiments involving perturbing the potential of the working electrode may be introduced. There is a wide variety of techniques available; however, cyclic voltammetry is one of the most commonly used for mechanistic and kinetic interrogation of electrode reactions.[1,31,35] In this technique, the potential is swept in a linear manner with respect to time and the current monitored during the potential sweep. That is, the applied potential at the working electrode at time t is defined by the relations

$$E_{\text{Applied}} = E_{\text{Initial}} + \nu t \quad (E_{\text{Applied}} < E_{\text{Switch}})$$

$$E_{\text{Applied}} = E_{Switch} - \nu(t - t_{\text{Switch}}) \quad (E_{\text{Applied}} > E_{\text{Switch}}) \tag{9}$$

where E_{Applied} is the potential applied to the working electrode, E_{Initial} is the applied potential at the start of the experiment, ν is the rate at which the potential is swept E_{Switch} is the potential at which the scan is reversed, and t_{Switch} is the time at which the potential sweep is reversed. The resulting applied potential is plotted with respect to time in Figure 5.

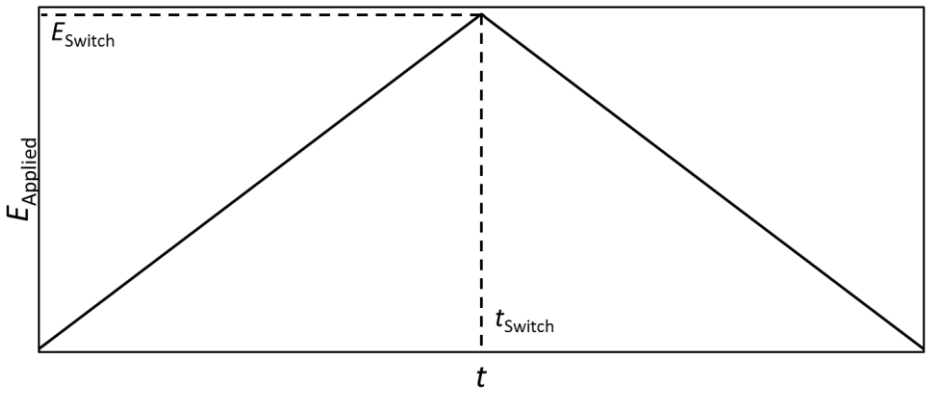

Figure 5: Graphical relationship between applied potential and time in a cyclic voltammetry experiment.

While only the first cycle is shown in Figure 5, cyclic voltammetry experiments often involve cycling the potential range several times. Before introducing cyclic voltammetry of a species dissolved in solution, it is beneficial to introduce the theory for cyclic voltammetry of an adsorbed species, as diffusion does not need to be considered for this situation.

1.3.4.1 Cyclic Voltammetry of an Adsorbed Species

In this section, the cyclic voltammetry of an electroactive species that is adsorbed to the surface of an electrode is considered. For simplicity, the rate at which electrons may be transferred between the electrode and the adsorbed species is extremely fast relative to the scan rate of the experiment. Sluggish electron transfer will be considered only for the case of dissolved species (Section 1.3.4.2).

For surface adsorbed species, it is customary to report the concentration of a species in surface excess:[36] Thus, the Nernst equation may be rewritten as

$$E = E^{o'} - \frac{RT}{nF} \ln\left(\frac{\Gamma_R}{\Gamma_O}\right) \tag{10}$$

where Γ_x is the surface coverage of species x. Solving Equation 10 for Γ_R/Γ_O:

$$\frac{\Gamma_R}{\Gamma_O} = e^{-\frac{nF}{RT}(E-E^{o'})} \tag{11}$$

Assuming that additional adsorption and desorption are negligible during the course of the experiment, the surface excess may be represented by the total excess, Γ_T:

$$\Gamma_T = \Gamma_O + \Gamma_R \tag{12}$$

Equation 11 may be rewritten as:

$$\left(\frac{\Gamma_O}{\Gamma_R} + 1\right)^{-1} = \frac{\Gamma_R}{\Gamma_T} \tag{13}$$

Inserting Equation 11 into Equation 13 results in:

$$\left(e^{\frac{nF}{RT}(E_{Applied}-E^{o'})} + 1\right)^{-1} = \frac{\Gamma_R}{\Gamma_T} \tag{14}$$

In a linear cathodic sweep, the total charge (q) passed will be governed by $nFA\Gamma_O$. At any given potential in the sweep, the total charge passed is determined by:

$$q(E) = nFA\Gamma_T\left(\frac{\Gamma_R}{\Gamma_T}\right) = nFA\Gamma_T\left(e^{\frac{nF}{RT}(E_{Applied}-E^{o'})} + 1\right)^{-1} \tag{15}$$

since the total charge passed at any potential is proportional to the fraction of oxidized adsorbate that has been reduced. In a cathodic scan, $E = E_{initial} + \nu t$ where ν is the scan rate and t is the time elapsed. Taking that current, i, is defined as charge passed per unit time, $i = \partial q/\partial t$, Equation 15 then becomes:

$$i = -\frac{n^2F^2}{RT}\nu A\Gamma_T\left(\frac{\exp\left[\frac{nF}{RT}(E_{Applied} - E^{o'})\right]}{\left(1+\exp\left[\frac{nF}{RT}(E_{Applied} - E^{o'})\right]\right)^2}\right) \tag{16}$$

For a cathodic scan, the scan is taken from positive to negative potential. Therefore, the scan rate is negative and the resulting current is positive. For the reverse scan, the scan

rate is positive and the current is therefore negative. Figure 6 is an example of cyclic voltammograms (CVs) calculated from Equation 16.

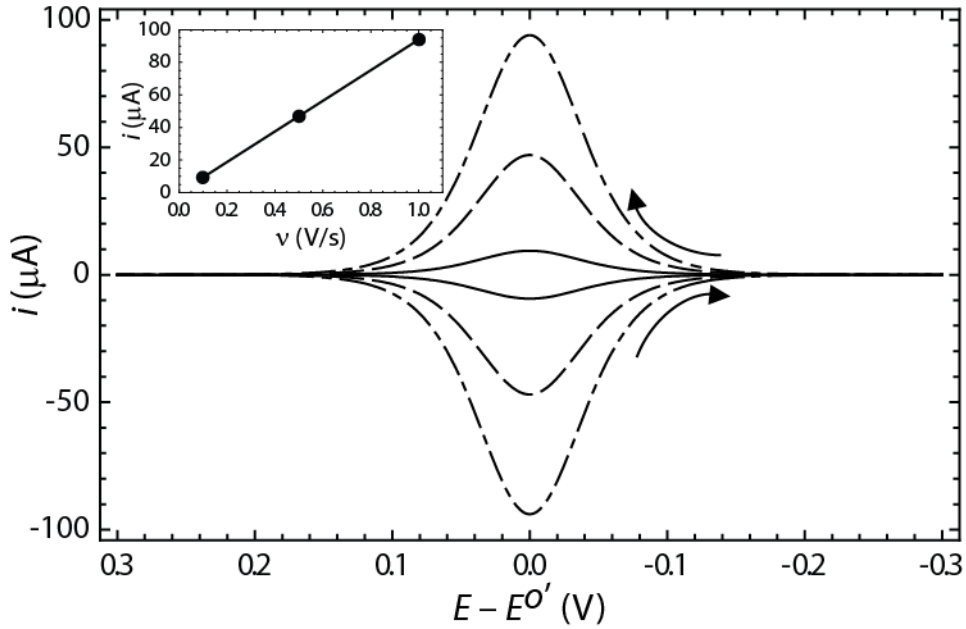

Figure 6: Simulated CVs for 10^{-10} mol/cm^2 adsorbed species R for scan rates of 0.1 (solid), 0.5 (dashed), and 1.0 (dot-dashed) V/s. Arrows indicate direction of scan. The inset shows the linear relationship between the maximum current of the first segment with respect to scan rate. T = 25 °C, A = 1.0 cm^2.

Examination of Figure 6 shows several characteristics for CVs of an adsorbed species that are commonly used to determine that the electroactive species is indeed adsorbed. Upon sweeping the potential, the current rises to a maximum value $E^{o'}$ before falling back to a negligible value. The return scan is then a mirrored image of the forward scan. This symmetric nature of the CV is characteristic of an adsorbed species; however, under circumstances where the kinetics of electron transfer is sluggish, the forward and reverse scans will exhibit maxima that are offset.[37] For this reason, it is customary when performing CV experiments to measure CVs at several scan rates and examine the relationship of the peak current with respect to scan rate. As shown in the inset, Figure 6,

the peak current is directly proportional to the scan rate, as shown in Equation 16. This relationship is a characteristic observation for surface electrochemistry.

1.3.4.2 Cyclic Voltammetry of a Dissolved Species

Now that the basic background behind cyclic voltammetry of an adsorbed species has been established, the case of a dissolved species will now be considered. First, the Nernst equation must be rewritten as a time-dependent form.

$$E_{\text{Applied}} = E^{o'} - \frac{RT}{nF}\ln\left(\frac{C_{\text{R}}(0,t)}{C_{\text{O}}(0,t)}\right) \tag{17}$$

In this notation, $C_{\text{x}}(\text{y},t)$ refers to the concentration of species x a distance y from the surface of the electrode at time t. Inserting Equation 9 into Equation 17 results in

$$E_{\text{Initial}} + \nu t = E^{o'} - \frac{RT}{nF}\ln\left(\frac{C_{\text{R}}(0,t)}{C_{\text{O}}(0,t)}\right) \tag{18}$$

In order to mathematically determine the rate at which a species is carried to the electrode surface by diffusion, Equation 18 must first be solved for $C_{\text{R}}(0,t)/C_{\text{O}}(0,t)$. Once a concentration gradient has been established between the electrode surface and the bulk solution (as described by Equation 18), Fick's second law must then be used to describe the rate at which concentration changes due to diffusion. Solving Fick's law to describe diffusion to a planar electrode involves making a Laplace transform. Unfortunately, because both applied potential and diffusion are dependent upon time, a discrete solution for the Laplace transform is not possible. Therefore, the relationship between current and time for a CV dissolved species cannot be obtained as for the case of adsorbed species. Instead, each point along the CV must be considered numerically to predict the CV of a dissolved species.[1] There are several commercially available software packages for simulating CVs (the author uses DigiElch® in this work). In the remainder of this introduction, the CVs for a dissolved species will be simulated using DigiElch and considered empirically.

The electrode reaction in Equation 1 will again be considered. A simulated CV that would typically be observed for 1 mM O in solution is depicted in Figure 7. As with Figure 6, several scan rates will be simulated and the electron transfer between the electrode and analyte is assumed to be extremely fast.

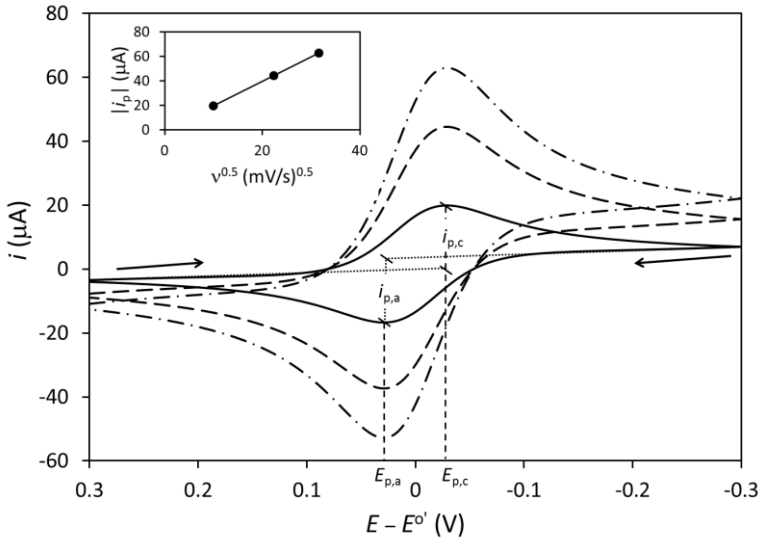

Figure 7: Simulated CVs of 1 mM O at a planar electrode with 0.8 mm radius for scan rates of 100 (solid), 500 (dashed), and 1000 mV/s (dot-dashed). Arrows indicate direction of scan. $D_o = D_R = 10^{-5}$ cm^2/s, $T = 25$ °C.

In these CVs, the scan is started at a potential of 0.3 V with respect to $E^{o'}$, swept to –0.3 V and then swept back to 0.3 V to complete one *cycle.* For clarity, only the second cycle is shown in Figure 7. In each sweep segment, there are three distinct features: first, the current begins to increase as the potential approaches the $E^{o'}$; second, the current peaks at a potential slightly beyond $E^{o'}$; and third, the current decreases as the scan continues farther beyond $E^{o'}$. The same characteristics are observed for the return scan. There are several important characteristics of this CV that must be commented upon. First, the anodic and cathodic peak currents, $i_{p,a}$ and $i_{p,c}$, respectively, are equal in magnitude. In CV experiments, i_p (in amperes) is determined by[1]

$$i_p = 0.4463\left(\frac{F^3}{RT}\right)^{1/2} n^{3/2} A D^{1/2} C^* \nu^{1/2} \tag{19}$$

where A is the area of the electrode in cm, D is the diffusion coefficient of the analyte in cm^2/s, and C^* is the concentration of the analyte in the bulk solution in M. As mentioned previously, it is prudent to measure several CVs at varied scan rates. Consistent with Equation 19, i_p is indeed proportional to the square root of the scan rate (inset, Figure 7) in the simulated voltammograms. Experimentally verifying this relationship confirms that the species being interrogated electrochemically is indeed dissolved in solution rather than adsorbed on the electrode surface. A second important feature to observe when analyzing CVs is the potential separation of the anodic and cathodic peaks, $\Delta E_p = E_{p,a} - E_{p,c}$. This peak separation is related to n by the relationship $\Delta E_p = 0.059/n$ V.

To this point, only systems in which the transfer of electrons from the electrode to the analyte is rapid have been considered. Before expanding this introduction to systems with sluggish electron transfer, several new parameters that define the electrode reaction must be introduced: the *forward rate constant,* k_f, *backward rate constant,* k_b *standard rate constant,* k^o, and the *transfer coefficient*, α. Taking kinetics into account, the electrode reaction in Equation 1 is rewritten as

$$O + n\,e^- \underset{k_b}{\overset{k_f}{\rightleftharpoons}} R \tag{20}$$

As with any equilibrium, there is a forward and reverse reaction taking place under all conditions. These reaction rates at any given time are defined by k_f and k_b, respectively. Under the special circumstance that $C_R(0,t) = C_O(0,t)$, the electrode potential $E_{Applied} = E^{o'}$ and as a result $k_f = k_b$. The parameter k^o is defined as the value of k_f (and subsequently k_b) when the applied potential is equal to the formal reduction potential.

The term α is used to describe the symmetry of the transition state in a reaction coordinate diagram. If the approach to the transition state is considered to be linear, as shown in Figure 8, the value of $(1-\alpha)$ may be defined as the relative position between O

and R at which the transition state occurs. This value, which typically ranges from 0.3 to 0.7, is only observable experimentally for cases in which k^o is rather small. In situations of fast electron transfer, α is often given a value of 0.5 for the sake of simplicity.

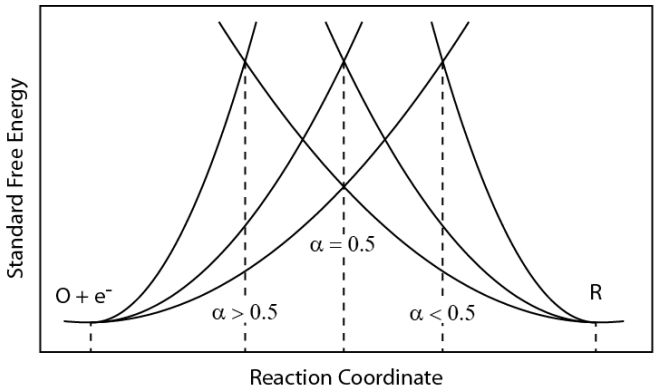

Figure 8: Effect of α on the reaction coordinate diagram for the reaction $O + e^- \rightleftharpoons R$.

Because defining these terms further is beyond the scope of this thesis, their effects will instead be explored using CV simulations. As mentioned earlier, the effect of α is only observed under conditions of sluggish electron transfer. Therefore, the kinetics of electron transfer will first be considered. Simulated CVs for several values of k^o are shown in Figure 9.

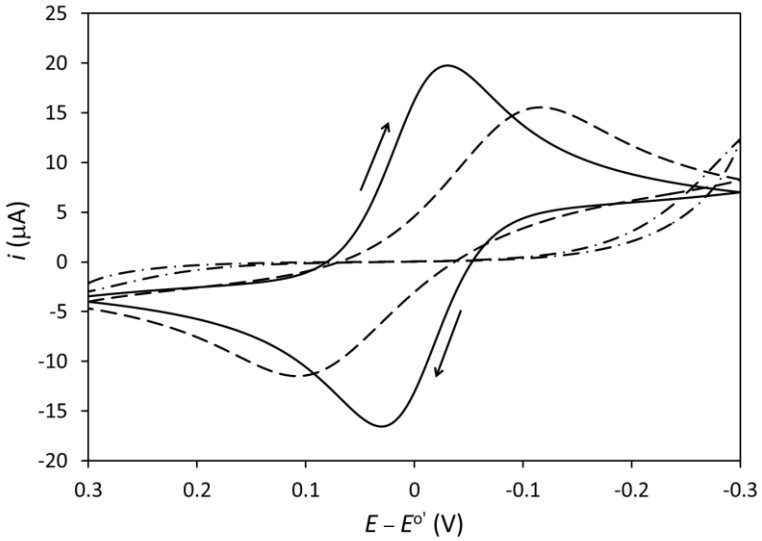

Figure 9: Simulated CVs of 1 mM O for k^o values of 10^1 (solid), 10^{-3} (dashed), and 10^{-5} (dot-dashed) cm/s at a 0.8 mm radius electrode. Arrows indicate direction of scan. α = 0.5, T = 25 °C, ν = 100 mV/s, $D_O = D_R = 10^{-5}$ cm^2/s.

Figure 9 depicts a CV in each of the three kinetic regimes that are generally defined when considering voltammograms: *reversible* (solid CV), *quasireversible* (dashed CV), and *irreversible* (dot-dashed CV). Clearly, because reversibility is defined by the kinetics of electron transfer, the shape of the CVs for a quasireversible or irreversible electron transfer will be dependent upon scan rate. In fact, a system that is reversible at a slow scan rate can (and often does) appear to be irreversible at faster scan rates.

The reversibility of an electrochemical reaction has been defined by Matsuda and Ayabe as the following k^o ranges with respect to scan rate.[38]

Reversible	$k^o \geq 0.3\ \nu^{1/2}$ cm/s
Quasireversible	$0.3\ \nu^{1/2}$ cm/s $\geq k^o \geq 2 \times 10^{-5}\ \nu^{1/2}$ cm/s
Irreversible	$k^o \leq 2 \times 10^{-5}\ \nu^{1/2}$ cm/s

Now that a range of typical values for k^o have been established, the effect of α on cyclic voltammograms is depicted in Figure 10. Because α shows a visible effect on the CV only for rather slow electron transfer, a value of k^o of 10^{-3} is used for these simulations.

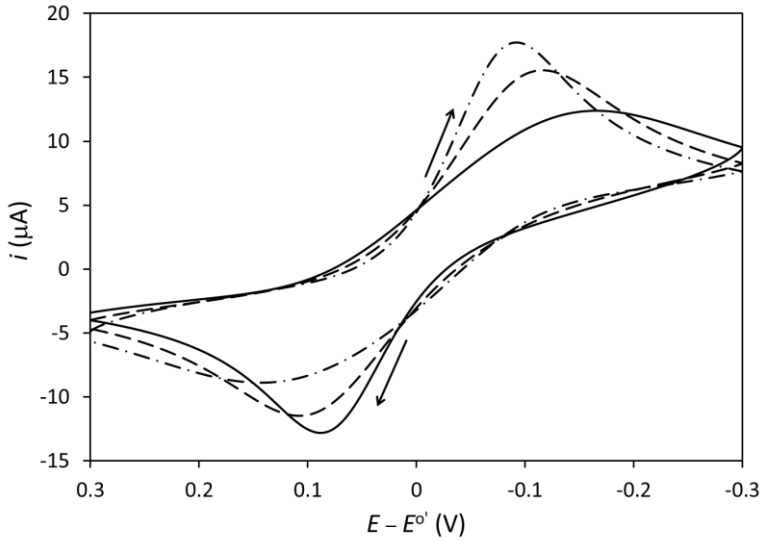

Figure 10: Simulated CVs of 1 mM O for α values of 0.3 (solid), 0.5 (dashed), and 0.7 (dot-dashed) at a 0.8 mm radius electrode. Arrows indicate direction of scan. $k^o = 10^{-3}$ cm/s, $T = 25$ °C, $\nu = 100$ mV/s, $D_O = D_R = 10^{-5}$ cm^2/s.

Clearly, the effect of α is quite pronounced for quasireversible CVs. Under the condition that $\alpha = 0.5$, the forward and reverse scan of the CV are highly symmetric while deviations in α away from 0.5 result in a loss of this symmetric nature. This phenomenon may be justified as follows: when $\alpha > 0.5$, the electroactive molecule O needs to undergo only a rather small change in spatial configuration to reach the transition state while the corresponding R undergoes a large change in spatial configuration, as interpreted by transition state theory. As a result, reaching the transition state from O is faster than from R and the reduction of O statistically more likely than

(and therefore faster than) the oxidation of R. The opposite argument holds true for small values of α. This interpretation is manifested in the CVs shown in Figure 10

1.3.5 Voltammetry with Weakly Supported Media

Every solution used for electrochemical experiments exhibits a bulk resistance. Typically, this resistance is kept as small as possible by the addition of a supporting electrolyte; however, resistances in the range of 100 Ω for aqueous electrolyte solutions up to tens of MΩ for extremely nonpolar organic solvents may be observed.[1,2,39] If this bulk resistance is not compensated for in an electrochemical experiment, distortion of the measured current-potential relationship will be observed. Under such conditions, the actual applied potential deviates from the measured (intended) potential by the relationship

$$E_{\text{Applied}} = E_{\text{Apparent}} - iR_{\text{u}} \tag{21}$$

where E_{Applied} is the actual applied potential, E_{Apparent} is the measured (intended) potential, i is the current passing through the sample solution at the applied potential and R_{u} is the uncompensated solution resistance. To highlight the effect of this distortion, simulated CVs for a redox system of $O + e^- \leftrightarrows R$, where O is an oxidized species and R is a reduced species, with several different values for the uncompensated solution resistance are presented in Figure 11.

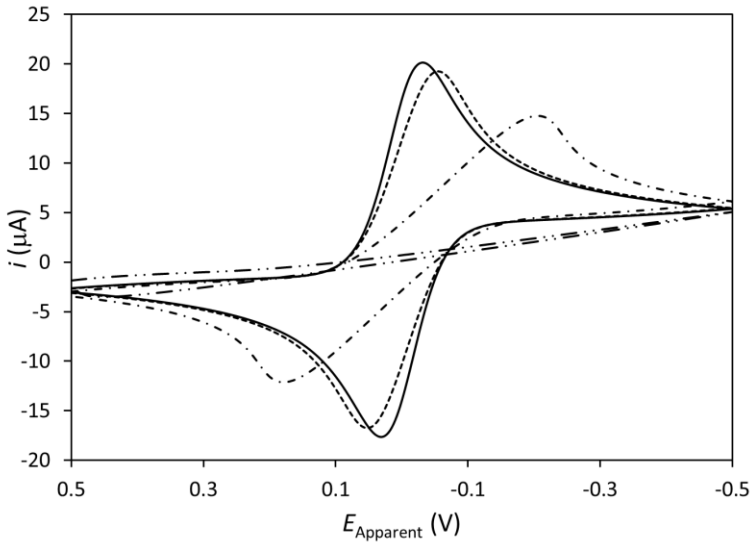

Figure 11: Simulated voltammograms of 1 mM O at a planar electrode of 8 mm radius and R_u of 10^2, 10^3, 10^4, and 10^5 Ω. $E^{o'}$ = 0.0 V, Scan rate = 100 mV/s, T = 25 °C, D_O = D_R = 10^{-5} cm^2/s, α = 0.5, k^o = 10^5 cm/s.

Performing voltammetry in solutions of extremely high resistance may still be performed with a few experimental considerations. First, the overall effect of bulk solution resistance may be minimized by careful construction of the three-electrode cell used for the experiment.[40] Specifically, by positioning the reference electrode as close to the electrode surface as possible (without blocking mass transport to the electrode) the resistance drop between the working electrode and reference electrode is limited. Second, the total current passed (and thus the contribution of the iR_u) may be minimized by utilization of electrodes with diameter in the μm range, often referred to as *ultramicroelectrodes* (UMEs).[41]

The addition of a supporting electrolyte is also required to maintain control over mass transport of the analyte to the electrode. More specifically, ionic species in unstirred solutions may be carried to the electrode by either diffusion or migration mechanisms. In

transient electrochemistry experiments, such as voltammetry, the primary mode of analyte transport to the electrode surface must be diffusion.[42-44]

The following section is used to calculate the fraction of current carried by migration and, consequently, the amount of deviation from ideal that will be observed in weakly supported systems. For a system with a cross-section of area A, the current, *i*, carried by an ion is determined by

$$i = \frac{z^2 F^2 ADC}{RT} \times \frac{\partial \phi}{\partial x} \tag{22}$$

where and $\partial\phi/\partial x$ is the potential gradient across the cell. The mobility of an ion, *u*, in an electric field is given by the Einstein-Smoluchowski equation,

$$u = \frac{|z|FD}{RT} \tag{23}$$

Inserting Equation 3 into Equation 2 gives the current carried by an individual ionic species, *j*, is thus

$$i_{\mathrm{j}} = |z_{\mathrm{j}}| FAu_{\mathrm{j}} C_{\mathrm{j}} \times \frac{\partial \phi}{\partial x} \tag{24}$$

Therefore, if many ionic species are present in solution, the fraction of the total current carried by ion j is thus

$$\frac{i_{\mathrm{j}}}{i_{\mathrm{total}}} = \frac{|z_{\mathrm{j}}| u_{\mathrm{j}} C_{\mathrm{j}}}{\sum_{\mathrm{k}} |z_{\mathrm{k}}| u_{\mathrm{k}} C_{\mathrm{k}}} \tag{25}$$

If 1 mM solution of a singly charged analyte is prepared with the addition of 100 mM electrolyte and the mobilities of all ions in solution are assumed to be equal, the percentage of the total current carried by the analyte determined by Equation 25 is 0.5%. However, if the analyte concentration is increased to 5 mM, already 2.4% of the total current is carried by the analyte ion. Because migration is a considerably faster process than diffusion,[1] this will result in a substantially higher current than anticipated. Therefore, it is imperative that the concentration of electrolyte in solutions used transient electrochemistry experiments be maintained at a large excess to the analyte. The careful

selection of a suitable electrolyte becomes especially challenging when working with solvents that solvate ions extremely poorly(*e.g.* hydrocarbons and fluorocarbons).

Previous development of lipophilic electrolyte salts has allowed for electrochemistry in a wide variety of low polarity solvents.[45-48] Electrolytes such as the tetrabutylammonium salts of perchlorate, tetrafluoroborate, and hexafluorophosphate are rather soluble in nonpolar solvents and thus have been used to perform voltammetry with solvents such as cyclohexane,[45] heptane,[47] and supercritical CO_2.[46] Unfortunately, these salts are only sparingly soluble in fluorous liquids, which are the least polar and polarizable solvents known.[49] Moreover, salts that had previously been shown to dissolve in fluorous solvents have been shown to be heavily ion-paired and are thus not suitable as supporting electrolytes.[50]

The first published example of electrochemistry in a fluorous solvent-containing matrix was demonstrated by LeSuer and Geiger in 2006.[51,52] By pairing tetrakis[3,5-bis(trifluoromethyl)phenyl]borate with an imidazolium cation containing a fluorinated ponytail (Figure 12), they performed voltammetry with benzotrifluoride and perfluoro-(methylcyclohexane) in a 1:1 volumetric ratio. This mixed solvent system showed an order of magnitude increase in bulk resistivity when compared to the same electrolyte in pure benzotrifluoride. The increase in resistivity is attributed to the decrease in the dielectric constant of the solution upon addition of the fluorous solvent. Thus, the resistivity of this system is expected to continue increasing upon further addition of perfluoro(methylcyclohexane).

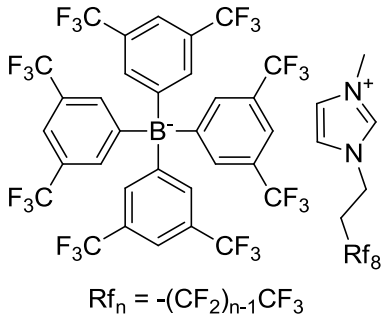

Figure 12: Fluorophilic electrolyte used for the first example of electrochemistry in a fluorous-containing medium.

1.4 Overview

The main goal of this work is to develop a sensing device that is capable of selectively binding and detecting DNT. Because fluorous sensing matrixes have been previously shown to greatly enhance the stability of host–guest complexes,[53-55] the ultimate goal of this work is to incorporate DNT-selective receptors into a fluorous matrix for enhanced sensitivity and selective for DNT. Therefore, in Chapter 2, an electrolyte for performing electrochemistry with fluorous matrixes is introduced. As a proof-of-concept, cyclic voltammetry of ferrocene was performed. Quantitative fitting of the resulting CVs shows that the transfer coefficient for ferrocene in the fluorous phase is well within the range previously reported in the literature. Conversely, the k^o determined by this fitting is orders of magnitude lower than in solvents typically used for electrochemistry. Using well-established Marcus theory, this discrepancy is explained. Because the electrolyte used for voltammetry is not commercially available at this time, the use of large sample volumes is undesirable. Thus, a sample cell that allows for performing cyclic voltammetry with sample volumes of 200 μL is presented in Chapter 3. This sample cell also has the potential of greatly reducing the size of samples typically used for electrochemistry experiments in undergraduate teaching laboratory experiments; thus, this chapter is presented in terms of reducing sample sizes for such experiments.

Chapter 4 begins to explore the development of receptors for the detection of DNT by attempting to determine the formation constants for the interaction of DNT with aliphatic amines in so-called "Meisenheimer complexes." However, we definitively show that DNT does *not* form an appreciable concentration of Meisenheimer complexes in the presence of amines in dimethylsulfoxide; rather, DNT is deprotonated. While developing the theory for interpretation of the Job's plot data collected for the interaction of DNT with these amines, a new method for quantitatively interpreting these plots was developed and is presented in Chapter 5. This method allows for quantitatively interpreting the type of interaction observed with a Job's plot by comparing the area under the curve to the reactant stoichiometry. In Chapter 6, the electrochemistry of DNT is further explored using cyclic voltammetry. We observe that DNT is reduced in two well-resolved electron transfers in aprotic media. Quantitative interpretation of these CVs is immensely complicated, as the radical anion formed by reduction of DNT is sufficiently basic to deprotonate neutral, uncharged DNT. Upon addition of an acidic species, the two reduction waves coalesce into a one-step, six-electron irreversible transfer. This is explained as the reduction of the two nitro groups to *N*-hydroxylamino groups.

Chapter 7 brings together the knowledge gained in Chapters 4 and 6 to construct a sensing device for DNT. In collaboration with Melissa Fierke from the Stein research group, a sensing electrode was constructed from 3-dimensionally ordered macroporous (3DOM) carbon. The surface of the 3DOM carbon monolith was modified by covalent attachment of a receptor molecule for DNT. Using cyclic and square wave voltammetry, the response of the electrode was characterized for DNT. These electrodes also showed selectivity over interferents commonly tested for DNT sensors. Chapter 8 explores increasing the electrochemical window for solvent/electrolyte systems. This research has a large bearing on increasing the bias voltage window accessible for electrochemical capacitor devices. While this chapter is a slight departure from the sensing theme of previous chapters, it does provide an increase in knowledge for the fundamental

electrochemistry upon which electrochemical capacitors operate. Lastly, Chapter 9 summarizes the results that have been presented in this thesis and discusses the directions for possible continuation of this work.

2 CHAPTER TWO

Electrochemistry in Media of Exceptionally Low Polarity: Voltammetry with a Fluorous Solvent

In part from:

Olson, E. J.; Boswell, P. G.; Givot, B. L.; Yao, L. J.; Bühlmann, P. "Electrochemistry in Media of Exceptionally Low Polarity: Voltammetry with a Fluorous Solvent" *Journal of Electroanalytical Chemistry*, **2010**, 639, 154-160.

This work was a joint effort by this author and P. G. Boswell, who carried out the synthesis and characterization of the fluorophilic electrolyte along with the determination of the resistivity of the fluorous electrolyte solution.

This work demonstrates the first cyclic voltammetry in a perfluorocarbon solvent without use of a cosolvent. The novel electrolyte tetrabutylammonium tetrakis[3,5-bis(perfluoro-hexyl)phenyl]borate (NBu_4BArF_{104}; 80 mM) allows for voltammetry of ferrocene in perfluoro(methylcyclohexane) by lowering the specific resistance to 268 kΩ cm at 20.8 °C. Despite significant solution resistance, the resulting voltammograms can be fitted quantitatively without difficulty. The thus determined standard electron transfer rate constant, k^o, for the oxidation of ferrocene in perfluoro(methylcyclohexane) is somewhat smaller than for many solvents commonly used in electrochemistry, but can be explained readily as the result of the viscosity and size of the solvent using Marcus theory. Dielectric dispersion spectroscopy verifies that addition of NBu_4BArF_{104} does not significantly raise the overall polarity of the solution over that of neat perfluoro(methylcyclohexane).

2.1 Introduction

Organic solvents have found extensive application as solvents for electrochemistry.[33] Their wide-ranging solvent environments provide electroactive species with distinctive solubility, stability, and reactivity characteristics.[33,56] In particular, through the development of electrochemically stable lipophilic electrolytes,[48] electrochemistry was demonstrated with low polarity solvents such as cyclohexane,[45] heptane,[47] and super-critical CO_2.[46] While many of these solvents have no permanent dipole moment, they still exhibit a significant degree of polarizability. Fluorous solvents, on the other hand, have a very low polarizability, resulting in very weak van der Waals forces between their molecules and making them the most nonpolar solvents known.[49] For example, on the π^* scale of solvent polarity/polarizability,[57] where dimethylsulfoxide is defined as 1 and cyclohexane 0, perfluorooctane can be found at –0.41. In fact, octane and perfluorooctane do not mix at room temperature precisely because octane is too polarizable.[58]

This extremely low polarity makes fluorous phases very useful for probing the electrochemical behavior of species at near gas-phase conditions.[59,60] Advantages also arise from the exceptional level of chemical inertness of perfluorocarbons and—in view of spectroelectrochemistry[61-63]—their optical transparency down to 160 nm and the low absorbance in a wide range of the IR spectrum [61,62]. Since fluorous phases have become important tools in catalytic synthesis[49,64] and separation techniques,[55] electrochemistry in these media could allow online monitoring of reaction progress and separation efficiency. Other possible applications lie in battery technology and the study of fluorous monolayers on macroscopic surfaces[49,55] and nanoparticles.[49,65]

Despite the many possible uses of electrochemistry with fluorous solvents, voltammetry in a perfluorocarbon solvent has not been reported yet. Even the most lipophilic salts known are only sparingly soluble in a fluorous solvent, and any salt that does dissolve is heavily ion-paired.[51,53] Geiger and LeSuer demonstrated voltammetry with perfluoro(methylcyclohexane) (**1**) and an electrolyte consisting of the tetrakis(3,5-trifluoromethyl)phenyl borate anion and an imidazolium cation with a fluorous ponytail,

but they had to use the comparatively polar benzotrifluoride with a dielectric constant of 9.2 as cosolvent in a 1:1 ratio to perfluoro(methylcyclohexane).[52]

We demonstrated previously the first potentiometric sensors based on fluorous membranes using perfluoro(perhydrophenanthrene) as the membrane matrix and the sodium salt of tetrakis[3,5-bis(perfluorohexyl)phenyl]borate to provide for ionic sites.[50,51] The receptor-free and receptor-doped sensors displayed excellent selectivities and show promise to reduce biofouling.[53] However, the low solubility of this salt (1 mM) and strong ion pairing resulted in bulk resistances too large for any electrochemical technique requiring significant current. Using the novel fluorophilic electrolyte prepared from this tetrakis[3,5-bis(perfluorohexyl)phenyl]borate and the tetrabutylammonium cation (NBu_4BArF_{104}) (**2**), we report in this work the first demonstration of voltammetry in an undiluted perfluorocarbon solvent, specifically perfluoro(methylcyclohexane). This compound is an excellent representative of fluorous solvents as its π^* value (–0.48) and dielectric constant (1.86) are very low even among fluorous phases.[66] With its boiling point of 76 ºC at 1.00 atm (partial pressure 0.139 atm at 25 °C),[67] perfluoro(methylcyclohexane) is much more convenient to work with than the more volatile perfluorohexane or perfluorocyclohexane. Moreover, unlike the commercially available perfluoro(dimethylcyclohexane) and perfluoro(perhydrophenanthrene), perfluoro(methylcyclohexane) is not a mixture of isomers.

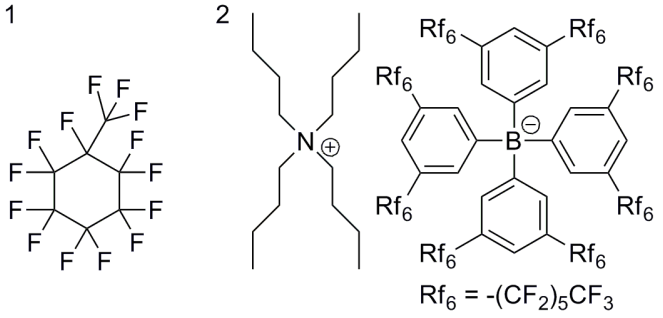

Figure 13: Structures of perfluoro(methylcyclohexane) (**1**) and NBu_4BArF_{104} (**2**).

2.2 Experimental

2.2.1 Chemicals

All reagents were of the highest commercially available purity. Perfluoro(methylcyclohexane) and tetrabutylammonium chloride were used as received from Alfa Aesar (Ward Hill, MA, USA) and Fluka (Milwaukee, WI, USA), respectively. Sodium tetrakis[3,5-bis(perfluorohexyl)phenyl] borate tetrahydrate was prepared according to a previously described procedure.[50]

NBu_4BArF_{104} was synthesized by metathesis from tetrabutylammonium chloride and sodium tetrakis[3,5-bis(perfluorohexyl)phenyl]borate. 10.0 g of sodium tetrakis[3,5-bis(perfluorohexyl)phenyl]borate tetrahydrate and 1.03 g of tetrabutylammonium chloride were added to a separatory funnel containing 300 mL water and 300 mL FC-72 (perfluorohexanes). The mixture was shaken until all of the salt dissolved. The FC-72 layer was collected, washed three times with 300 mL water, dried with $MgSO_4$ and filtered. The solvent was removed by rotary evaporation and further drying under vacuum at 75 °C for 48 hours, yielding NBu_4BArF_{104} as a colorless, wax-like material in quantitative yield. ^{1}H NMR (500 MHz, FC-72, δ): 0.507 (t, J_{HH} = 7.2 Hz, –CH_3, 12H), 0.75–0.90 (m, –CH_2CH$_3$, 8H), 1.04–1.19 (m, NCH$_2$CH_2–, 8H), 2.42–2.58 (m, NCH_2–, 8H), 7.31 (s, *p*-Ar*H*, 4H), 7.51 (s, *o*-Ar*H*, 8H). The corresponding tetraethyl- and tetrahexylammonium salts were prepared analogously. Differential scanning calorimetry (DSC, see Supplementary Material for details) revealed a glass-transition temperature of –21 °C, showing that **2** is a highly viscous ionic liquid at room temperature.

2.2.2 Resistance Measurements

The specific resistance of the 80 mM NBu_4BArF_{104}/perfluoro(methylcyclohexane) solution was measured by impedance spectroscopy using a homemade cell. A Solartron SI 1287 electrochemical interface was used in combination with a Solartron 1255B frequency response analyzer (Solartron Analytical, Farnborough, Hampshire, England) at an AC amplitude of 100 mV, swept over a frequency range from 100,000 Hz to 10 Hz,

using a DC offset equal to that of the open circuit potential. Solution resistance was determined by a fit of the resulting complex impedance plot to a model circuit consisting of a resistor in series with a parallel resistor/capacitor. The cell was made of two polished stainless steel disks separated by a Teflon ring (0.2 cm thick, 0.7 cm inner diameter). In each measurement, the fluorous solution was injected into the cell, the cell was placed in a Teflon pocket, and the pocket was suspended in a water bath thermostated at 20.8 °C. All samples were placed in the bath for at least 20 minutes prior to measurement. The cell constant was determined by a KCl conductivity standard purchased from Sigma-Aldrich (St. Louis, MO, USA).

2.2.3 Voltammetry

Voltammetry was performed with a CHI600C Potentiostat in combination with a CHI200B Picoamp Booster and Faraday Cage (CH Instruments, Austin, TX, USA). A 10 μm diameter Pt microelectrode from Bioanalytical Systems (BAS; West Lafayette, IN, USA) was used as the working electrode, a Au disk electrode (BAS) as the auxiliary electrode, and a silver wire (>99%, Alfa Aesar) as a quasi-reference electrode. Cyclic voltammograms (CVs) of ferrocene were performed at concentrations of 5.43, 2.72, 1.36, and 0.68 mM. Each concentration was scanned at 10, 50, 100, and 1000 mV/s. The resultant CV curves were then fitted using the DigiElch software package (ElchSoft, Kleinromstedt, Germany). All voltammograms are resistance corrected using the method outlined in the Supplementary Material before fitting.

Polishing equipment was purchased from Buehler (Lake Bluff, IL, USA). Prior to each experiment, the working electrode was polished on Microcloth polishing pads, first with 5.0 μm Micropolish II deagglomerated alumina, then with 1.0 μm and 0.25 μm MetaDi Supreme polycrystalline diamond suspension, and lastly with 0.05 μm Micropolish II deagglomerated alumina. The polished electrode was then ultrasonicated in a Triton X-100 detergent solution for 3 minutes, rinsed, and dried. Water used for the detergent solution and for rinsing the electrode was deionized and charcoal-treated (≥18.2

MΩ cm specific resistance) with a Milli-Q PLUS reagent-grade water system (Millipore, Bedford, MA, USA). Typically, samples were not purged of oxygen in order to minimize loss of solvent (purging did not have a significant effect on the shape of the CV in the potential range necessary to observe ferrocene), except in the case of the measurement of the electrochemical window (Figures 2 and 3), in which case the samples were purged with solvent-saturated argon for 30 min prior to measurement.

2.2.4 DOSY ^{19}F NMR

DOSY ^{19}F NMR was performed on a Varian INOVA 300 spectrometer equipped with a 4-nucleus probe capable of pulsed field gradients operating at 282.12 MHz. A bipolar pulse pair stimulated echo (BPP-STE) sequence, as described in ref. 68, was used to determine the diffusion coefficients of tetrakis[3,5-bis(perfluorohexyl)phenyl]borate and the solvent in a solution of 80 mM NBu_4BArF_{104} in perfluoro(methylcyclohexane). The field gradient was calibrated using the self-diffusion coefficient of 6.1×10^{-6} cm^2 s^{-1} for perfluoro(methylcyclohexane) at 20 °C. This value is calculated using equation 1 and the self-diffusion coefficient reported at 25 °C reported in ref.69.

2.2.5 Dielectric Dispersion Spectroscopy

Dielectric dispersion spectroscopy was performed with an HP8720 network analyzer and an open-ended coaxial HP85070B probe (both Hewlett-Packard).[70,71] In addition, a TE01-mode cylindrical dielectric resonator similar to the ones described in ref. [72] was used to measure the complex permittivity at 2.45 GHz. The value of 1.95 measured with the latter probe for the reference heptane agrees well with the literature value of 1.97.[73] For perfluoro(methylcyclohexane), the fluorous electrolyte solution, and heptane as reference, a consistent discrepancy of 0.30 was noted for the measurements with the two probes. Reasons for the discrepancy may be power reflection from the extremities of the specimen back to the probe face, or an air gap between the open-ended coaxial probe and

the liquid sample,[74,75] caused by surface roughness and the poor wettability of the Ni-coated probe with liquids of low polarity. The resulting shift in the dielectric constant (capacitive in nature in case of the latter explanation) was estimated from the TE01-mode cylindrical dielectric resonator measurements of heptane, and applied as a frequency independent correction for all measurements performed with the open-ended coaxial-line probe.

2.3 Results and Discussion

2.3.1 Electrolyte Characteristics

NBu_4BArF_{104} was found to have a high solubility (greater than 80 mM) in perfluoro(methylcyclohexane), perfluorohexanes, perfluoroheptanes, perfluorodecalin, and perfluoro(perhydrophenanthrene), and a solubility of 8 mM in *n*-perfluorohexane. An 80 mM solution of NBu_4BArF_{104} in perfluoro(methylcyclohexane) was measured to have a specific resistance of 268 kΩ cm at 20.8 °C. To explore how the alkyl substituents on the tetraalkylammonium cation affect the properties of $BArF_{104}^-$ salts, tetraethylammonium (NEt_4^+) and tetrahexylammonium (NHx_4^+) salts of $BArF_{104}^-$ were also prepared. NEt_4BArF_{104} was found to have a high solubility in **1**, but an 80 mM solution of NEt_4BArF_{104} in **1** exhibited a solution resistance approximately five times greater than solutions with **2** as the supporting electrolyte. This is indicative of stronger ion pairing for NEt_4BArF_{104} than for the tetrabutylammonium salt **2**. On the other hand, NHx_4BArF_{104} was shown to have a high solubility in **1** (greater than 80 mM) but a somewhat lower solubility than **2** in *n*-perfluorohexane and perfluorodecalin. It follows that among the three tested electrolytes, NBu_4BArF_{104} is the most advantageous one since its cation is large enough to weaken ion pairing but not too large to compromise the solubility in fluorous solvents.

2.3.2 Electrochemical Window

The electrochemical window provided by an electrolyte solution of 80 mM NBu_4BArF_{104} in perfluoro(methylcyclohexane) spans 4.2 V, from +1.9 to –2.3 V vs. the ferrocenium/ferrocene couple (Fc^+/Fc, Figure 14). While the reduction limit is similar to that reported by Geiger and LeSuer for the 1:1 perfluoro(methylcyclohexane)/benzotrifluoride mixed solvent system,[52] the oxidation limit of the perfluoro(methylcyclohexane) solution is 0.6 V greater than that of the solvent mixture.

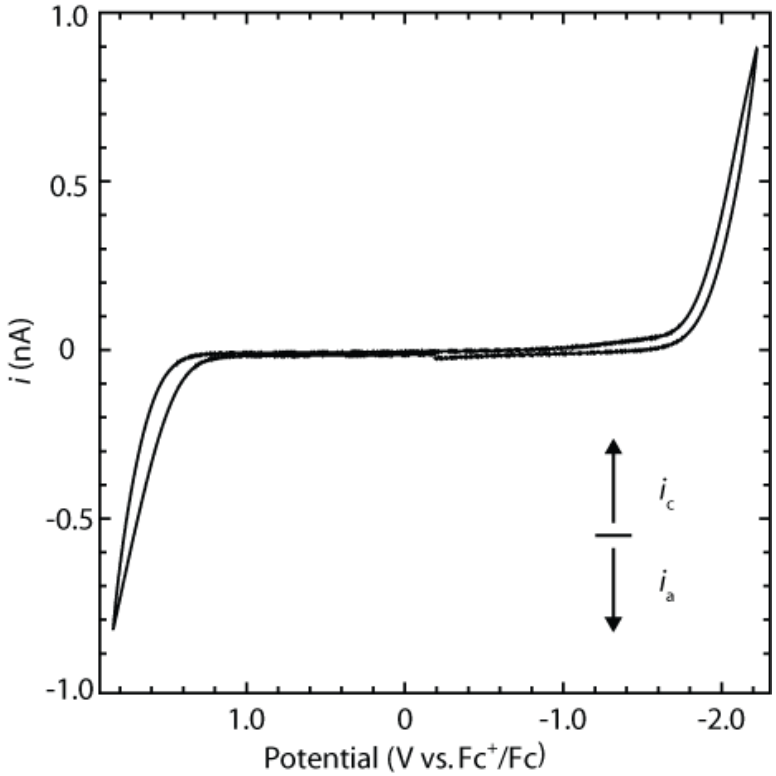

Figure 14: Cyclic voltammogram (CV) of perfluoro(methylcyclohexane) containing 80 mM NBu_4BArF_{104}, scan rate = 100 mV/s, showing the electrochemical background. Data is corrected for solution resistance.

To determine the cause of the reduction limit (i.e., to determine whether it is caused by the solvent or by the electrolyte salt), the reduction potentials of perfluoro(methylcyclohexane) and the electrolyte were determined individually in a Na-distilled THF solution containing 0.1 M NBu_4ClO_4. Each solution was purged for 30 min with Ar before measurements were taken. Addition of 20 mM NBu_4BArF_{104} showed no significant change in the cyclic voltammogram. However, addition of perfluoro(methylcyclohexane) yielded an ill-defined reduction peak at –2.9 V vs. Fc^+/Fc (Figure 15), which is identical to a previously reported value for reduction of this compound in THF solution.[76] This shows that the reduction limit for our fluorous electrolyte solutions is given by the fluorous solvent. Since it has been shown that branched perfluorocarbons are more readily reduced than unbranched ones,[76,77] it appears likely that use of a monocyclic or straight-chain perfluorocarbon as fluorous solvent would further extend the electrochemical window.

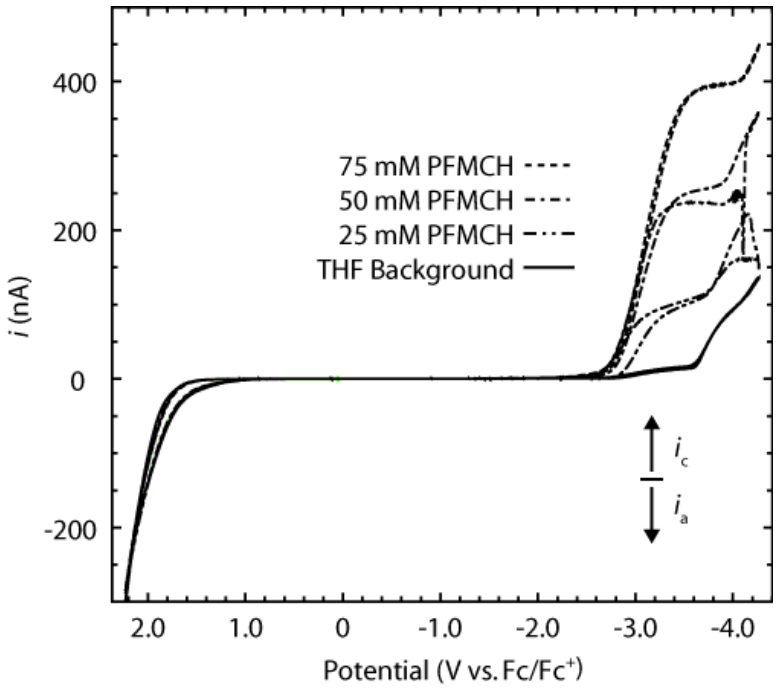

Figure 15: CVs of a 0.1 M NBu_4ClO_4/THF solution containing 0, 25, 50, or 75 mM perfluoro(methylcyclohexane): scan rate = 10 mV/s, T = 21 °C.

To explore the source of the oxidation limit, a solution of 0.1 M NBu_4PF_6 in anhydrous acetonitrile was used as the electrochemical solvent medium, which exhibited an electrochemical window from +2.9 V to –2.6 V vs. Fc^+/Fc. Samples were again purged with argon prior to voltammetric measurements. Upon addition of 25 mM NBu_4BArF_{104} or 25 mM perfluoro(methylcyclohexane), no new oxidation peak could be observed, showing that the oxidation of both NBu_4BArF_{104} and perfluoro(methylcyclohexane) in acetonitrile must occur at positive potentials that are outside the electrochemical window of acetonitrile. This indicates that the oxidation limit in the electrochemical window of the 80 mM NBu_4BArF_{104}/ perfluoro(methylcyclohexane) solution is not caused by the electrolyte or the solvent. Interestingly, upon taking a voltammogram of the NBu_4BArF_{104}/perfluoro(methyl-cyclohexane) solution from -2.30 to +7.45 V vs Fc^+/Fc, a peak of relatively low intensity was observed with a half-wave potential of +1.9 V vs Fc^+/Fc (see Supplementary Material), suggesting that the oxidative limit of the electrochemical window is caused by a species of comparatively low concentration. Since this peak was observed even when perfluoro(methylcyclohexane) was purified by slow filtering through silica gel and storage over KOH, the impurities of perfluoro(methylcyclohexane) that are responsible for the oxidation limit of the electrochemical window do not appear to be polar in character. Moreover, since ^1H NMR spectra of commercial perfluoro(methylcyclohexane) show the presence of hydrogen-containing impurities in the mM range (in comparison, the solvent has a self concentration of 4.96 M), it may be that a low concentration of imperfectly perfluorinated solvent molecules with one (or more) hydrogens is responsible for the oxidative limit.

2.3.3 Voltammetric Measurements

Figure 16 shows CVs of 5.43 mM ferrocene in 80 mM NBu_4BArF_{104} at various scan rates.

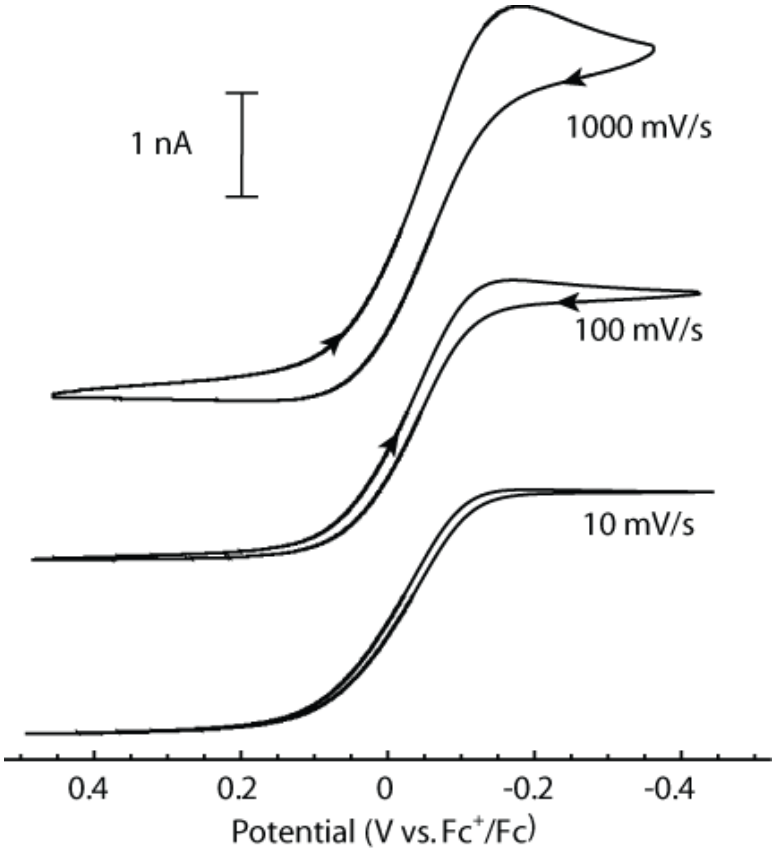

Figure 16: CVs of 5.43 mM ferrocene and 80 mM NBu_4BArF_{104} in perfluoro(methylcyclohexane) with various scan rates. Data is corrected for solution resistance.

The CV measured with a scan rate of 10 mV/s exhibits, in both the forward and backward scan, the typical shape expected for hemispherical diffusion at a microelectrode, i.e., the current reaches a plateau. At scan rates of 100 and 1000 mV/s, the forward scan still has the characteristics of hemispherical diffusion, while the reverse scan exhibits a peak maximum indicative of planar diffusion to the electrode. This suggests that the diffusion coefficient of Fc, which is oxidized in the forward scan, is significantly larger than the diffusion coefficient of Fc^+, which is reduced in the backward scan. Indeed, upon fitting of the voltammograms, the diffusion coefficient for

Fc was determined to be (2.05±0.01) × 10^{-6} cm^2 s^{-1} while that of Fc^+ was determined to be (2.85±0.01) × 10^{-7} cm^2 s^{-1}. This disparity in diffusion coefficients is not surprising since in a fluorous solvent the cation Fc^+ is expected to form very stable ion pairs (and possibly even higher aggregates) with the electrolyte ions. Stability constants for ion pair formation in these solvents (log K_{ip} values from 14 to 16)[50,51,53] are among the strongest ones reported for any condensed phase, which is explained by the extremely low polarity/polarizability of fluorous media.

The accuracy of the diffusion coefficient of Fc^+ determined by fitting of the CVs is supported by the observation that it is within 5.0% of the diffusion coefficient of the fluorophilic borate in 80 mM NBu_4BArF_{104} [(3.0 ± 1.5) × 10^{-7} cm^2 s^{-1}], as determined by ^{19}F Diffusion-Ordered NMR SpectroscopY (DOSY). This result is anticipated when considering that the ion pairs of the fluorophilic borate with tetrabutylammonium likely have very similar geometrical dimensions as the ion pairs of the fluorophilic borate with Fc^+. The DOSY ^{19}F NMR data along with the Stokes-Einstein equation

$$D = \frac{k_B T}{6 \pi r \eta} \qquad (1)$$

also permit a comparison of the effective radii of the $BArF_{104}^-$ anion, r_{anion}, and perfluoro(methylcyclohexane), $r_{solvent}$. Using equation 5, it follows that $r_{anion}/r_{solvent} = D_{anion}/D_{solvent}$ for a solution of the anion. Since the solution viscosity, η, is the same for both species, it does not affect $r_{anion}/r_{solvent}$. With the experimental values of D_{anion} and $D_{solvent}$ (3.0 × 10^{-7} and 4.2 × 10^{-6} cm^2 s^{-1}, respectively), $r_{anion}/r_{solvent}$ is calculated to be 14. This value is larger than what would be expected for an ion pair of $BArF_{104}^-$ and NBu_4^+, confirming that not only ion pairs but also larger ionic aggregates are formed.

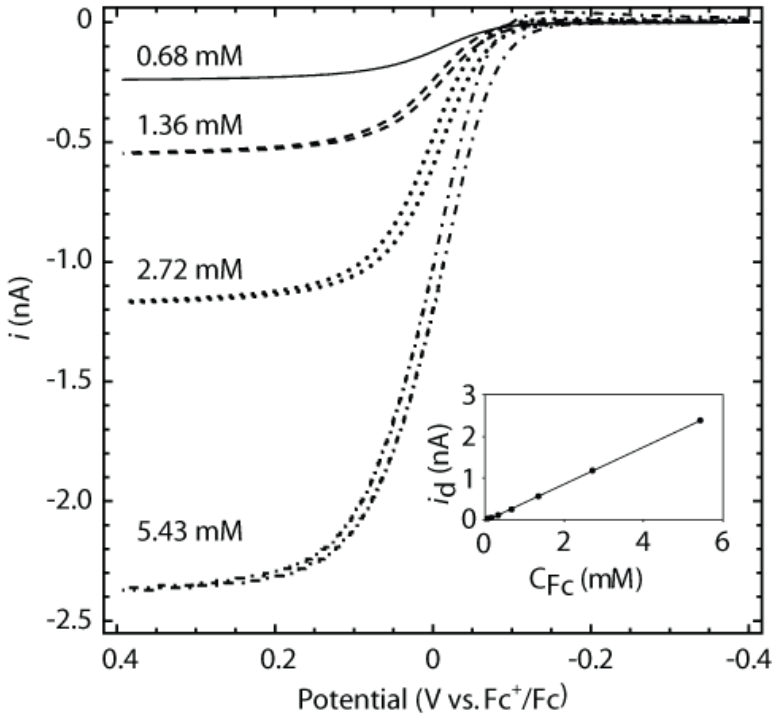

Figure 17: CVs of varied concentrations of ferrocene in 80 mM NBu_4BArF_{104}/ perfluoro(methylcyclohexane): scan rate = 10 mV/s, T = 21 °C. The inset shows the linear relationship between the limiting current and the ferrocene concentration.

Figure 17 shows CVs of ferrocene in the concentration range from 0.68 to 5.43 mM. As anticipated, the CVs overlap very well upon normalization (see Supplementary Material), and the limiting oxidation current is directly proportional to the ferrocene concentration (see inset, Figure 17). The CVs are indicative of a quasi-reversible electron transfer, as suggested by the asymmetry of the oxidation wave and supported by the fits that give a heterogeneous rate constant (k^o) of (7.13±0.04) × 10^{-4} cm s^{-1}. The transfer coefficient determined through fitting was found to be 0.611±0.002. This value falls well within the range of 0.45 to 0.74 that has been published for Fc^+/Fc in a variety of solvents from dichloromethane to methanol.[78-80] As shown in Figure 18, the predicted voltammetric curves overlap well with the experimental ones.

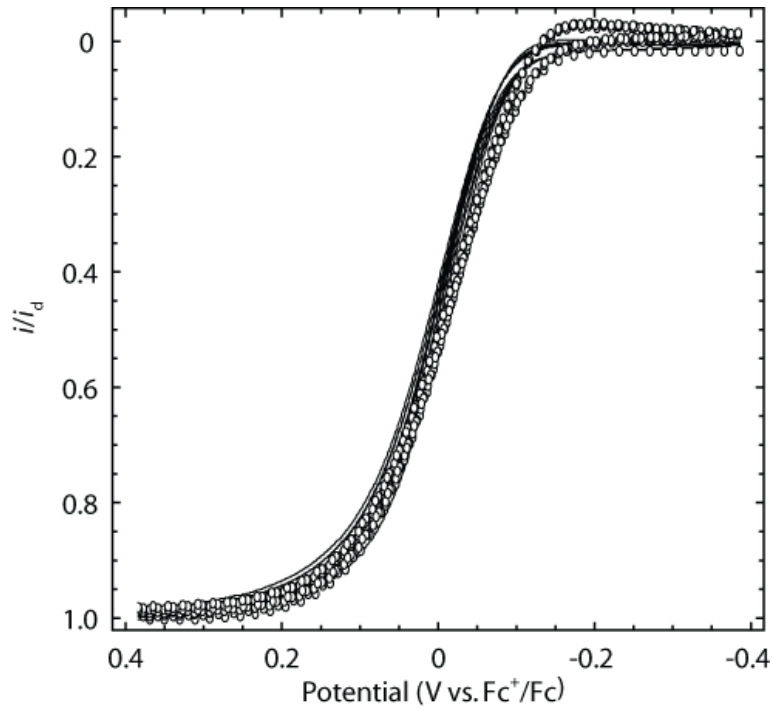

Figure 18: CV of 1.36 mM ferrocene normalized to the diffusion-limited current (solid) along with a fit based on $\alpha = 0.61$, $k^o = 7.13 \times 10^{-4}$ cm/s, D(Fc) = 2.05×10^{-6} cm^2 s^{-1} and D(Fc$^+$) = 2.85×10^{-7} cm^2 s^{-1}(dots).

2.3.4 Heterogeneous Rate Constant

The k^o of $(7.13 \pm 0.04) \times 10^{-4}$ cm s^{-1} as determined by the above described fitting is somewhat smaller than the 0.03 to 8.4 cm/s for ferrocene oxidation at a Pt electrode in solvents ranging from chloroform to acetonitrile, as previously reported.[78-80] Two possible reasons for this observation appeared to be specific adsorption of the electrolyte onto the electrode surface,[81,82] thereby inhibiting the electron transfer, or a slow rearrangement of the solvent and electrolyte, as described by the Marcus theory of electron transfer.[83-86]

To test for the formation of an adsorbed electrolyte layer, a voltammogram of 80 mM NBu_4BArF_{104}/perfluoro(methylcyclohexane) was measured at 10 V/s in the range of -1.1 to 0.9 V vs. Fc$^+$/Fc (see Supplementary Material). The results do not confirm the

formation of an adsorbed layer since peaks indicative of adsorption or desorption events were not observed. However, the formation of such a layer cannot be excluded entirely since a particularly strongly adsorbed layer might not be desorbed in the potential range accessible.

An interpretation of k^o based on the Marcus theory is more straightforward. The effect of solvent dynamics on k^o has been studied with great detail and has been experimentally confirmed for solvents with a permanent dipole.[83,85] Modeling of the relationship between k^o and the solvent dynamics involves the equation[84,85]

$$k^o = K_p \kappa_{EL} \tau_L^{-1} \left(\frac{\Delta G_{OS}^*}{4\pi RT} \right)^{1/2} \exp\left(\frac{-\Delta G^*}{RT} \right) \qquad (2)$$

where K_p is the precursor formation constant, κ_{EL} is the adiabicity parameter, τ_L is the solvent longitudinal relaxation time, ΔG_{OS}^* is the free energy of activation for outer sphere reorganization, and ΔG^* is the sum of the inner and outer sphere reorganization free energies of activation. The longitudinal relaxation time is related to the Debye relaxation time (τ_D) by[87]

$$\tau_L = \left(\frac{\varepsilon_\infty}{\varepsilon_s} \right) \tau_D \qquad (3)$$

where ε_∞ is the dielectric constant in the infinite frequency limit and ε_s is the static dielectric constant. For perfluoro(methylcyclohexane) at 20 °C, ε_∞ and ε_s are 1.859 and 1.85, respectively.[88] In cases where it is not known, τ_D can be estimated using the relation[87]

$$\tau_D = \frac{4\pi\alpha^3\eta}{k_B T} \qquad (4)$$

where α is the radius of the solvent molecule and η is the solution viscosity. The combination of equations 1 to 3 gives:

$$k^o = K_p \kappa_{EL} \frac{\varepsilon_s k_B T}{\varepsilon_\infty 4\pi\alpha^3\eta} \left(\frac{\Delta G_{OS}^*}{4\pi RT} \right)^{1/2} \exp\left(\frac{-\Delta G^*}{RT} \right) \qquad (5)$$

It has been reported previously that for ferrocene as the redox-active analyte and a variety of solvents ranging from chloroform to acetonitrile[78-80,89] (see also Figure 19) a plot of log k^o versus log τ_L shows the expected linear relationship. This shows that for ferrocene the term $K_p \kappa_{EL} \left(\Delta G_{OS}^*\right)^{1/2} \left(4\pi RT\right)^{-1/2} \exp\left(-\Delta G^*/RT\right)$ has only a small dependence on the solvent.

In order to apply equation 5 to the fluorous electrolyte solutions, it had to be determined to what extent the addition of electrolyte affects the viscosity of perfluoro(methylcyclohexane). Upon addition of 80 mM NBu_4BArF_{104} to perfluoro(methylcyclohexane), the diffusion coefficient of the solvent, as determined by DOSY ^{19}F NMR, decreased only 33% from 6.1×10^{-6} cm^2 s^{-1} to $(4.19 \pm 0.50) \times 10^{-6}$ cm^2 s^{-1}, which suggests that the addition of electrolyte only moderately increases the viscosity of the solution. Because the k^o determined in this work is 42 and 1.2×10^4 times smaller than for chloroform and acetonitrile, respectively, any effect of the electrolyte on the viscosity of perfluoro(methylcyclohexane) is comparatively small. Therefore, the published value for η of perfluoro(methylcyclohexane) of 1.56 cP[69] was used for all further calculations.

Using literature values for the viscosity and self-diffusion coefficient (6.2×10^{-6} cm^2 s^{-1}) of perfluoro(methylcyclohexane) along with equation 1, a radius of 2.26 Å is obtained for perfluoro(methylcyclohexane). This radius along with equations 3 and 4 gives τ_L as 56 ps at 20 °C and permits the comparison of the relationship of k^o and τ_L from this work with corresponding data for non-fluorous solvents. Figure 19 illustrates that the experimentally determined k^o for the oxidation of ferrocene in the fluorous electrolyte solution falls on the same line as k^o values for non-fluorous solvents from the literature. This shows that while k^o for the oxidation of ferrocene in the fluorous electrolyte solution is smaller than for solvents commonly used in electrochemistry, its value can be readily explained as the result of the large viscosity and molecular size of the solvent perfluoro(methylcyclohexane).

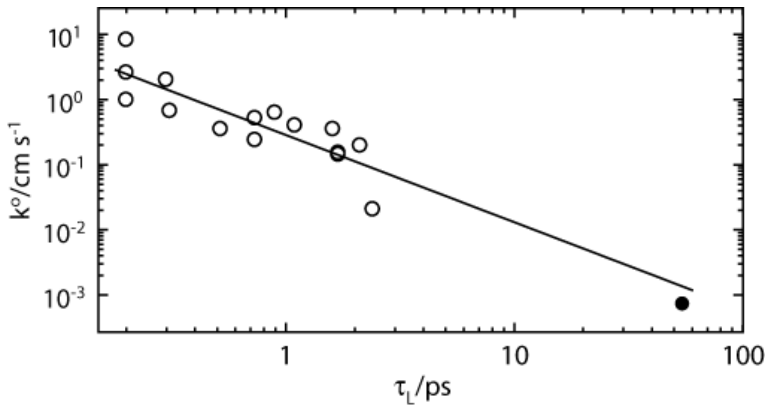

Figure 19: Log-log plot of k^o versus τ_L along with a linear fit for the literature data (open circles)[78-80,86,89] only. The fit is extrapolated to the τ_L for perfluoro(methylcyclohexane) (filled circle).

2.3.5 Dielectric Spectroscopy

While this is the first report on voltammetry with a cosolvent-free perfluorocarbon, the question arises whether these experiments were in fact performed with the least polar organic phase to date. Or does the addition of the NBu_4BArF_{104} electrolyte increase the polarity of the perfluoro(methylcyclohexane) phase to an extent that the electrolyte solution has a much more polar character than the fluorous solvent alone? This question may be addressed through dielectrometry, which provides the dielectric constant as a measure of the molecular dipole moments and polarizability of a sample. Because of the inherent ionic conductivity of electrolyte solutions, the dielectric properties of the fluorous media discussed here cannot be determined in the frequency range around 100 kHz, which is typically used for conventional dielectrometry. Instead, dielectric spectroscopy in the GHz range was used in this study to assess the polarity of the electrolyte solution.[90-93] Since relevant dynamic processes occur in the ps and ns range, the static dielectric constant ε can be determined by extrapolation of the real component, $\varepsilon'(\nu)$, of the frequency-dependent complex dielectric permittivity, $\tilde{\varepsilon}(\nu)$, from the GHz range to zero frequency. $\tilde{\varepsilon}(\nu)$ is given by[90-93]

$$\tilde{\varepsilon}(\nu) = \varepsilon'(\nu) - \sqrt{-1}\,\varepsilon''(\nu) \qquad (6)$$

where ε'(ν) stands for dielectric dispersion, and the imaginary component ε"(ν) is the dielectric absorption. Because ε"(ν) is related to ε'(ν), it does not carry independent information and will not be discussed here.

As Figure 20 shows, ε'(ν) of solutions of the electrolyte salt NBu_4BArF_{104} in perfluoro(methylcyclohexane) in the frequency range 0.2 to 20 GHz exceeded ε'(ν) of the pure perfluorocarbon by no more than 6.5%. The linear extrapolation of ε'(ν) in the range from 0.2 to 5.0 GHz suggests a static dielectric constant of the electrolyte solution of 1.96 and of pure perfluoro(methylcyclohexane) of 1.89. The latter value is in good agreement with the literature value of 1.86.[66]

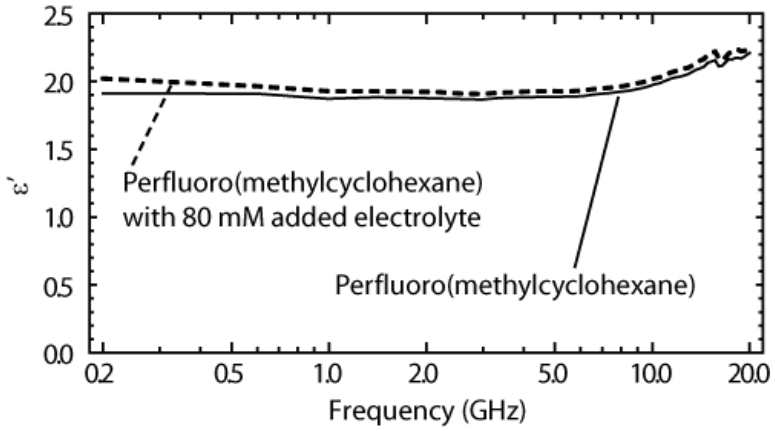

Figure 20: Dielectric dispersion spectrum of perfluoro(methylcyclohexane) with and without 80 mM NBu_4BArF_{104}.

2.4 Conclusions

Using the novel fluorous electrolyte salt NBu_4BArF_{104}, we demonstrated that voltammetry can be performed with a perfluorocarbon solvent without the use of a cosolvent. Even though fluorous phases are the least polar of all condensed phases, the observed CVs can be quantitatively fitted. The thus obtained k^o is 1.6 orders of magnitude smaller than the smallest k^o for oxidation of ferrocene in a set of common non-fluorous

solvents, for which k^o values cover a range of 2.4 orders of magnitude. Using Marcus theory, the small k^o can be readily explained as the result of the large radius and the high viscosity of perfluoro(methylcyclohexane). While ion pair formation in these fluorous phases is extremely strong and the formation of local pockets of higher polarity at the submolecular level is possible, dielectric spectroscopy confirms that the addition of electrolyte has only a minimal effect on the overall polarity of the fluorous electrolyte solutions.

The unique solvent environment of fluorous phases should provide an interesting medium for further experimentation. We are currently investigating the use of fluorous media as new matrixes[94,95] for voltammetric and amperometric sensors as they are expected to exhibit selectivity patterns differing significantly from those of conventional hydrophobic phases[53,55,96] and have the potential to reduce chemical and biological fouling. Also, in view of a further extension of the already large solvent window, we are exploring the electrochemistry of different perfluorinated and partially fluorinated solvents.

2.5 Supporting Information

2.5.1 Differential Scanning Calorimetry (DSC)

The glass transition temperature of NBu_4BArF_{104} was determined using a Q1000 Thermal Analyzer (TA Instruments, New Castle, DE, USA). The sample was allowed to thermally equilibrate at 25 °C for 5 min, cooled to –80 °C at a rate of 20 °C/min, allowed to thermally equilibrate for 5 min, heated to 100 °C at a rate of 20 °C/min, allowed to thermally equilibrate for 5 min, cooled to –80 °C at a rate of 20 °C/min, allowed to thermally equilibrate for 5 min, and then heated to 100 °C at a rate of 20 °C/min. The glass transition temperature was calculated from the observed heat flow profile during the final temperature ramp. See Figure 21 for the resultant DSC curve.

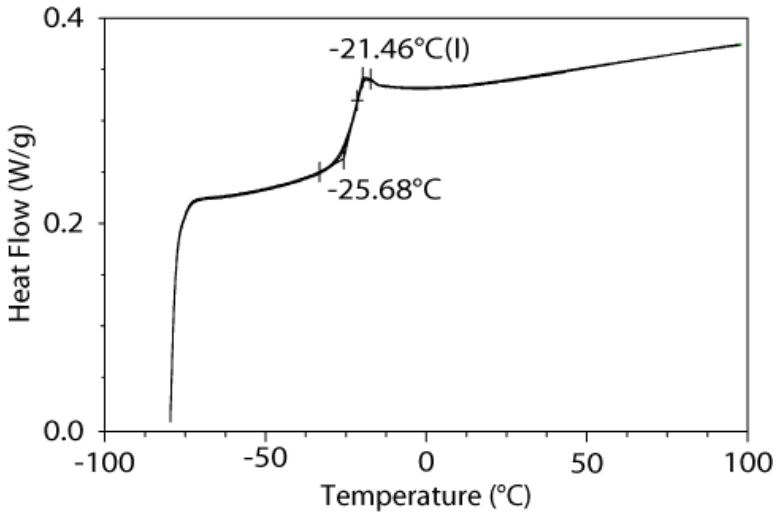

Figure 21: DSC curve for the final temperature ramp as described above: scan rate = 20 °C/min.

2.5.2 Correction of Solution Resistance Effects

The resistance of the fluorous electrolyte solutions was large enough to cause distortion in the measured voltammograms due to *i*R drop. The effect of ohmic distortion was

corrected from the voltammograms post-experiment by subtracting the *i*R drop at each data point from its potential. The solution resistance was determined by normalization of the CVs relative to the diffusion-limited current and least-squares fitting of the resistance value that gave the best overlap of all normalized CVs. Figure 22 shows the CVs after normalization and resistance correction. The resistance determined using this method was 120 MΩ. The resulting resistance-corrected CVs were then fitted to determine the kinetic parameters of the system, as described in the main text.

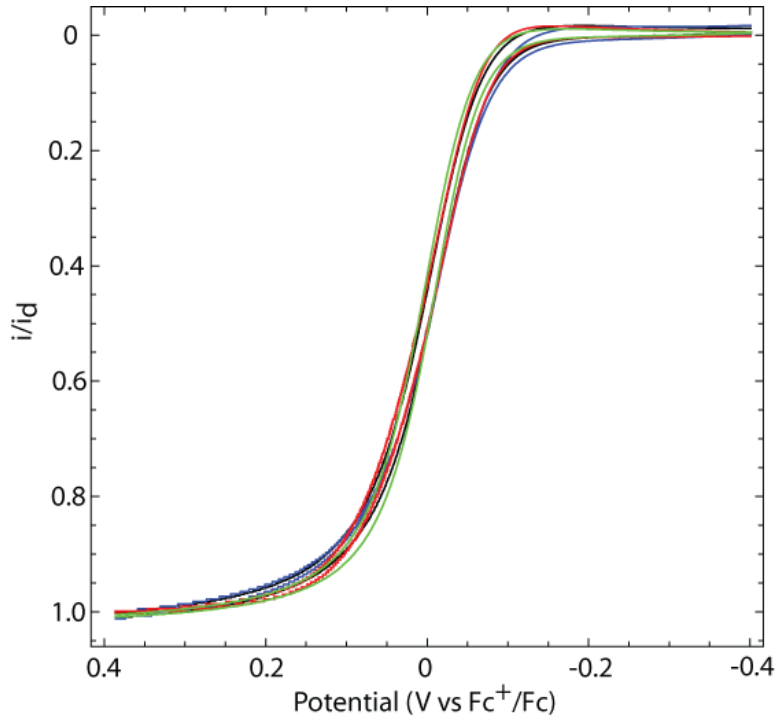

Figure 22: CVs of several concentrations of Fc in 80 mM NBu_4BArF_{104}/ perfluoro(methylcyclohexane): scan rate = 10 mV/s, T = 21 °C. Red = 5.43 mM, green = 2.72 mM, black = 1.63 mM, blue = 0.679 mM. Data is corrected for iR distortion using the method described above.

2.5.3 Determination of the Oxidation Limit of NBu_4BArF_{104}/perfluoro(methylcyclohexane)

In the voltammogram of a NBu_4BArF_{104}/perfluoro(methylcyclohexane) solution shown in Figure 23, measured in the wide range from –2.30 to 7.45 V vs Fc^+/Fc, a peak of relatively low intensity was observed with a half-wave potential at +1.9 V vs Fc^+/Fc, suggesting that the oxidative limit is caused by a species of comparatively low concentration and not the solvent itself.

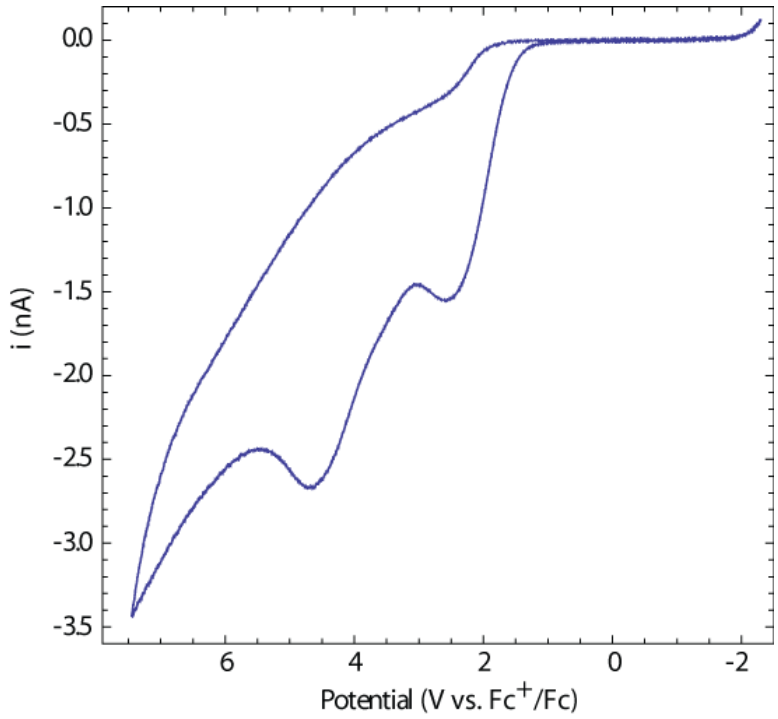

Figure 23: Oxidation limit of 80 mM NBu_4BArF_{104}/ perfluoro(methylcyclohexane): scan rate = 100 mV/s, T = 21 °C.

2.5.4 Cyclic Voltammetry of Ferrocene-Free Electrolyte Solution

A voltammogram of 80 mM NBu_4BArF_{104}/perfluoro(methylcyclohexane) measured in the range of –1.1 to 0.9 V vs. Fc^+/Fc (Figure 24) does not confirm the formation of an adsorbed layer since peaks indicative of adsorption or desorption events were not

observed. However, the formation of such a layer cannot be excluded entirely since a particularly strongly adsorbed layer might not be desorbed in the potential range accessible.

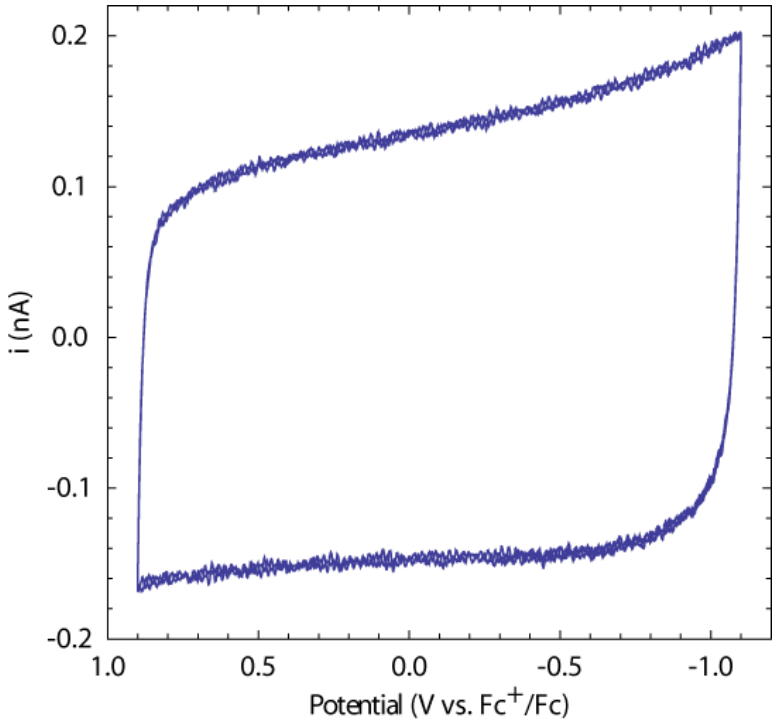

Figure 24: Cyclic voltammograms of 80 mM NBu_4BArF_{104}/ perfluoro(methyl-cyclohexane) showing absence of a desorption peak: scan rate = 10 V/s, T = 21 °C. Depicted are the third, fourth, fifth, and sixth segments of a CV, showing excellent overlap between the third and fifth as well as the fourth and sixth segments.

3 CHAPTER THREE

Minimizing Hazardous Waste in the Undergraduate Analytical Laboratory: A Microcell for Electrochemistry

In part from:

Olson, E. J.; Bühlmann, P. "Minimizing Hazardous Waste in the Undergraduate Analytical Laboratory: A Microcell for Electrochemistry" *Journal of Chemical Education*, **2010**, 87, 1260-1261.

Adapted with permission from the Journal of Chemical Education, 2010, 87, 1260.

Reducing the volume of chemical waste is a fundamental principle of green chemistry. However, many experiments in the undergraduate analytical teaching laboratory ask for relatively large samples to achieve reasonable accuracy and precision. We developed a simple electrochemical cell that requires only 0.20 mL of sample to reliably produce ideally shaped cyclic voltammograms. The cell can be easily disassembled for cleaning and polishing of the working electrode.

3.1 Introduction

Working toward greener experiments is imperative for responsible chemistry instructors[97,98] but the reduction of waste in analytical teaching laboratories is often overlooked.[99] For example, voltammetry experiments typically require tens of milliliters to accommodate the working, reference, and auxiliary electrodes.[31,100] This results in the consumption of significant amounts of solvent, analyte, and electrolyte, especially in large classes. Small volume adapters designed for use in teaching laboratories are commercially available, but their use only reduces samples to approximately 2 mL.[101] Moreover, typical microcells are either difficult to assemble or require the use of microfabrication techniques,[102,103] making electrode cleaning for repeated use complicated. Therefore, we developed the readily reusable but attractively simple microcell shown in Figure 25 and have used it in our laboratory for undergraduate research with great success.

3.2 Cell Details

The microcell consists of a 3-cm segment of 12-mm i.d. glass tubing and a poly(chlorotrifluoroethylene) top and bottom cap with four and one hole, respectively. Inserted through the top cap is a commercial 10-μm diameter platinum microelectrode, which serves as the working electrode. Also inserted into the sample solution through the

top cap is a reference electrode consisting of a silver chloride-coated silver wire inside a Teflon tube that is plugged at the lower end with tightly packed cotton and filled with 1 M KCl. The remaining two holes in the top cap are reserved for purging the sample of oxygen using a stream of nitrogen or argon gas. Purging is optional and is typically not necessary when analytes of medium or high concentrations are measured. A standard Au disk macroelectrode is used as the auxiliary electrode and inserted through the bottom cap of the cell. All junctions are sealed with Viton o-rings.

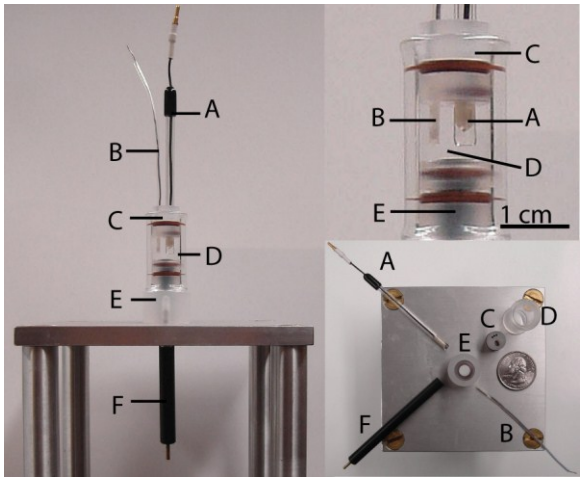

Figure 25: Photographs of the cyclic voltammetry microcell: (A) Platinum working microelectrode; (B) Ag/AgCl reference electrode; (C) Top cap; (D) Glass cell body; (E) Bottom cap; (F) Au disk auxiliary electrode (see the supplement for a schematic and a detailed description of the cell).

Using this cell, voltammograms were readily obtained with sample volumes as small as 0.20 mL, at which point the working and auxiliary electrodes are separated by approximately 2 mm. Much smaller volumes were found to be possible but rather impractical, as the samples did not form a layer of uniform thickness at the bottom of the cell. As shown in the supplement, a typical example of a voltammogram of aqueous potassium ferrocyanide with 100 mM potassium chloride as background electrolyte

obtained with this cell exhibits exactly the same features as observed with large sample cells.

A common example of a non-aqueous system often used in undergraduate laboratories to teach principles of voltammetry is ferrocene in acetonitrile.[41] We tested our cell for use in this system and obtained ideal voltammograms (see supplement). Note however that measurements in organic solvents require the use of o-rings that will not swell in the chosen solvent.

In conclusion, our cell design reduces the consumption of sample to approximately 0.20 mL from the several milliliters that is common for typical cells. This not only reduces the amount of hazardous waste, but it also reduces the cost of reagents. The latter should be particularly useful for experiments involving enzymes and other biological materials.

3.3 Supplement

3.3.1 Detailed Cell Construction

The developed microcell consists of a 3-cm segment of 12-mm i.d. glass tubing and a poly(chlorotrifluoroethylene) top and bottom cap with four and one hole, respectively. Inserted through the top cap is a 10-μm diameter platinum microelectrode (BAS; West Lafayette, IN), which serves as the working electrode. Inserted into the sample solution through the top cap is a reference electrode consisting of a silver chloride-coated silver wire inside a Teflon tube that is plugged at the lower end with tightly packed cotton and filled with 1 M KCl. A drawing of the reference electrode is shown in Figure 26. The cotton plug, which provides a liquid junction to the sample solution, is washed thoroughly with water and subsequently with 1 M KCl to prevent cell contamination. Provided that this reference electrode is stored in 1 M KCl when not in use, it can be used repeatedly. Glass wool is an alternative to cotton but it is much harder to pack into the narrow Teflon tube. The remaining two holes in the top cap are reserved for purging the sample of oxygen using a stream of either nitrogen or argon. Purging is optional and is

typically not necessary when analytes of medium or high concentrations are measured. A standard Au disk electrode (BAS) is used as the auxiliary electrode and is inserted with a tight fit through the bottom cap of the cell. Note that the chemical composition of the auxiliary electrode is not critical provided that the reaction at the electrode does not significantly contaminate the sample (e.g., by oxidation of the electrode, releasing soluble metal ions into the sample). All junctions are sealed with appropriately sized Viton o-rings (DuPont; Wilmington, DE).

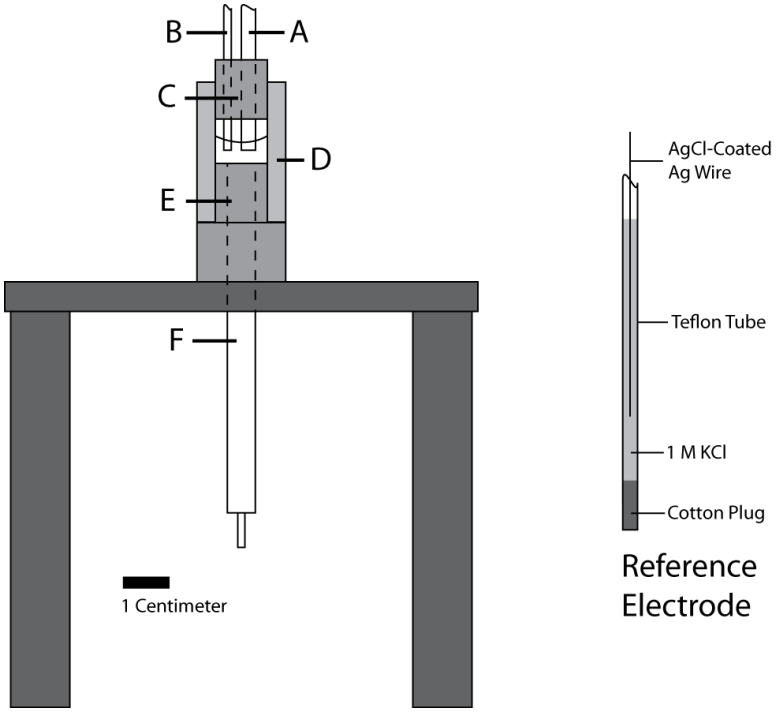

Figure 26 Scaled schematics of the microcell (left) and the reference electrode (right). The cell components are labeled as follows: (A) 10-μm diameter platinum working microelectrode; (B) Ag/AgCl reference electrode; (C) top cap; (D) glass cell body; (E) bottom cap; (F) Au disk auxiliary electrode.

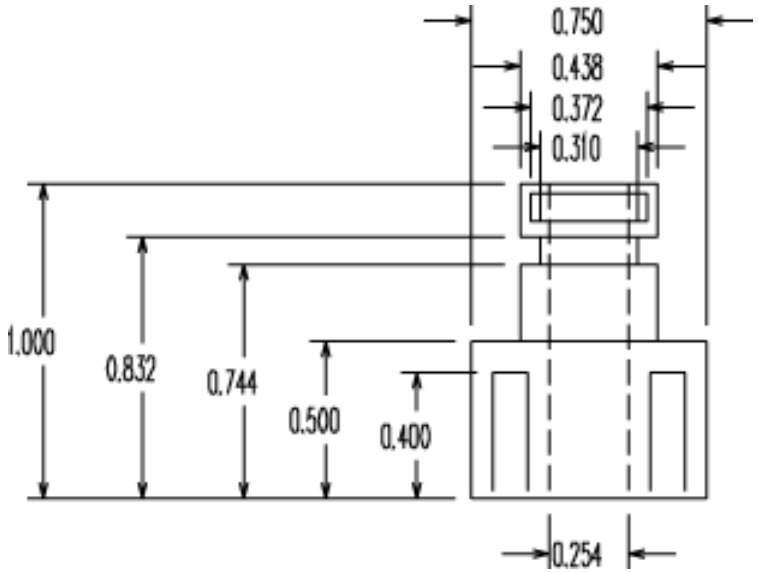

Figure 27: Machining dimensions for the bottom poly(chlorotrifluoroethylene) cap. All dimensions are in inches.

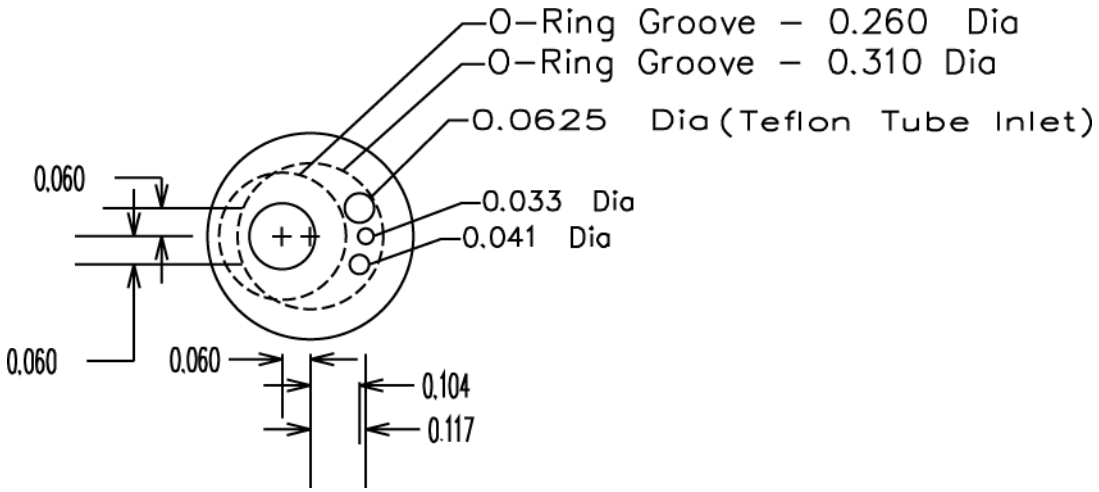

Figure 28: Machining dimensions for the top poly(chlorotrifluoroethylene) cap. All dimensions are in inches. Note that the 0.310 inch diameter O-ring groove is external, while the 0.260 inch diameter groove is inside the 0.120 inch diameter hole for the working electrode.

3.3.2 Microelectrode Polishing Procedure

All polishing equipment was purchased from Buehler (Lake Bluff, IL). The platinum microelectrode was polished using Microcloth polishing pads, first with 5.0 μm Micropolish II deagglomerated alumina, then with 1.0 μm and 0.25 μm MetaDi Supreme polycrystalline diamond suspension, and lastly with 0.05 μm Micropolish II deagglomerated alumina. The polished electrode was then ultrasonicated in a Triton X-100 detergent solution for 3 minutes, rinsed, and dried. When we omitted the ultrasonication step, limiting currents decreased by approximately 5%, but the precision of the experiments was hardly affected. Water used for the detergent solution and for rinsing the electrode was deionized and charcoal-treated (≥18.2 MΩ cm specific resistance) with a Milli-Q PLUS reagent-grade water system (Millipore, Bedford, MA). The Au disk auxiliary electrode was polished with 5.0 μm Micropolish II deagglomerated alumina, rinsed well, and dried.

3.3.3 Cyclic Voltammetry (CV) of Ferrocyanide

Ferrocyanide was chosen because it is an example of an inexpensive and well-behaved electrochemically reversible analyte.[31] It is also an analyte of interest in hazardous waste remediation, particularly of nuclear waste.[104] Ferrocyanide is oxidized to ferricyanide in the one-step, one-electron transfer shown in reaction (1), with a formal reduction potential, E°', of approximately 0.41 V vs. NHE (normal hydrogen electrode) in solution of ionic strength of near 0.1 M.[105]

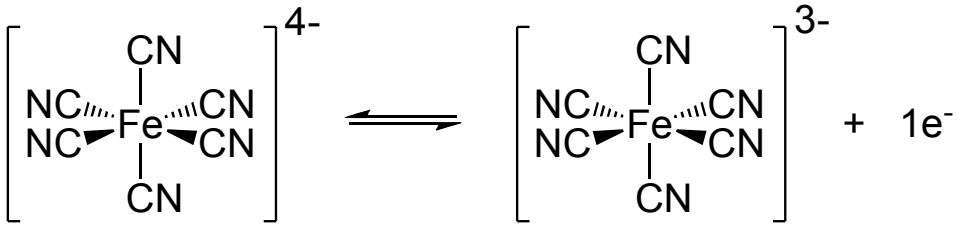

(1)

A representative voltammogram of ferrocyanide obtained using this cell is shown in Figure 29. This voltammogram shows the ideal sigmoidal shape expected at a microelectrode. The shape of a voltammogram at a microelectrode is the result of the hemispherical concentration profile of the analyte diffusing to the electrode. In contrast, the diffusion profile at a macroelectrode is linear, resulting in peak-shaped voltammograms. A more detailed discussion of the CV shapes along with a pictoral representation of each process can be found in reference [41]. Importantly, in a microelectrode CV one can immediately recognize that the electrode was not polished properly if for a reversible redox couple the unique sigmoidal curve does not have the proper shape or is not observed at the proper potential. As also discussed in reference [41], the limiting current of a voltammogram obtained at a microelectrode is proportional to the concentration of the analyte. This ideal linear behavior is shown in the inset of Figure S4. The E°' of a reversible reaction at a microelectrode can be obtained from the potential at which the current has reached half of its plateau value.[1] In our experiments, an E°' of 0.194±0.007 V vs. Ag/AgCl was determined. To express the potential relative to the NHE, one adds 0.197 V, thus arriving at an E°' of 0.391 V vs. NHE.[1] This is in good agreement with the reported literature value of 0.41 V.[105]

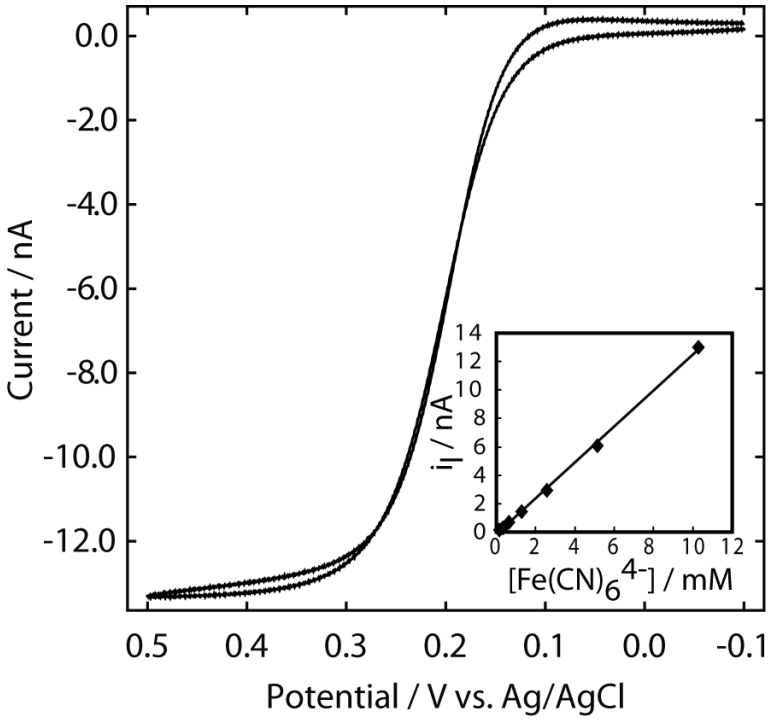

Figure 29: Cyclic voltammogram of 10.3 mM $Fe(CN)_6^{4-}$ in 0.1 M KCl obtained using the microcell discussed in this article: scan rate = 100 mV/s, T = 21 °C. The inset shows the linear relationship between the limiting current and the $Fe(CN)_6^{4-}$ concentration.

Upon close inspection, the voltammogram in Figure 29 shows slightly different shapes in the forward and reverse scan. This is caused by the formation of Prussian Blue at the Pt electrode surface.[106,107] While the formation of Prussian Blue on the electrode surface does not affect the linearity of the calibration curve for scan rates of 100 mV/s, the slow deposition of Prussian Blue will decrease the current upon extended cycling or for slow scan rates. This deposition makes regular polishing of the electrode necessary for quantitative analysis. It is interesting to note that Prussian Blue intentionally electrodeposited onto electrodes catalyzes the reduction of hydrogen peroxide which has been used to prepare sensors for hydrogen peroxide and glucose.[108,109]

3.3.4 CV of Ferrocene in Acetonitrile

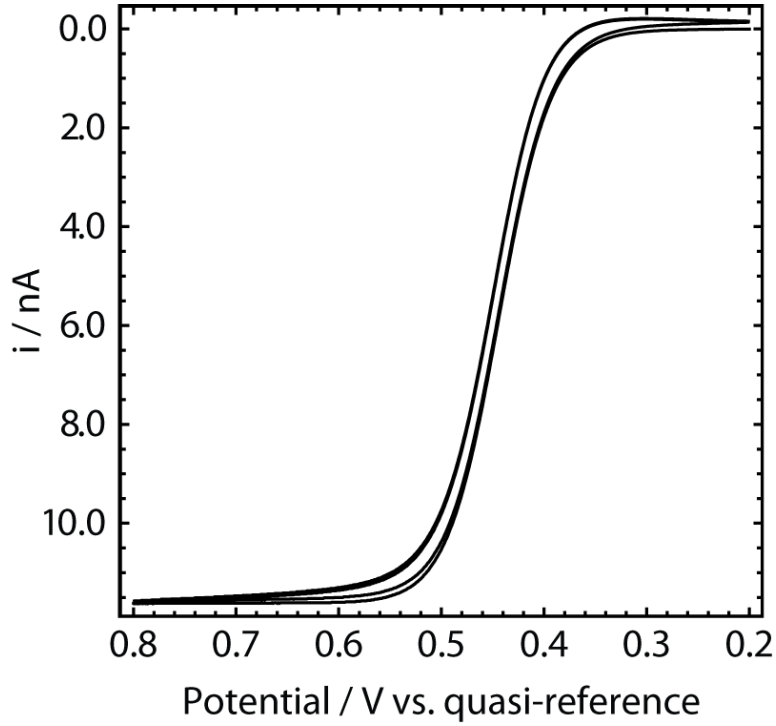

Figure 30: Cyclic voltammogram of 3.0 mM ferrocene in acetonitrile/0.1 M tetrabutyl-ammonium perchlorate: scan rate = 100 mV/s, T = 21 °C.

3.3.5 Concentration Profiles and Currents at Microelectrodes

When determining the thickness of the diffusion layer at a microelectrode, it is more convenient to consider the case of a potential step rather than the potential sweeps characteristic of cyclic voltammetry. Assuming that mass transfer is governed by hemispherical diffusion and that the concentration (C) of an electroactive species after a potential step is 0 M at the electrode surface and C^o at infinite distance from the electrode, it can be shown that the concentration of this species at distance r from the microelectrode and at time t after the potential step is given by

$$C(r,t) = C^o\left[1 - \frac{r_o}{r} erfc\left(\frac{r - r_o}{2(Dt)^{1/2}}\right)\right] \quad (1)$$

where C^o is the bulk concentration of the electroactive species, r_o is the radius of the microelectrode, and D is the diffusion coefficient of the electroactive species (Equation 5.2.22 in ref. [1]). At infinite time after the potential step, equation 1 reduces to

$$C(r,t) = C^o\left[1 - \frac{r_o}{r}\right] \quad (2)$$

For an electrode radius of 5 μm, it follows from Equation 2 that the concentration of the electroactive species at a distance of 0.5 mm from the electrode surface at infinite time is 99% of the bulk concentration. The depletion of the electroactive species in the case of a potential sweep rather than a potential step is even smaller since the applied potential in the early stage of the sweep is not large enough to reduce C to 0 M.

The conditions observed in the microcell described in this article are very similar to those observed for scanning electrochemical microscopy (SECM) in positive feedback mode.[1] Using models developed for SECM, one can calculate the increase in current expected when the working (micro)electrode approaches the auxiliary electrode [110]. For a microelectrode laterally covered with an insulator that has a much larger thickness than the radius r_o of the microelectrode, the ratio of the current observed at a distance r between the two electrodes compared to infinite separation is calculated using the following equation

$$\frac{i_r}{i_\infty} = 1 + \frac{2\ln 2}{\pi(r/r_o)} \quad (3)$$

where i_r is the current at distance r, and i_∞ is the current when the microelectrode is infinitely far away from the auxiliary electrode (Equation 6 from ref. 110). For the case of a 5 μm radius microelectrode, an increase in current of only 0.5 % is predicted at a distance of 0.5 mm, and 0.1% is predicted for an electrode separation of 2 mm.

In the event that one would like to use macroelectrodes both as the working and auxiliary electrodes, the magnitude of the thin-layer effect can be estimated by thin-layer cell theory. In this case, the current as a function of time is given by

$$i(t) = \frac{4nFADC^o}{l} \sum_{m=1}^{\infty} \exp\left[\frac{-(2m-1)^2 \pi^2 Dt}{l^2}\right] \quad (4)$$

where n is the number of electrons transferred, F is Faraday's constant, A is the electrode area, D is the diffusion coefficient of the analyte, and l is the cell thickness. For further discussion on this issue, see Section 11.7 in Reference [1]. Considering a one-electron transfer and a diffusion coefficient of 10^{-5} cm^2 s^{-1}, the current predicted at 100 seconds for two electrodes separated by 1.5 mm is 99% of the current for infinite electrode separation. Note that Equation 4 requires very large values of m to give numerically accurate predictions for large values of l or small values of t. This suggests that this cell could be used with a macroelectrode as working electrode. In this case, however, care must be taken with long experimental times or very small sample volumes to avoid thin-layer effects.

4 CHAPTER FOUR

Interaction of a Weakly Acidic Dinitroaromatic with Alkylamines: Avoiding the Meisenheimer Trap

In part from:

Olson, E. J.; Xiong, T. T.; Cramer, C. J.; Bühlmann, P. "Interaction of a Weakly Acidic Dinitroaromatic with Alkylamines: Avoiding the Meisenheimer Trap" *Journal of the American Chemical Society*, **2011**, 133, 12858-12865.

Adapted in part with permission from the Journal of the American Chemical Society, 2011, 133, 12858.

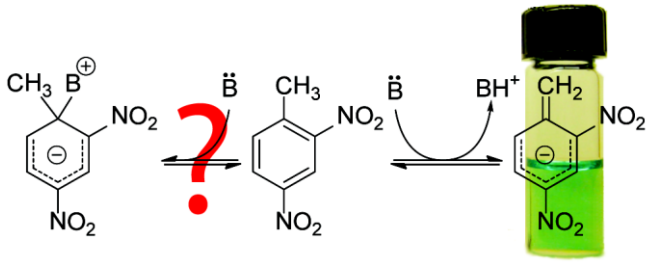

Polynitroaromatics are well known to form anionic σ-complexes (Meisenheimer complexes). The formation of such complexes was assumed in the past to explain the blue color of solutions of 2,4-dinitrotoluene (DNT) and amines. However, this work shows that caution is warranted to avoid the hasty misidentification of Meisenheimer complexes. ^{1}H NMR spectra exhibit no significant shifts in the positions of the DNT protons, indicating that the majority of DNT species in solutions of DNT and amines retain their aromaticity. Density functional calculations on DNT–ethylamine complexes suggest that Meisenheimer complexes are sufficiently high in free energy so that they make up only a very small fraction of the full equilibrium population. While principal component analysis of the UV/Vis spectra of the DNT–amine solutions reveals that only one absorbing species of significant concentration is formed, quantitative fits of Job's plots show that 1:1 association of DNT with the amines alone cannot explain the visible absorption spectra. Instead, the Job's plots can be accurately interpreted by deprotonation of DNT, with the amines acting as bases. The deprotonation equilibria lie far on the side of the unreacted DNT, preventing the detection by NMR of the deprotonated minority species that gives the solutions their strong blue color. The analysis of systems with DNT and *n*-butylamine, diethylamine, triethylamine, or benzylamine provides a consistent pK_a of DNT in dimethyl sulfoxide of 15.3±0.2.

4.1 Introduction

The analysis of 2,4-dinitrotoluene (DNT) is of interest because of its role as an intermediate in the synthesis of polyurethane and its hepatocarcinogenicity.[111] However, the key incentive for developing chemical sensors for DNT lies in the detection of explosives[6,112,113] since DNT is a common impurity in the widely used explosive 2,4,6-trinitrotoluene (TNT).[14] While various sensing schemes for the detection of TNT itself have been reported, including several ones based on the formation of colored complexes,[10-13] the detection of its impurity DNT is often preferable for analytical purposes as its much higher volatility allows a much more sensitive detection. Indeed, dogs trained to find TNT smell primarily DNT and not TNT. Not surprisingly, chemical abstracts lists nearly 4000 entries for DNT.

For the design of DNT receptors, several modes of intermolecular interactions are conceivable. The nitro groups of DNT have been reported to bind to hydrogen bond donors and metal cations,[30,114] and there have been several publications suggesting that amines form anionic σ-complexes with DNT (often referred to as Meisenheimer complexes).[115-118] With a view to optical sensors, it appeared particularly interesting that solutions of DNT and alkylamines have a deep blue color absent to solutions of DNT or alkylamines alone.

Meisenheimer complexes have been the subject of a great deal of research[119-121] since their structure was first proposed in 1900 by Jackson and Gazzolo[122] and chemical evidence for their composition was reported by Meisenheimer in 1902.[123] These complexes result from the addition of a nucleophile to an electron-deficient aromatic molecule. Formation constants have been determined for the complexes of a wide variety of electron-deficient aromatic molecules with many nucleophiles,[10,118,124-127] and several reviews discussing recent advances made in studying such complexes were published.[119-121] Relevant to the case of DNT is that, because of their strongly electron-withdrawing nitro groups, polynitroaromatic compounds readily form Meisenheimer complexes with strong nucleophiles.[116,117,119-121,128]

The molecular structure of these complexes proved difficult to elucidate for many years, but various studies in condensed phases using UV/Vis and NMR spectroscopy as well as X-ray crystallography eventually revealed that Meisenheimer complexes of polynitroaromatics consistently involve attachment of a nucleophile to an aromatic carbon in direct resonance with a nitro group.[119-121] Recently, the structure of the complex formed between 1,3,5-trinitrobenzene and methoxide has been explicitly determined in the gas phase by infrared multiphoton dissociation spectroscopy.[129] The current level of understanding indicates that strong nucleophiles result in a nearly tetrahedral geometry at the carbon center to which the nucleophile binds, while weaker nucleophiles bind in a more axial fashion with a much lesser effect on the geometry of the aromatic skeleton,[130] leading to some ambiguity as to the dividing line between a Meisenheimer complex and a more weakly interacting pair.

In contrast to the extensive record on Meisenheimer complexes in general, reports on the color reaction of DNT with amines have been few. Moreover, in view of the new results described in this contribution, some of the previously reported conclusions appear to be misleading. For example, in an investigation on the formation of a colored product in solutions from DNT and butylamine it was speculated that "dinitrotoluene, like other polynitroaromatics, is expected to form anionic sigma complexes with bases." No attempts were made to confirm the structure of these complexes.[116] Similarly, in a study of the reaction of methylamine and diethylamine with DNT in dimethyl sulfoxide (DMSO), the formation of Meisenheimer complexes was assumed only based on the analogy of similar complexes with trinitrobenzene.[117] Also, in a seminal study on the environmental fate of nitroaromatic compounds, DNT adsorption to natural clay materials with large surface concentrations of negative charges was studied. It was assumed that electron donor–acceptor (EDA) complexes were formed, but the possibility of deprotonation of DNT was not considered.[131] Arguably the most careful comment came from the developers of optical sensors based on poly(vinyl chloride) thin films doped with amines.[132] The authors did not explicitly comment on DNT complexes but

stated very generally that polynitroaromatics form either Meisenheimer complexes or their conjugated bases, thus at least considering alternatives. However, as in other reports on color reactions of TNT and DNT too,[133] quantitative studies were not performed, and significant differences in the reactivities of TNT and DNT were not implied.

In this contribution we show that DNT surprisingly does not form any appreciable amounts of Meisenheimer complexes with various alkylamines. Density functional calculations confirm the experimental conclusion that Meisenheimer complexes exist in solution as an extreme minority species at most. It is shown that the deep blue color of solutions of DNT and alkylamines in *N,N*-dimethylformamide (DMF) and DMSO is due to the deprotonation of DNT. The characteristic color of the deprotonated DNT was used to determine the pK_a of DNT in DMSO. The question whether hydroxide forms a complex with DNT or simply deprotonates DNT was also addressed.

4.2 Results and discussion

4.2.1 Effect of solvent polarity

A typical visible spectrum of a DNT–amine solution in DMSO is shown in Figure 31. Solutions of DNT with all amines studied were found to have the same broad absorbance band with a maximum at 652 nm, and in the range of 400 to 800 nm all spectra overlapped with one another almost perfectly. To confirm that only one colored reaction product is formed in all solutions containing DNT and the different amines, sets of DNT–amine spectra were subjected to principle component analysis.[134] This confirmed that within experimental error only two species were responsible for the absorption in the range from 400 to 800 nm (98.7% of the spectra is described with these two components). Because DNT absorbs visible light near 400 nm, one principle component (2.2%) of the visible spectra can be attributed to DNT. The second (96.5%) principle component can then be attributed to the product of the interaction of DNT with the amine.

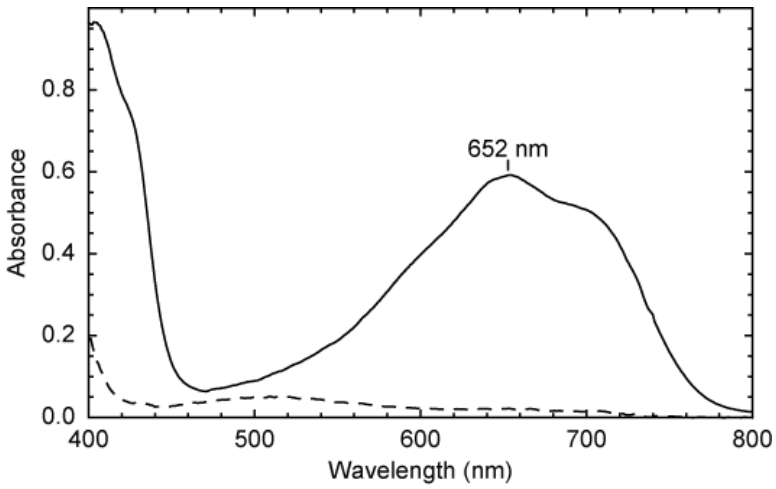

Figure 31: Visible spectrum of 10 mM DNT in DMSO before (dashed) and after (solid) the addition of 10 mM diethylamine. T = 20 °C.

A large effect of solvent polarity was observed. The absorption associated with DNT deprotonation was observed in both DMSO and DMF but not in ethyl acetate or acetonitrile. In mixtures of either DMSO or DMF with ethyl acetate or acetonitrile, the absorption from the complex decreased sharply with the addition of even fairly small amounts (<20%) of the latter solvents. This observation is consistent with reports of Andrabi and Atehar, who reported that the formation constant of the complex of DNT with diphenylamine shows a logarithmic correlation with the π* solvent polarity parameter of the solvent.[118] This relationship is true for complex formation in both protic and aprotic solvents. Because of the large dependence of the formation constant on the polarity of the solvent, DMSO was used for all subsequent experiments.

4.2.2 The Special Case of Hydroxide

The literature suggests that increased Bronsted basicity increases the stability of Meisenheimer complexes. In the case of the addition of strong nucleophiles such as methoxide to trinitrobenzene, the trinitrobenzene carbon attacked by the nucelophile was shown to take a geometry close to sp^3. In contrast, weak nucleophiles such as bromide or

iodide bind to trinitrobenzene in a more axial fashion, leaving the trinitrobenzene carbon with a geometry close to sp^2.[130] Therefore, the question arose as to whether anionic species such as alkoxides or hydroxide form Meisenheimer complexes with DNT. As shown with a ^{1}H NMR titration of a DMSO-d_6 solution of DNT (100 mM) with tetrabutylammonium hydroxide, DNT behaves quite differently. Before the addition of hydroxide, DNT has aromatic protons at 7.66 (d, 1H), 8.31 (d, 1H), and 8.60 (s, 1H) ppm while the methyl peak appears at 2.63 ppm (3 H). Upon addition of a substoichiometric OH^- concentration, additional peaks were observed at 4.59 (s, 1H), 5.62 (s, 1H), 6.29 (d, 1H), 6.72 (d, 1H), and 8.56 (s, 1H) ppm, and upon addition of a full stoichiometric amount of OH^- the original DNT peaks disappeared, leaving only the newly formed peaks. The addition of a small amount of D_2O at this point did not affect the newly formed peaks, but acidification with 5 M D_2SO_4 led to the disappearance of the OH^--induced peaks and the reappearance of the original aromatic peaks of DNT. However, the D_2SO_4 addition did not lead to the reappearance of the DNT methyl peak. This observation can be interpreted as follows: Addition of OH^- led to deprotonation of the methyl group. Due to restricted rotation around the exocyclic carbon–carbon bond, the two CH_2 protons were observed as two distinct signals at 4.59 and 5.62 ppm, while all three aromatic protons shifted upfield; these assignments are supported by density functional theory (DFT) calculations reported in Section 2.7. The addition of D_2O to the solution of the DNT anion did not result in any observable H/D exchange, but the subsequent addition of D_2SO_4 did not only result in the formation of CH_2D but also a quickly following exchange of all methyl hydrogens to give a CD_3 group. These observations clearly show that, in DMSO, OH^- prefers to deprotonate DNT rather than produce a Meisenheimer complex by binding to DNT.

4.2.3 Interaction of DNT with Alkylamines

^{1}H NMR spectroscopy also gives some insight into the interaction of DNT with amines. The ^{1}H NMR titration of 50 mM DNT with diethylamine in DMSO-d_6 showed

no observable shift in the peak position or integrals of the aromatic and amine protons. Rather, the peaks corresponding to these protons only broadened very slightly, even with a large excess of the added amine. This suggests that there is a fairly quick rate of exchange between the different forms of DNT, and that, at equilibrium, either the conformations of the different DNT species are structurally very similar or that free, electrically neutral DNT remains the dominant species. As will be shown in the following, the latter is consistent with the formation of a very small concentration of deprotonated DNT.

4.2.4 Model for Fitting of Job's Plots

The possibility of binding of amines to DNT was further studied using Job's method of continuous variation[4,128,135] by fitting of the visible absorption at 652 nm. For each amine, several solutions were prepared to contain DNT and an amine at concentrations that added up to a constant value for all solutions of a plot. To improve the accuracy of each fit, Job's plots were prepared for several total concentrations. Job's method was initially employed because, in cases where only one complex of n:m stoichiometry is formed, it can reveal the the ratio of n and m by the occurrence of a maximum in the absorbance of the complex at a host:guest ratio of n:m. However, as discussed in the following, the interpretation of a Job's plot is more complicated when the equilibrium under study involves formation of more than one product.

Experimental Job's plots for different total concentrations of DNT and benzylamine are shown in Figure 32. The three curves shown in this figure and the Job's plots for *n*-butylamine, diethylamine, and triethylamine all share three characteristic features: (i) an absorption maximum was observed at a mole fraction of DNT of 0.5, indicating an equimolar stoichiometry for the reaction of DNT with the amines, (ii) none of the plots exhibited a sharp maximum, as it would be expected for the exclusive formation of a very stable complex, and (iii) all plots exhibited (with respect to the maximum absorbance at the 0.5 mole fraction of DNT) much larger absorbances around the 0.25 and 0.75 mole

fraction than would be expected for the formation of one type of complex with n:n stoichiometry (such as in the case of the formation of a Meisenheimer complex); as a result, the Job's plots are more reminiscent of a semicircle than the more commonly encountered inverted parabola.[4]

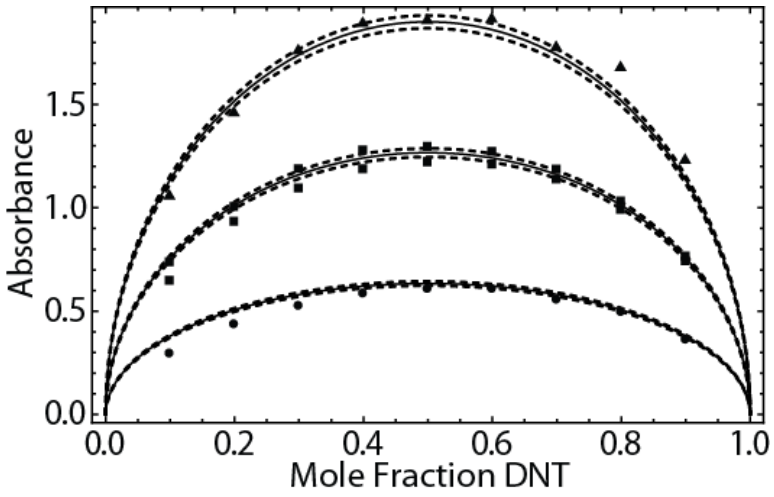

Figure 32: Job's plots and corresponding fits for the system of DNT and diethylamine (total concentration of DNT and diethylamine for the data fitted with the bottom, middle, and top curve were 20, 40, and 60 mM, respectively). The solid curves indicate the best fit while the dashed curves indicate the calculated 95% confidence intervals. T = 22 °C. Fitted parameter: $K_{Eq} = 2.943 \times 10^{-5}$.

The unusual semicircular shape of the Job's plots is consistent with a reactant:product ratio of 2:2 (such as for a deprotonation reaction) and a rather small equilibrium constant, while the common shape reminiscent of an inverted parabola shape is observed for a reactant:product ratio of 2:1 (such as when a host, H, and a guest, G, form HG or H_2G_2 host–guest complexes). For example, in the limit of weak complexation and 2:2 reactant:product stoichiometry, the Job's curve rises to 79% of its maximum value at a mole fraction of 0.2 (and, due to the symmetry of the curve, falls to 79% at 0.8). By contrast, the Job's curve characteristic for binding of one guest molecule to one host

molecule to give a HG complex (with a 2:1 reactant:product ratio) rises for the limit of weak complexation to 64% of its maximum at the same mole fractions. (Note that in the limit of weak complexation these percentages of maximum absorption do not depend on the actual equilibrium constant. For medium strengths of binding, the percentages become smaller for both reactant:product ratios, and for very strong binding, the Job's plot have a triangular shape.)[136]

The semicircle-type shape of the curves shown in Figure 2 strongly indicated the occurrence of a 2:2 reactant:product ratio. Indeed, various attempts to fit the experimental data with conventional models where n host molecules react with n guest molecules to form H_nG_n complexes failed because these models invariably overestimated the absorbance at the 0.5 mole fraction of DNT while simultaneously underestimating the absorbances at the 0.2 and 0.8 mole fractions of DNT. This complicated the determination of the stability of these complexes. The literature describes several fitting techniques developed to determine complex formation constants using Job's method for systems with a 2:1 reactant:product ratio.[128,137-140] However, these methods are insufficient for the determination of binding constants from experimental data in other cases. Therefore, a specific algorithm was developed in this work to fit experimental data such as those shown in Figure 2, as is described in the following.

Knowing that the reaction of DNT with an amine does not result in the simple formation of a 1:1 Meisenheimer complex or a 2:2 complex, and considering that OH^- was found to result in DNT deprotonation, the possibility of H^+ transfer from DNT to the amines was considered. This process is described by the following equations:

$$c^o_{\mathrm{DNT}} = c_{\mathrm{DNT}} + c_{[\mathrm{DNT\text{-}H}]^-} \tag{1}$$

$$c^o_{\mathrm{A}} = c_{\mathrm{A}} + c_{\mathrm{AH}^+} \tag{2}$$

$$K_{\mathrm{Eq}} = \frac{c_{[\mathrm{DNT\text{-}H}]^-} \times c_{\mathrm{AH}^+}}{c_{\mathrm{DNT}} \times c_{\mathrm{A}}} \tag{3}$$

where c^o_{A} and c^o_{DNT} are the total amine and DNT concentrations, respectively, the *c* terms stand for the concentrations of the free species A and DNT along with the proton transfer

products $[DNT\text{-}H]^-$ and AH^+ in solution, and K_{Eq} is the equilibrium constant for the proton transfer. Since principle component analysis had shown that the system contained only one species absorbing at 652 nm, the total absorbance at this wavelength could be obtained from the concentration and molar absorptivity of the deprotonated DNT and the optical pathlength, d:

$$A = \varepsilon d\, c_{[DNT-H]^-} \tag{4}$$

Solving equations 1–4 for the absorbance as a function of the mole ratio fraction of DNT, K_{eq}, ε, and the sum of c_A and c_{DNT} results in an equation that describes the Job's plots. This equation was used for preliminary efforts to fit the experimental Job's plots with Mathematica 7 (Wolfram Research, Champaign, IL, USA) using an embedded nonlinear regression algorithm. However, these fits showed a poor agreement between the reported pK_a values of the amines and the fitted K_{Eq} and an extremely inconsistent molar absorptivity of the deprotonated DNT for the Job's plots with the different amines. This could be explained by that fact that in the case of a deprotonation reaction in the limit of a small proton transfer equilibrium constant, the shape of the Job's curve when normalized to its maximum is independent of the stock concentrations, and simultaneous fitting of K_{EQ} and ε results in extremely large confidence intervals for both of these parameters.[136]

4.2.5 Determination of ε

To determine ε independently in a separate experiment, solutions containing 10 mM tetrabutylammonium hydroxide and DNT in a concentration range from 0.002 to 0.1 mM were prepared, and their absorbance was measured at 652 nm (see Figure 33). Based on the ^{1}H NMR spectra of these DNT–hydroxide solutions and the linearity of the plot in Figure 3, it was assumed that in these solutions DNT was completely deprotonated at all concentrations and, therefore, the concentration of deprotonated DNT in all solutions was equal to the total concentration of DNT. Linear regression gave the molar absorptivity of the deprotonated DNT as 11740±230 M^{-1} cm^{-1}.

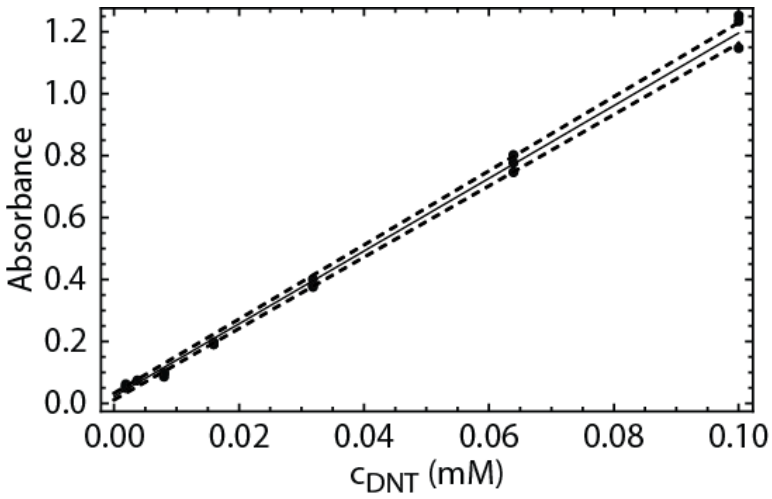

Figure 33: Absorbance of DNT in a 10 mM solution of tetrabutylammonium hydroxide in DMSO at 20 °C. The solid line represents the linear fit while the dashed curves indicate 95% confidence intervals.

Determination of K_{Eq}

With the fixed value for ε, the nonlinear regression was again used to fit the Job's plots for several amines and determine numerical values for the parameters K_{Eq}. As an example, the experimental Job's plots for diethylamine at three different total concentrations along with the corresponding fits (solid lines) are shown in Figure 2. Note that all 32 experimental points (i.e., all three Job's plots) were fitted simultaneously to determine one single K_{Eq} value. (The experimental Job's plots and fits for the other amine systems may be found in the Supplementary Information.) The good fits of multiple Job's plots with one single value of K_{Eq} support the adequateness of our model.

Table 1: Proton Transfer Equilibrium Constants for DNT and Various Amines in DMSO at 20 °C.

Amine	**pK_a**[a]	**K_{Eq}**	**pK_a (DNT, calculated)**
benzylamine	10.2	$(4.79\pm0.46) \times 10^{-6}$	15.5
n-butylamine	11.1	$(9.73\pm0.56) \times 10^{-5}$	15.1
diethylamine	10.5	$(2.943\pm0.097) \times 10^{-5}$	15.0
triethylamine	9.0	$(3.75\pm0.47) \times 10^{-7}$	15.4
isopropylamine	Proton transfer slow. Equilibrium not achieved in 5 min.		
tert-butylamine	Proton transfer slow. Equilibrium not achieved in 5 min.		

[a] pK_a in DMSO from refs. 141,142.

The thus fitted values for the proton transfer equilibrium constants, K_{Eq}, for the different amines differ from one another by over two orders of magnitude (see Table 1) and reflect differences in the basicity of the amines in DMSO. This is illustrated by Figure 34, in which the logarithm of the thus determined K_{Eq}, is plotted versus the pK_a of these amines in DMSO, as they were reported in the literature.[141,142] As expected, there is a linear correlation ($r^2 = 0.969$) between the two parameters. Moreover, the pK_a of DNT as calculated from K_{Eq} and the previously published pK_a values of the amines (15.3±0.2; Table 1, right column) matches very closely the reported value for the pK_a of DNT (15.0) in a 1:1 H_2O:DMSO solution,[115] and is also consistent with DFT calculations discussed in the next section of this contribution.

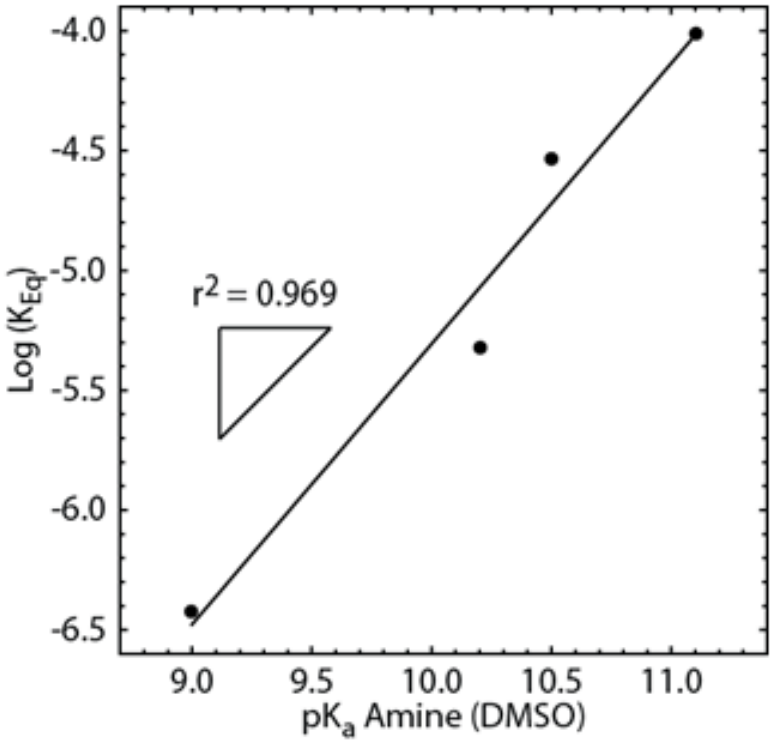

Figure 34: Log K_{Eq} vs. pK_a along with the linear best fit for the amines tested in this work. The slope indicator shows the expected slope of 1.

As mentioned above, NMR spectra of DNT in the presence of diethylamine showed only a slight broadening of the peaks associated with the phenyl hydrogens and no significant changes in chemical shifts. In view of these fits, this can be explained easily by the extremely low values for the proton transfer equilibrium constant. At equilibrium, only 0.1% of the DNT in a 50 mM DNT/50 mM diethylamine solution is deprotonated.

It is interesting to note that for isopropylamine and *tert*-butylamine, the deprotonation process is rather slow, presumably due to the sterically hindered accessibility of the nitrogen in these amines. While equilibrium for the other amines was achieved quickly enough to allow for the determination of an equilibrium constant, deprotonation of DNT by isopropylamine and *tert*-butylamine was so slow that equilibrium was not achieved within five minutes. At these long time scales, the absorption resulting from the

deprotonated DNT starts to decrease, and the solutions turn red within hours unless solutions are carefully purged with argon to remove traces of oxygen. Indeed, bubbling of oxygen into a blue solution that had kept its color for several hours after being purged with argon resulted in a color change to purple within 5 and red within 10 minutes. Since samples in which DNT determination is of interest always contain oxygen, further studies of the deprotonation of DNT by isopropylamine and *tert*-butylamine in an oxygen-free environment were not pursued.

Density Functional Theory Studies

In order to gain further insight into the surprising absence of Meisenheimer complex formation for DNT, we examined the energetics for association of DNT with ethylamine as a prototype primary amine. In particular, for various possible complex structures, we began by optimizing molecular structures at the M06-2X/6-31+G(d) level of DFT (see the Methods Section below for full theoretical details).

Initially, we attempted to locate Meisenheimer complexes in the gas phase by building reasonable starting geometries (with C–N bonds between appropriate aryl ring carbons and the amine nitrogen of roughly 1.45 Å) but such structures were not stable. Instead, they smoothly dissociated to van der Waals type complexes with the nitrogen lone pair clearly oriented towards some electrophilic center, but with distances only slightly less than the sum of the relevant van der Waals radii. Among the electrophilic centers were the nitrogen atoms of the nitro groups, the center of the aromatic ring, and positions axially above ring carbons at which Meisenheimer attack might be expected.

As the Meisenheimer complex of DNT and ethylamine has charge-separated character (formal resonance structures involve aci nitronates and ammonium cations), deprotonation of the NH_2 group by proton transfer to another ethylamine molecule appears plausible.[143,144] However, such a process would not result in a maximum in the Job's plot at a 1:1 mole ratio of DNT and the amine. Moreover, simple deprotonation is not possible in the case of Meisenheimer complexes of triethylamine because the nitrogen of the latter has no directly bound hydrogen. Therefore, we speculated that solvation

might provide an alternative mode of stabilization of the Meisenheimer geometries. Indeed, we successfully located a number of such geometries once the effects of DMSO solvation were included in the optimization process by the use of the SMD continuum solvation model.[145] However, the loose van der Waals complexes found from the gas-phase optimizations were also determined to be legitimate equilibrium structures in DMSO solution, i.e., they did not spontaneously collapse to Meisenheimer complexes. Figure 5 illustrates ten optimized structures, five of each class of complexes.

Although the Meisenheimer complexes are computed to be true equilibrium structures in DMSO solution, their free energies are predicted to be substantially higher than those of the looser van der Waals complexes. Figure 35 lists the computed microscopic binding free energies for the various complexes, taking the convention that a positive value implies that separated species are more stable than the complex (c.f. eq. 5), as calculated at the SMD(DMSO)/M06-2X/6-311+G(2df,2p)//SMD(DMSO)/M06-2X/6-31+G(d) level of theory and including thermal contributions.

We emphasize the term "microscopic" when referring to complex free energies, because each binding free energy listed is for a single geometry, but it is clear that these various geometries will all be readily interconverting with one another, and presumably with many, many others that we did not attempt to locate, since there are numerous different rotational possibilities associated with, for instance, the orientation of the ethyl group of the amine with respect to the ring substituents of DNT (some examples of such isomerism are included in Figure 35). In such a situation, the experimentally measured binding constant does *not* reflect the free energy of any one structure relative to separated DNT and ethylamine, but it instead reflects the relative free energy G of the entire equilibrium population of complexes, computed as[146]

$$G = -RT \ln \Sigma_i \exp(-G_i / RT) \qquad (5)$$

where the sum runs over all conformers i, G_i is the microscopic free energy of conformer i, and R and T are the universal gas constant and temperature, respectively.

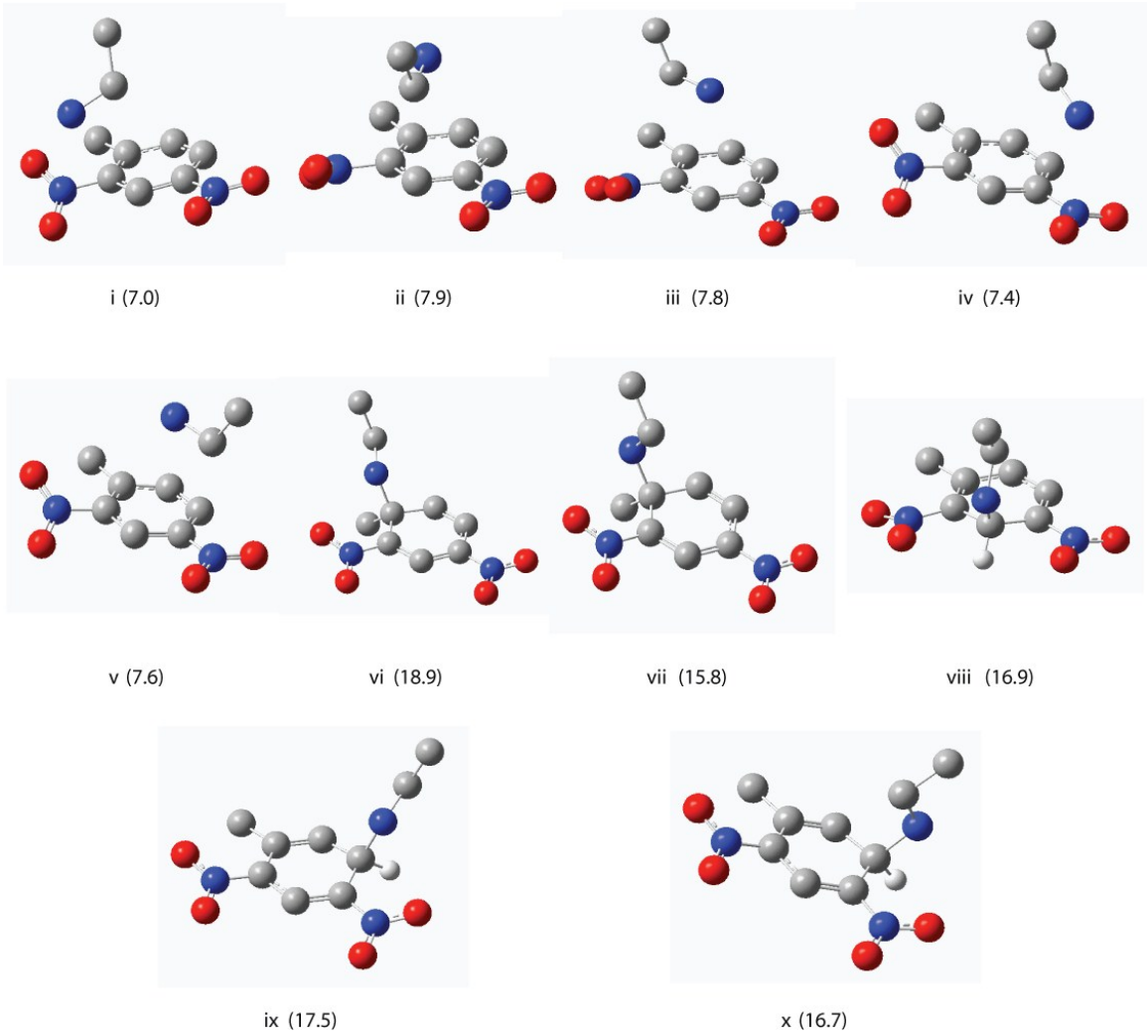

Figure 35: Optimized structures and binding free energies (kcal/mol) of ten different complexes of ethylamine with 2,4-dinitrotoluene relative to separated components and computed at the SMD(DMSO)/M06-2X/6-311+G(2df,2p)//SMD(DMSO)/M06-2X/6-31+G(d) level including thermal contributions. Structures i-v are loose van der Waals complexes and structures vi-x are Meisenheimer complexes. Hydrogen atoms are not shown for clarity, except at the position of Meisenheimer substitution in the lower two rows; hydrogen atoms are white, carbon atoms are gray, nitrogen atoms are blue, and oxygen atoms are red.

The substantial entropy associated with the very large number of possible complexes, only some of which are listed in Figure 35, will lower the population free energy significantly relative to the separated species. Moreover, it seems also likely that the first DMSO solvation shell may impart additional stability to the complexes by acting as a hydrogen bond acceptor to the amine protons that develop partial positive charge character in the bimolecular complexes. We have not attempted to model this point given the impracticality of surveying a large number of termolecular complexes at the quantum mechanical level.

We did examine the quantitative utility of the M06-2X density functional by comparing the gas-phase component of the complex interaction energies computed at the M06-2X level to values computed at the MP2/6-311+G(2df,2p) level of theory. The MP2 interaction energies were typically about 1 kcal/mol *more* favorable for the van der Waals complexes and 3 to 4 kcal/mol *less* favorable for the Meisenheimer complexes. As the density functional and correlated post-Hartree-Fock levels of theory are in reasonable agreement with one another, and as it is more difficult to achieve convergence with respect to the one particle basis set at the MP2 level,[146] we will take the M06-2X predictions to be reasonable, which is consistent with the documented strong performance of this functional in the prediction of non-bonded interactions.

Returning to the issue of the Meisenheimer complexes being substantially less stable than the looser van der Waals complexes, this observation is consistent with the NMR and UV-Vis spectral data noted above. Thus, we computed ^{1}H NMR chemical shifts for DNT and complexes **i**, **v**, and **viii** following the WP06 protocol[147] with DMSO solvation. Shifting the predicted absolute shieldings so that H-6 in DNT is predicted to have its experimental chemical shift, we computed values for H-3, H-5, H-6, and the averaged methyl signal in DNT of 9.15, 8.57, 7.66, and 2.62 ppm, respectively. The relatively poor prediction of the chemical shift for H-3 compared to experiment may reflect dynamical effects associated with the nitro groups that are not taken into account in the calculations,

but this point is not important for the following internal comparison. In the case of loose complexes **i** and **v**, the same proton chemical shifts are computed to be **i**: 9.07, 8.54, 7.53, and 2.61, and **v**: 9.15, 8.59, 7.63, and 2.62. The average deviation of these shifts from those for DNT itself is only 0.04 ppm. By contrast, the same proton chemical shifts predicted for the Meisenheimer complex **viii** are 6.65, 7.70, 5.41, and 2.42, respectively. Since all complexes in rapid equilibrium on the NMR time scale should contribute to the observed chemical shifts proportional to their equilibrium populations, it is clear that the amount of Meisenheimer complex(es) present at equilibrium must be *very* small in order to reconcile the experimental observation that there is no apparent change in the DNT chemical shifts upon addition of amine.

Returning to the question of the precise free energies of the Meisenheimer complexes relative to the looser van der Waals complexes, this is decidedly non-trivial to compute, although Figure 5 includes microscopic estimates. A complicating aspect is that the SMD model predicts the solvation free energies for these formally zwitterionic complexes to be from –19 to –27 kcal/mol, while for the loose van der Waals complexes values of –11 to –12 kcal/mol are computed. The potential errors are certainly on the order of one or two kcal/mol, not simply in the continuum model, but probably more importantly in the failure to account for specific DMSO solvation effects like accepting hydrogen bonds from the Meisenheimer complexes to further stabilize them.

Attempting to model more quantitatively (i) the solvent–complex interactions and (ii) the entropy associated with the phase space volume available to the many floppy complexes is well beyond the scope of this work. Nevertheless, the various computational results presented above support an interpretation of the experimental data that indicates complexes of the neutral amines and DNT (i.e., not conjugate acid/conjugate base pairs following deprotonation) to comprise a population of potentially very many loose van der Waals complexes of similar energy and also potentially many Meisenheimer complexes, but the latter are a very substantially smaller fraction of the population.

Finally, in addition to modeling Meisenheimer complexes to assess better their energetic accessibility, we also undertook DFT calculations to support our assignments of the pK_a of DNT and the ^{1}H NMR spectrum of its conjugate base. In particular, at the SMD(DMSO)/M06-2X/6-31+G(d) level of theory we computed the pK_a of DNT to be 14.5, which agrees with the measured value to within the typical uncertainty observed for computed pK_a values.[148] In addition, applying the same NMR protocol already outlined above, we predicted ^{1}H chemical shifts of 4.79 and 5.85 ppm for the exo-methylene protons of DNT conjugate base, and 6.38, 6.79, and 8.96 ppm for the aromatic protons. At this level of theory, the activation free energy for rotation of the exo-methylene (which would average its two ^{1}H signals) is predicted to be 41.5 kcal/mol, implying that no such rotation occurs on the time scale of the NMR experiment.. Compared to the experimental data in Section 2.2, the predicted values have a mean unsigned error of 0.2 ppm, which is again in good agreement and consistent with assigning the conjugate base as the source of the spectrum generated upon addition of hydroxide.

4.3 Conclusions

We have determined that 2,4-dinitrotoluene has, despite its two nitro groups, only a small tendency to form Meisenheimer complexes with hydroxide or basic amines in DMSO, contradicting assumptions previously made in the literature. Instead, deprotonated DNT was observed to exhibit intense absorption in the visible region, explaining the deep blue color of solutions of 2,4-dinitrotoluene and alkylamines.

Because of the wide interest in 2,4-dinitrotoluene due to environmental, toxicological and safety concerns, the implications of our findings go beyond the development of optical sensors. The relative ease of deprotonation combined with the comparatively low tendency to interact with nucleophiles, as evidenced by our results, suggests that results from a number of recent studies on other types of 2,4-dinitrotoluene sensors may have to be critically revisited. For example, sensors based on mesoporous SiO_2,[30] TiO_2 nanowires,[114] and nanoporous silicon films as well as carbon nanotubes and graphene

have been reported but the deprotonation of 2,4-dinitrotoluene on oxide surfaces or at the well-known oxygenated defects of carbon-based materials has not been considered. Similarly, electron donor–acceptor (EDA) complexes were suggested to cause adsorption of DNT to clay,[131] a more refined reinterpretation of which could have a substantial impact on our understanding of the kinetics of 2,4-dinitrotoluene transport through contaminated soils.[149] Finally, a reevaluation of the reactivity of 2,4-dinitrotoluene with special attention to deprotonation and the interaction of this nitroaromatic with nucleophiles may lead to a better understanding of the decomposition of this dinitroaromatic pollutant in the environment.

4.4 Methods

4.4.1 Experimental

All reagents were used as received without further purification unless noted otherwise. 5 M D_2SO_4 (≈90 atom % D) was prepared from appropriate volumes of H_2SO_4 and D_2O. All dilute solutions for UV-Vis experiments were prepared in reagent grade DMSO from Sigma-Aldrich (St. Louis, MO, USA). 2,4-Dinitrotoluene was obtained from Alfa-Aesar (Ward Hill, MA, USA). All amines were obtained from commercial suppliers. UV-Vis absorbance spectra were obtained using a Shimadzu UV160U spectrophotometer within five minutes of preparation of the sample, unless otherwise stated in the text. All ^{1}H NMR experiments were carried out on a Varian Inova 300 MHz spectrometer.

4.4.2 Computational

All geometries were fully optimized at the M06-2X level[150] of density functional theory[146] making use of the 6-31+G(d) basis set.[151] The effects of DMSO solvation were included in the geometry optimizations using the SMD solvation model.[145] Thermal contributions to free energy were computed at this level of theory following the usual

ideal-gas, rigid-rotator, harmonic-oscillator protocol.[146] Improved estimates of binding free energies were obtained by replacing the electronic energies computed at the M06-2X/6-31+G(d) level with single-point values computed at the M06-2X/6-311+G(2df,2p) level or at the MP2/6-311+G(2df,2p) level. ^{1}H NMR and UV-Vis calculations made use of the WP06 functional/basis set combination[147] and the INDO/S model,[152] respectively. The 1 M to 1 M standard-state free energy of solvation for H^{+} in DMSO, required for computation of the pK_a of DNT using standard techniques,[146,148,153] was taken as –273.3 kcal/mol, as recommended by Kelly et al.[154] All calculations made use of the *Gaussian* 09 Rev A.02 suite[155] of electronic structure programs.

4.5 Supplementary Material

4.5.1 Job's Plots and Resulting Fits For *n*-Butyl-, Diethyl-, and Triethylamine

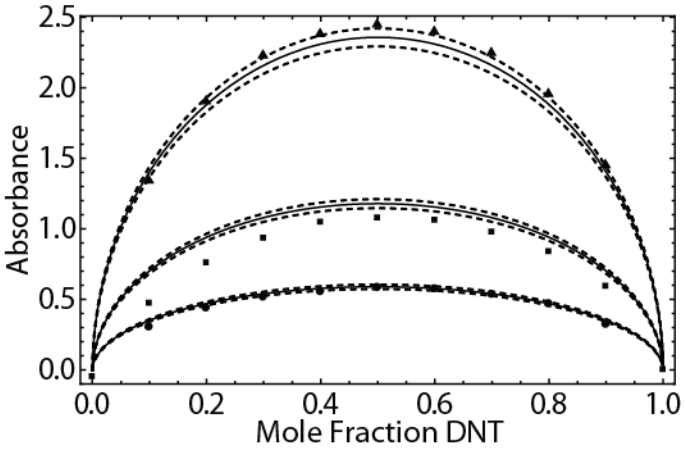

Figure 36: Job's plots and corresponding fits for the system of 2,4-dinitrotoluene (DNT) and *n*-butylamine (total concentration of DNT and *n*-butylamine for the data fitted with the bottom, middle, and top curve were 10, 20, and 40 mM, respectively). The solid curves indicate the best fit while the dashed curves indicate the 95% confidence intervals. T = 22 °C. Fitted parameter: $K_{Eq} = 9.73 \times 10^{-5}$.

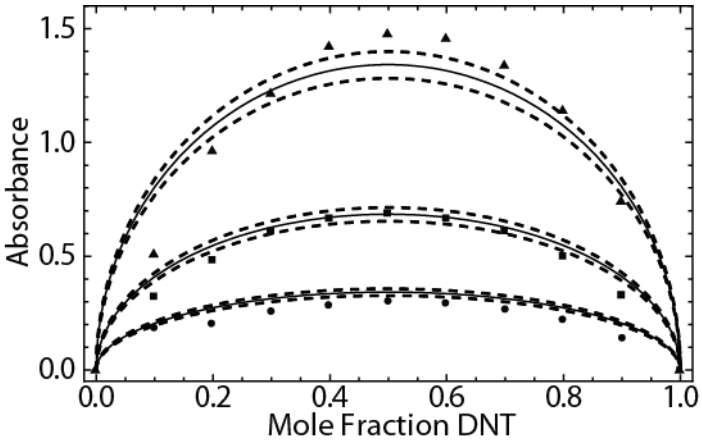

Figure 37: Job's plots and corresponding fits for the system of DNT and benzylamine (total concentration of DNT and benzylamine for the data fitted with the bottom, middle, and top curve were 25, 50, and 100 mM, respectively). The solid curves indicate the best

fit while the dashed curves indicate the 95% confidence intervals. T = 22 °C. Fitted parameter: $K_{Eq} = 4.79 \times 10^{-6}$.

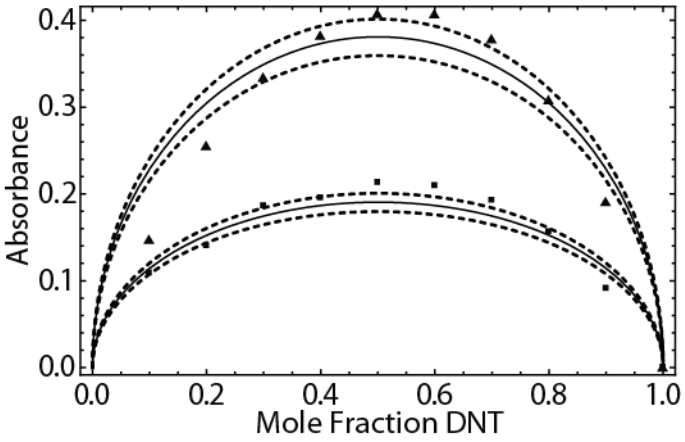

Figure 38: Job's plots and corresponding fits for the system of DNT and triethylamine (total concentration of DNT and triethylamine for the data fitted with the bottom and top curve were 50 and 100 mM, respectively). The solid curves indicate the best fit while the dashed curves indicate the 95% confidence intervals. T = 22 °C. Fitted parameter: $K_{Eq} = 3.75 \times 10^{-5}$.

5 CHAPTER FIVE

Getting More out of a Job Plot: Determination of Reactant to Product Stoichiometry in Cases of Displacement Reactions and *n:n* Complex Formation

In part from:

Olson, E. J.; Bühlmann, P. "Getting More out of a Job Plot: Determination of Reactant to Product Stoichiometry in Cases of Displacement Reactions and *n:n* Complex Formation" **2011**, 76, 8406-8412.

Adapted in part with permission from the Journal of Organic Chemistry, 2011, 76, 8406.

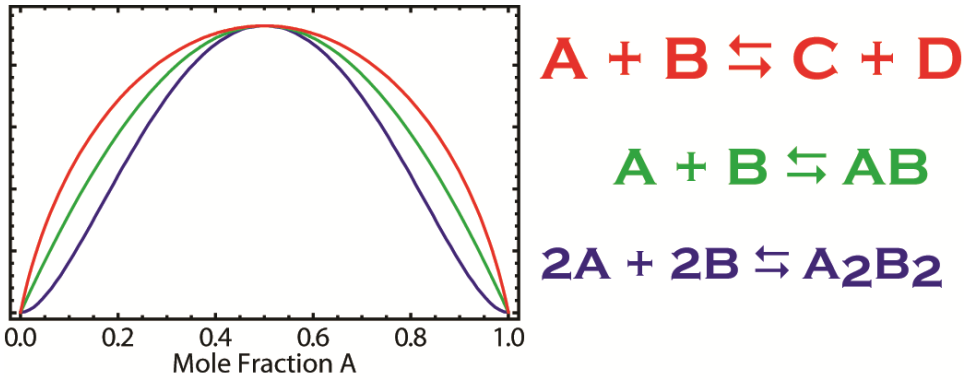

The Method of Continuous Variation (often referred to as Job's method) is an easy and common method for the determination of the reactant stoichiometry of chemical equilibria. The traditional interpretation of Job's plots has been limited to complex association equilibria of the type n A + m B $\rightleftharpoons$ A_nB_m while little focus has been placed upon displacement type reactions (e.g., A + B $\rightleftharpoons$ C + D), which can give Job's plots that look quite similar. We developed a novel method that allows the user to accurately distinguish between 1:1 complex association, 2:2 complex association, and displacement reactions using nothing more than a pocket calculator. This method involves preparing a Job's plot of the system under investigation (using regularly spaced mole fractions), normalizing the measured quantities (such as the concentration of A_nB_m or C for the above reactions) to their maximum value (i.e., at mole fraction 0.5), and determining the sum of the normalized values. This sum is then compared with theoretically predicted normalized sum values that depend on the nature of the equilibrium. The relationship between, on one hand, the sum of the normalized values and, on the other hand, the reaction equilibrium constant and the concentration of the stock solutions used for the preparation of the Job's plot is also explored. The use of this new technique for the interpretation of Job's plot permits users to readily determine information that can be obtained otherwise only with laborious additional experiments, as illustrated by the analysis of four Job's plots taken from the literature.

5.1 Introduction

Several techniques have been developed for the determination of the stoichiometry of chemical equilibrium reactions, including the Method of Continuous Variation,[135,156-158] Slope Ratio Method,[159] and Mole Ratio Method,[160] to name a few. Due to its simplicity, the Method of Continuous Variation (often referred to as Job's Method), first described by Ostromisslensky,[156] Dension,[157] and Job,[135] is widely regarded as the most popular of these methods.[4,161] A common use of Job's method is the determination of the ratio of the reaction coefficients *n* and *m* in an association equilibrium of the form

$$n\,\mathrm{A} + m\,\mathrm{B} \rightleftharpoons \mathrm{A_nB_m} \tag{1}$$

where A and B represent the free species at equilibrium (i.e., a ligand and a substrate), and A_nB_m represents a molecular complex of A and B.[4,135,137,162-165] In this method, the measured concentration of the complex A_nB_m (or a parameter that is proportional to its concentration, such as its UV/vis or infrared absorbance[166] or the integrated NMR signal intensity[167]) is plotted against the mole fraction of one reactant while the sum of the reactant concentrations, c^o_{SUM}, is kept constant. This plot is referred to as a Job's plot. It follows from equation 1 that $c^o_A = c_A + n\,c_{\mathrm{AnBm}}$ and $c^o_B = c_B + m\,c_{\mathrm{AnBm}}$, where c_A , c_B , and c_{AnBm} refer to the species present in solution, while c^o_{A} and c^o_{B} refer to the total concentrations of the reactants A and B, respectively. The latter are related to c^o_{SUM} at any given mole fraction *f* of species A by:

$$c^o_{\mathrm{A}} = f \times c^o_{\mathrm{SUM}} \tag{2}$$

$$c^o_{\mathrm{B}} = (1-f) \times c^o_{\mathrm{SUM}} \tag{3}$$

For association equilibria of this type, the highest concentration of the complex A_nB_n and, thereby, the maximum in the Job's plot are given by

$$x = \frac{n}{n+m} \tag{4}$$

where x is the mole fraction of A at the maximum point of the curve.[161] Clearly, this relationship makes Job's Method an extremely powerful tool to determine the

stoichiometries of equilibrium reactions, which is the cause for the popularity of Job's Method.

Because of its utility and simplicity, Job's Method has been utilized to interrogate a wide variety of systems, including ligand:metal complexes,[168] complexes of inorganic anions and organometallic compounds,[169,170] the binding of DNA to fluorescent dyes,[171] and the interaction of organic hosts and guests,[172,173] to name just a few. Because of the widespread use of Job's method, several reports highlighting the technical aspects of the method have been published.[128,136,137,139,140,165,166] In particular, a number of techniques have been developed to directly determine the formation constant of the complexes that are investigated by fitting of Job's plot curves.[137,139,163,165,168]

However, while the conventional interpretation of a Job's plot allows for the immediate determination of the empirical ratio of the reactants in a chemical equilibrium by the location of the maximum in the plot, distinguishing between 1:1, 2:2, and higher *n*:*n* stoichiometries on the basis of a Job's plot is more difficult because they all exhibit a maximum at the same mole fraction (i.e., $f = 0.5$). Recently, a method developed by Sayago and co-workers utilized Job's method with spectrophotometry to distinguish between n:m stoichiometries of the type 1:1 and 2:2.[162] While the use of this method accurately confirmed the presence of a weakly bound 2:2 complex, it relied upon the prediction of a maximum absorbance and replotting of the Job data in a linearized form derived from a method developed by Heller and Schwarzenbach.[174] Even more difficult is the differentiation between an association equilibrium as described by equation 1 and a displacement reaction of the type

$$A + B \rightleftharpoons C + D \qquad (5a)$$

where the concentration of either species C or D is detected and plotted as a function of the mole fraction of either A or B. The method described herein considerably simplifies this problem as it can be used to quickly and accurately determine the stoichiometry of chemical equilibria from Job's plots. Specifically, this contribution focuses on the three most common reaction types, which are 1:1 complex association (i.e, Equation 1 where

n = m = 1), 2:2 complex association (n = m = 2), and the 1:1 displacement reaction (Equation 5a). Note that any treatment of the latter also applies to the special case of

$$AB + C \rightleftharpoons A + BC \tag{5b}$$

where B is transferred from A to C. A typical example for such a reaction is a H^+ transfer. Examples of other reactions that involve two reactants and give a Job's plot with a maximum at the mole fraction of 0.5 seem to be very rare.

Distinguishing between the formation of complexes of the type A_nB_n and displacement reactions using the method introduced in this contribution is achieved by normalization and summation of the measured concentration of a product of the reaction in question. As with other methods for interpreting Job's plots, this method is limited to the presence of a single equilibrium.[4] To simplify the discussion herein, we refer to the species written on the left hand side of equilibria 1, 5a, and 5b as reactants while those written on the right hand side are referred to as products.

5.2 Description of Different Equilibria

5.2.1 1:1 Complex Association

In the case of 1:1 complex association, as described by Equation 1 for n = m = 1, the system is described by:

$$K = \frac{c_{AB}}{c_A \times c_B} \tag{6}$$

$$c_A^o = c_{AB} + c_A \tag{7}$$

$$c_B^o = c_{AB} + c_B \tag{8}$$

where K is the equilibrium constant describing the complex formation, and c_i is the equilibrium concentration of species i. Solving the set of Equations 2, 3, and 6–8 for c_{AB} in terms of c_{SUM}^o, f, and K results in:

$$c_{AB} = 1 + c_{SUM}^o K - \sqrt{1 + 2c_{SUM}^o K + [c_{SUM}^o K(1-2f)]^2} \tag{9}$$

5.2.2 2:2 Complex Association

For a 2:2 complex association, as described by Equation 1 for n = m = 2, the system is described as:

$$K = \frac{c_{A_2B_2}}{(c_A \times c_B)^2} \tag{10}$$

$$c_A^o = 2 \times c_{A_2B_2} + c_A \tag{11}$$

$$c_B^o = 2 \times c_{A_2B_2} + c_B \tag{12}$$

Unlike in the case of 1:1 complex association, combining Equations 2, 3, and 10–12 results in a (fourth order) polynomial that cannot be solved algebraically to give a single discrete equation describing the system.[170] As for any fourth order polynomial, there are four algebraic solutions to this problem, but the Job's plots cannot be calculated from one of these algebraic solutions alone. Instead, it depends on the actual numerical values of K, c_A^o, and c_B^o which algebraic solution has to be used to calculate the concentration of A_2B_2. Consequently, this system of equations was solved for the following discussion numerically, using as for all other graphs and calculations too the software Mathematica 7 (Wolfram Research, Champaign, IL).

5.2.3 1:1 Displacement Reaction

Last, for a 1:1 displacement reaction as described by Equation 5a, the equilibrium is described by:

$$K = \frac{c_C \times c_D}{c_A \times c_B} \tag{13}$$

$$c_A^o = c_A + c_C \tag{14}$$

$$c_B^o = c_B + c_C \tag{15}$$

$$c_C = c_D \tag{16}$$

Solving the set of Equations 2, 3, and 13–16 for c_C or c_D in terms of c^o_{SUM}, f, and K results in:

$$c_C = c_D = \frac{c^o_{SUM}K - c^o_{SUM}\sqrt{K^2(1-2f)^2 - 4Kf^2 + 4Kf}}{2(K-1)} \tag{17}$$

THEORETICAL PREDICTION OF JOB'S PLOTS

Figure 1 shows on the left hand side representative plots of the three systems described above for several equilibrium constants and a c^o_{SUM} value of 10 mM. For simplicity, the concentration of the measured species is plotted rather than a measurable parameter that is proportional to its concentration, such as absorbance or integrated NMR signal intensity. To facilitate the direct comparison of the curve shapes and to emphasize the difference between the three different systems, the same plots are also shown on the right hand side, but this time normalized to their maximum value, c_{MAX}. Because the type of equilibria described here have an equimolar reactant stoichiometry, c_{MAX} is the concentration of the measured species at $f = 0.5$. Therefore, the plotted variable c/c_{MAX} is the ratio of the concentration of the measured species at point f and the concentration of that species at $f = 0.5$. In other words, c/c_{MAX} is the concentration of the measured species normalized with respect to its concentration at $f = 0.5$.

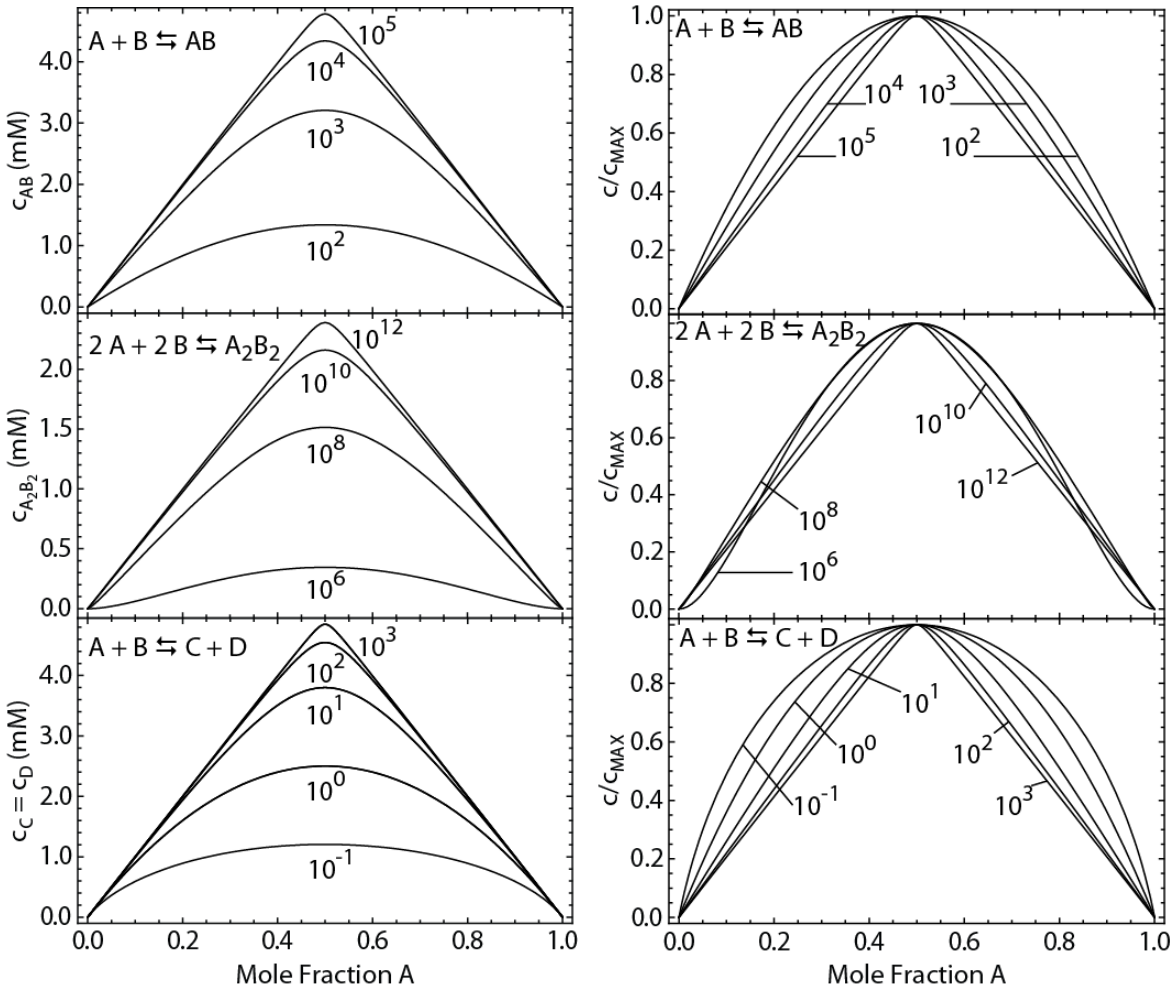

Figure 39: Theoretical (left) and normalized (right) Job's plots for 10 mM stock solutions (i.e., c^{o}_{SUM} = 10 mM) and several equilibrium constants for 1:1 association (top), 2:2 association (middle), and 1:1 displacement (bottom) equilibria as described by equation 5a. The different curves are labeled with their respective equilibrium constants, *K*.

As pointed out in the literature, the shape of the Job's plot curves shown in Figure 39 distinctly varies with the equilibrium constant.[136,161] For all three equilibrium stoichiometries described herein, the predicted curves approach a limiting triangular shape for reactions characterized by very large equilibrium constants, i.e., reactions

resulting in the formation of very stable associates or displacement reactions favoring very strongly the products C and D. Because this triangular shape is identical for all three systems, the determination of the stoichiometry from Job's method alone is not possible in these cases. Note, however, that use of a more dilute stock solution can eliminate this problem (see below).

It is also clear from the normalized plots that, for small equilibrium constants, the Job's plot curves for all three types of equilibria take on distinctly different shapes. As can be clearly observed in Figure 39, the integrated area under the normalized Job's plot differs greatly for the three equilibrium stoichiometries. These distinctly different shapes for the Job's allow for determination of the equilibrium stoichiometry plots for systems with small equilibrium constants. Indeed, previous methods to determine reaction stoichiometry and/or binding constant are applicable only for rather small equilibrium constants.[137,162,163,168,175]

5.2.4 Numerical Evaluation of Experimental Job's Plots

By quantitatively comparing the area under the normalized theoretical Job's plots, a method may be developed to determine the reaction stoichiometry. However, experimental Job's plots are not continuous functions of the mole fraction on the x-axis, making it impossible to determine the area from a discrete and limited number of measured data points without making some approximations. Indeed, experimental Job's plots are prepared using measured concentrations of reaction products only for a limited number of distinct mole fractions. Therefore, rather than calculating the area under an approximated continuous curve, it is much more convenient to consider the sum of the individual data points after normalization to $c_{MAX,,}$ as described in the previous section. Consequently, the method developed herein can be summarized as follows:

(1) Prepare a Job's plot as outlined in the literature,[161,166] varying the mole fraction of A (and consequently B) at constant intervals of Δf.

(2) Verify that the maximum of the resulting Job's plot curve is at $f = 0.5$, and that the curve is symmetric around $f = 0.5$. This is to confirm that the equilibrium under investigation involves the reaction of equal amounts of reactants A and B, and that the system being interrogated does not exhibit multiple equilibria. If the curve is either not centered at $f = 0.5$, or the curve is asymmetric, the approach developed herein is not applicable.

(3) Determine c/c_{MAX} value for each data point by dividing the measured quantity, c, (i.e., either the concentration of the product or a measured observable that is directly proportional to its concentration) at each point of f with the measured quantity at $f = 0.5$ (c_{MAX})

(4) Calculate the sum of c/c_{MAX} over the entire range of *mole fractions* from 0 to 1.

The calculated sum, as described by step (4), is directly related to the area under the continuous curve and will be represented in the following as $\Sigma\ c/c_{MAX}$. Therefore, the experimentally determined values of $\Sigma\ c/c_{MAX}$ can be used to determine the equilibrium stoichiometry by comparison to theoretically predicted values for $\Sigma\ c/c_{MAX}$.

Note that even if in step 3 a measured quantity other than concentration is used for c and c_{MAX}, special pretreatment of the data is not required provided that the measured quantity is directly proportional to the concentration of the reaction product. This is a direct result of the elimination of the proportionality constant between the measured quantity and the species concentration (e.g., molar absorptivity) using the normalization described in step 3.

5.3 Results and Discussion

5.3.1 Effect of Equilibrium Constant on $\Sigma\ c/c_{MAX}$

As mentioned above, the area under the Job's plot curve for any fixed c^{o}_{SUM} is highly dependent on the equilibrium constant, K. Because this area is directly related to $\Sigma\ c/c_{MAX}$, the value of $\Sigma\ c/c_{MAX}$ is also highly dependent upon the equilibrium constant.

The relationship between $\Sigma\ c/c_{MAX}$ and the equilibrium constant of the system is shown in Figure 40. For this plot, a mole fraction interval, Δf, of 0.1 was chosen.

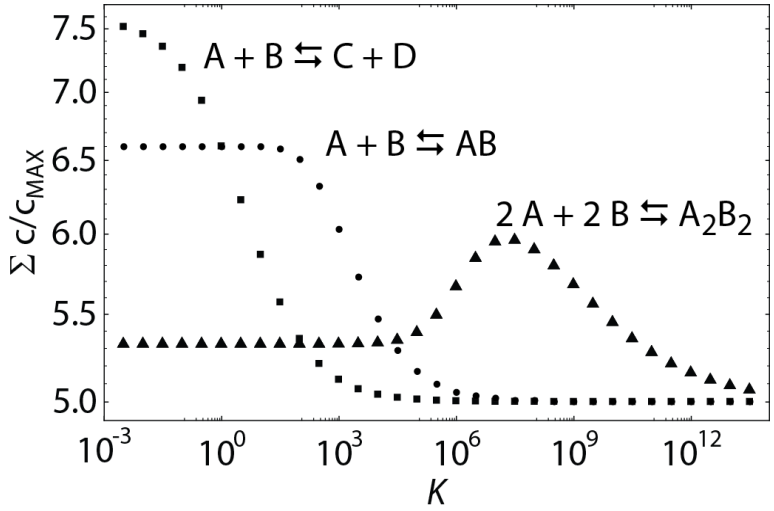

Figure 40: Plot of $\Sigma\ c/c_{MAX}$ versus K for 1:1 displacement (squares), 1:1 association (circles), and 2:2 association (diamonds) equilibria for 10 mM stock solutions and $\Delta f = 0.1$ (i.e., for Job's plots with 11 data points equally distributed on the mole fraction axis).

The curves for $\Sigma\ c/c_{MAX}$ versus K shown in Figure 40 illustrate two important features. First, for very large equilibrium constants, the value of $\Sigma\ c/c_{MAX}$ reaches a constant value. For the example of $\Delta f = 0.1$ used for Figure 40, this value is 5. This phenomenon is expected since, in the limit of large equilibrium constants, the Job's plots approach an isosceles triangle, i.e., a triangle with two equal sides (as shown in Figure 39). More importantly, in the limit of extremely large formation constants, $\Sigma\ c/c_{MAX}$ approaches a numerical value that is the same regardless of stoichiometry. This value only depends on the number of experimental points in the Job's plot, i.e., the number of mole fractions for which a measurement was performed. In the general case of n data

points distributed equally between 0 and 1 on the mole fraction scale, the limiting value of $\Sigma\ c/c_{MAX}$ is $(n\text{-}1)/2$ for all three types of reactions in question.

Second, in the limit of *small* equilibrium constants, a constant value of $\Sigma\ c/c_{MAX}$ is also achieved, but the value of $\Sigma\ c/c_{MAX}$ depends on the type of reaction. Thus, calculating $\Sigma\ c/c_{MAX}$ for systems in which the lower limit is reached allows for the direct determination of the type of equilibrium by comparison with the theoretically predicted values of $\Sigma\ c/c_{MAX}$ for the three different equilibria. Table 2 contains an abridged list of the numerical values for $\Sigma\ c/c_{MAX}$ for the three systems in the limit of small equilibrium constants. A more extensive list may be found in the Supplementary Information for this article.

Table 2: Theoretical values of $\Sigma\ c/c_{MAX}$ in the limit of small equilibrium constants as a function of the number of data points, *n*, of the Job's plot.

Number of Data Points[a]	Δf	$\Sigma\ c/c_{MAX}$		
		1:1 Association	1:1 Displacement	2:2 Association
9	0.1250	5.25	5.96	4.27
11	0.1000	6.60	7.55	5.34
16	0.0667	9.96	11.49	8.00
21	0.0500	13.30	15.41	10.67
26	0.0400	16.64	19.33	13.33
41	0.0250	26.65	31.04	21.34

a. Including $f = 0$ and $f = 1$.

As the value of $\Sigma\ c/c_{MAX}$ in the limiting case of *large* equilibrium constants, the values of $\Sigma\ c/c_{MAX}$ in the limiting case of *small* equilibrium constants can also be readily predicted from the number of data points, *n*, of the Job's plot. As plots of $\Sigma\ c/c_{MAX}$ values versus *n* show (see Table 2 and the corresponding table in the Supporting Information),

$\Sigma\ c/c_{MAX}$ in the limiting case of small equilibrium constants can be the calculated as $0.77\times(n-1)$ for the displacement reaction, as $0.66 \times (n-1)$ for the formation of the product AB, and as $0.53 \times (n-1)$ for the formation of A_2B_2. These relationships are empirical, but predict for all Job's plots with at least 9 data points the $\Sigma\ c/c_{MAX}$ values with an error of less than 1.0%. The few exceptions with errors in the 1.0 to 3.4% error range are all for Job's plots characterizing displacement equilibria investigated with 13 or less data points, where $\Sigma\ c/c_{MAX}$ is a slightly less accurate estimate of the area under the Job's plot curve.

Interestingly, the maximum in the curve for A_2B_2 in Figure 40 is always observed at $0.60 \times (n-1)$, which shows that, except for very minor deviations for very small values of *n,* the shapes of the curves depicted in Figure 40 do not depend on the number of data points. Figures that are equivalent to Figure 40, but that are prepared for different numbers of data points (*n*) in the Job's plots, differ from Figure 40 only by a scaling factor for the y-axis.

It is also clear from Figure 40 that experimentally determined, intermediate values of $\Sigma\ c/c_{MAX}$ immediately exclude the occurrence of certain equilibrium stoichiometries. For instance, if a Job's plot has been prepared for $\Delta f = 0.1$ and passes the symmetry test, and $\Sigma\ c/c_{MAX}$ lies between 6.60 and 7.55, formation of AB or A_2B_2 can be excluded. Consequently, there is strong evidence for a displacement reaction. Similarly, if for $\Delta f = 0.1$ the experimentally determined value of $\Sigma\ c/c_{MAX}$ lies above 6.00, the possibility of 2:2 association may be eliminated. Also, if for a Job's plot with $\Delta f = 0.1$ a value of 5.34 for $\Sigma\ c/c_{MAX}$ is calculated, and the Job's plot exhibits inflections near the mole fractions of 0 and 1 (giving it the characteristic bell shape shown in Figure 39), this is consistent with A_2B_2 formation. Consequently, AB formation and displacement can be excluded. In the event that the system being interrogated cannot be determined using one of these checks, it can be concluded that either the limit of weak binding for an A_nB_n formation is not reached, or that a displacement reaction is occurring. In such a case,

more information may be attained by varying the value of c^o_{SUM} used to determine the Job's plot.

Note that the $\Sigma\ c/c_{MAX}$ values for the displacement and the 2:2 association case are 17% larger and 20% smaller, respectively, than in the case of 1:1 stoichiometry. These are large differences and will typically permit a distinction between different types of equilibria within experimental error even where a casual look at the Job's plots might suggest that the differences between the Job's plots for the different types of equilibria are not very pronounced.

5.3.2 Effect of Stock Concentration on $\Sigma\ c/c_{MAX}$

Figure 40 may appear somewhat discouraging if *K* lies outside the lower limiting range. However, the use of a stock solution of lower concentration can often easily shift the Job's plot towards the low binding limit. In other words, for the purpose of the method of Job's plot analysis presented here, a binding constant is only large or small in comparison to the c^o_{SUM} employed. Dilution of the stock solution to shift the Job's plot towards the low binding limit is limited only by the lower detection limit of the instrumental method used to measure the concentration of the observed species (e.g., UV/vis, infrared or NMR spectrometry).

Figure 41 shows the relationship between $\Sigma\ c/c_{MAX}$ and c^o_{SUM} for 1:1 and 2:2 association systems. The 1:1 displacement reaction has been omitted from this plot, as it can be shown easily from Equation 17 that for this system $\Sigma\ c/c_{MAX}$ is independent of c^o_{SUM}.

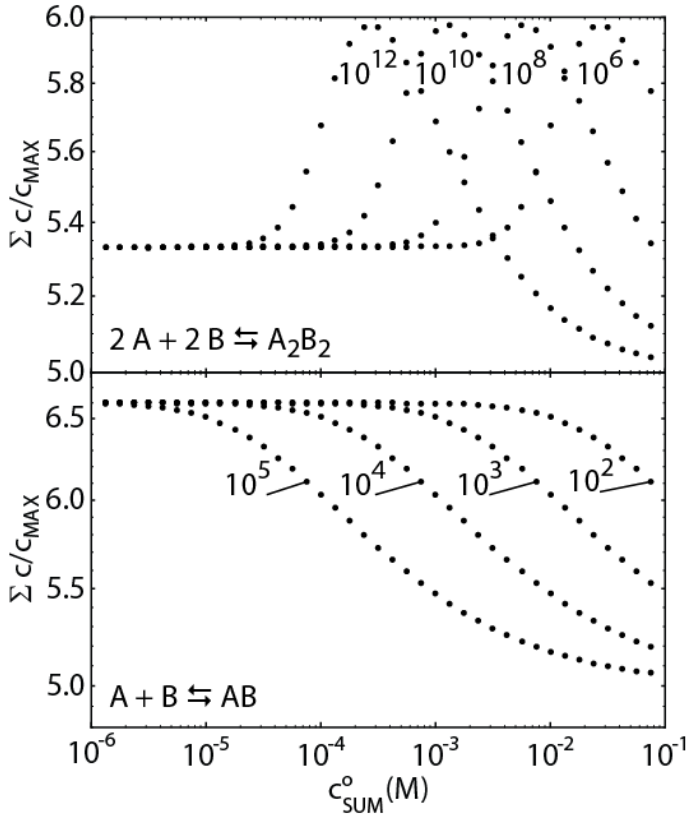

Figure 41: Relationship of Σ c/c_{MAX} on c^o_{SUM} for $\Delta f = 0.1$ and several formation constants for the 1:1 and 2:2 association reactions. All curves are labeled with the respective formation constant.

As it can be seen from Figure 41, Σ c/c_{MAX} exhibits a strong dependence upon the c^o_{SUM} chosen when preparing the Job's plot. As such, the limiting value of Σ c/c_{MAX} observed for small equilibrium constants may be determined experimentally by varying the c^o_{SUM} chosen for the Job's plot, thus allowing the determination of the reaction stoichiometry over a wide range of equilibrium constants.

While in an intermediate case the most obvious option for the determination of the correct type of equilibrium is to lower c^o_{SUM} to a value sufficiently low such that Σ c/c_{MAX} reaches its limiting value, it is not the only option. Even in the case of an experimental technique that has a detection limit that is insufficiently low to permit working with c^o_{SUM}

low enough to reach the lower limiting case, there are still prospects to determine the type of equilibrium from Job's plots. If the measured $\Sigma\ c/c_{MAX}$ is intermediate to the limiting values determined above and shows no dependence on c^o_{SUM}, the reaction may immediately be concluded to be a 1:1 displacement reaction. Alternatively, if $\Sigma\ c/c_{MAX}$ shows a positive slope with respect to c^o_{SUM}, the equilibrium is a 2:2 association reaction.

5.3.3 Application to Published Data

To demonstrate the utility of the method described in this article, four Job's plots published previously[170,173,176,177] were analyzed, and the conclusions gained by this new method of Job's plot analysis were compared with the conclusions reported in the original literature. The plots were chosen as examples for all types of equilibria discussed in this paper. A summary of these results is shown in Table 3 and is discussed in the following.

Table 3: Analysis of Job's Plots from references 170, 173, 176, and 177.

Reference	Figure[a]	Published Reaction Type[b]	$\Sigma\ c/c_{MAX}$	% Error[c]
170	2	2:2 association	5.49	2.72
173	11	1:1 association	6.55	–0.83
176	2	Proton transfer	7.54[d]	–0.17
177	4	1:1 association	7.26[e]	10.0

[a] Figure number in original publication.
[b] Published conclusion.
[c] Percent error in measured $\Sigma\ c/c_{MAX}$ versus theoretical Job's plot curve for the reaction type indicated.
[d] Average result from four Job's plots.
[e] The data point at 100% host was omitted from this reanalysis.

Using the analysis method introduced in this paper, two examples of association reactions from the literature were analyzed and the original authors' conclusions confirmed. First, a Job's plot describing the complexation of iron(III) with chrome azurol S, a known 2:2 association reaction, was reanalyzed.[170] As expected, reanalysis of the Job's plot presented in the original article indicates that, with an error of only 3%, this system is a 2:2 association reaction. Another association system that we reanalyzed is the complexation of citrate by a fluorescent tricationic guanidiniocarbonyl pyrrole.[173] By monitoring the decrease in the fluorescence of this receptor upon addition of citrate, the authors nicely showed a 1:1 receptor:citrate stoichiometry and confirmed complex association by ^{1}H NMR spectroscopy. This conclusion is strongly supported by reanalysis using the method described above, the error being only –0.83%.

While distinguishing between 1:1 and 2:2 association reactions may be achieved using established analysis techniques, 1:1 displacement reactions are not as readily identified and can be quite easy to miss. This is particularly the case when the species observed for the Job's plot is the minority species, as we reported in a recent publication.[176] In this article, we characterized the interaction of 2,4-dinitrotoluene (DNT) with nucleophilic bases in DMSO. It has long been assumed that polynitroaromatic compounds such as DNT form colored Meisenheimer complexes with nucleophiles,[115-118,121,123] and the addition of an aliphatic amine to a solution of DNT in DMSO indeed produces an intense blue color. However, the presence of a Meisenheimer complex could not be confirmed by NMR spectroscopy. This led us to utilize a variety of techniques to investigate this system, leading to the conclusion that the interaction between DNT with a base in DMSO results in the deprotonation of an extremely small fraction of the DNT and not the formation of a Meisenheimer complex. As expected, reanalysis of Job's plots for the interaction of DNT with diethylamine shows very clearly that this interaction is a 1:1 displacement reaction, with an error of only –0.17% (Table 3, third row).

Another common system in which there can be difficulty in distinguishing between 1:1 association and 1:1 displacement is the case of hydrogen-bonding receptors for basic anions.[178] Such receptors often use guanidinium, amide, or urea functional groups (or their thio derivatives) as hydrogen bond donors to bind the anion of interest.[173,178] To enhance the hydrogen bond donor strength of these groups by increasing the partial positive charge on their hydrogens, these receptors are often substituted with electron withdrawing groups that also make these receptors more acidic. This leads to the possibility of deprotonation rather than complex formation.[179,180] As shown previously in the literature, the straightforward identification of deprotonation in such systems is somewhat complicated because the titration plot of a deprotonation reaction can be satisfactorily fitted using a 1:1 association model,[178] which can easily lead to erroneous conclusions. Therefore, one has to be careful and may have to rely upon a second, complementary technique to identify the occurrence of deprotonation. As an example, Table 3 includes the reanalysis of the interaction between the diamide receptor **1** and acetate, which has been previously interpreted as a 1:1 complex association (fourth row of Table 3).[177] Our reanalysis of the published Job's plot shows that this interpretation exhibits a 10.0% divergence between the theoretically expected value of $\Sigma\ c/c_{MAX}$ and the value determined from the experimental data. This is a large deviation considering that, in the limit of small equilibrium constants, erroneously fitting a perfect 1:1 displacement reaction with a 1:1 complexation model would result in a difference in $\Sigma\ c/c_{MAX}$ of only 14.4% (see Table 2 for 11 data points).

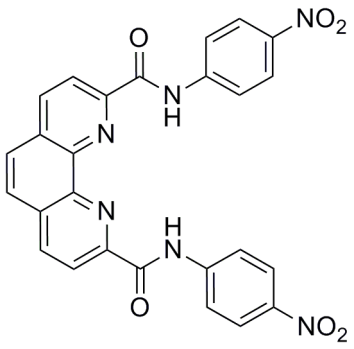

1

Indeed, this system can be fitted much more accurately based on a 1:1 displacement reaction, giving a deviation of only –3.8% from the theoretically expected value. The visual difference between the two fits is striking. When the experimental data is normalized to c_{MAX} and plotted along with the theoretically expected plots for 1:1 association and the displacement reaction (see Figure 42), the 1:1 association fit clearly show that the 1:1 association gives the much worse fit. The systematically positive residuals for this fit are a characteristic feature of an inappropriate model. Clearly, a reevaluation of the reaction of acetate with receptor **1** is warranted.

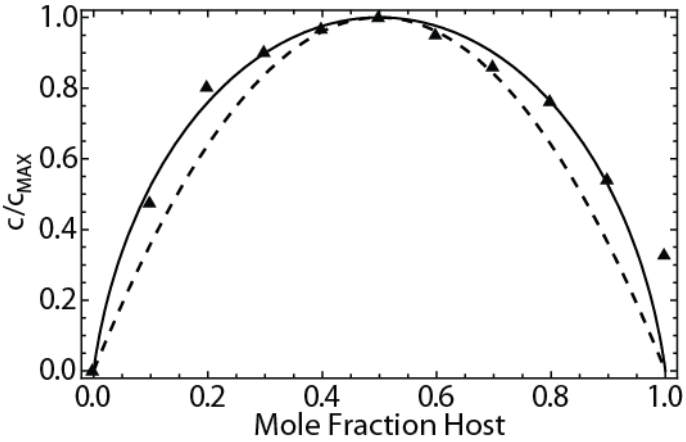

Figure 42: Reproduction of Figure 4 from Reference [177] normalized to the maximum at *f* = 0.5, along with theoretically expected Job's plots for 1:1 displacement (solid line) and 1:1 association (dashed line) in the limiting case of small equilibrium constants.

5.4 Conclusions

Job's Method is a powerful tool for the determination of the stoichiometry of the reactants in a chemical equilibrium. However, previously developed methods for interpreting Job's plots have been limited to complex association reactions.[4] Only recently, a method was developed by Sayago and co-workers to accurately discern between 1:1 and 2:2 association reactions.[162] This approach required linearization of the data, followed by least squares analysis of a linear fit of the data.

The new technique described in this paper allows rapid determination of the reactant:product stoichiometry of chemical equilibria with equimolar reactant stoichiometry by simple normalization and summation of equally spaced data points in a Job's plot. We have shown that the resulting $\Sigma\ c/c_{MAX}$ reaches upper and lower limiting values, the lower limiting value being distinct for the different reaction stoichiometries. Careful selection of the stock concentrations allows the user to access these regions for the case of 1:1 and 2:2 association reactions, while $\Sigma\ c/c_{MAX}$ is shown to be independent of c^o_{SUM} for 1:1 displacement reactions. This independence is an extremely useful diagnostic when intermediate values of $\Sigma\ c/c_{MAX}$ are observed for the system being studied.

The method proposed here is not intended to replace numerical fits of Job's plots entirely. The latter can still be very useful to determine equilibrium constants. However, fitting of Job's plots with several types of reaction models to determine which equilibrium model fits the data best is a very time-consuming process, especially if multiple Job's plots are fitted simultaneously and/or if Job's plots and titration curves are fitted simultaneously with one set of parameters (for an example, see ref. [176]). Moreover, Job's plot fitting is even more complicated when the extinction coefficient of the reaction product (or alternatively any other proportionality constant between the measured quantity on the reaction product) cannot be determined readily.[176] Under such circumstances, the remarkably simple method introduced here considerably simplifies the study of the equilibrium and the ultimate determination of equilibrium constants. We

tested this method by reanalyzing Job's plots that were previously presented in the literature, demonstrating the simplicity and utility of the method not only to confirm known complex stoichiometries but also to readily detect errors in the interpretation of systems investigated less thoroughly in the past. Given the regular use of Job's plots across different fields of chemistry and in related disciplines, this new method of analysis should prove a tool useful in studies of a wide range of chemical equilibria.

Table 4: Theoretical values of $\Sigma\ c/c_{MAX}$ based upon the number of data points, *n*, acquired.

Number of Data Points[a]	Δf	$\Sigma\ c/c_{MAX}$		
		1:1 Association	1:1 Displacement	2:2 Association
7	0.1667	3.89	4.34	3.20
8	0.1423	4.57	5.16	3.73
9	0.1250	5.25	5.96	4.27
10	0.1111	5.93	6.76	4.80
11	0.1000	6.60	7.55	5.34
12	0.0909	7.27	8.34	5.86
13	0.0833	7.94	9.13	6.39
14	0.0769	8.62	9.92	6.93
15	0.0714	9.29	10.70	7.47
16	0.0667	9.96	11.49	8.00
17	0.0625	10.62	12.28	8.53
18	0.0588	11.29	13.06	9.06
19	0.0556	11.96	13.85	9.60
20	0.0526	12.63	14.63	10.13
21	0.0500	13.30	15.41	10.67
22	0.0476	13.97	16.20	11.20
23	0.0455	14.64	16.98	11.73
24	0.0435	15.30	17.76	12.27
25	0.0417	15.97	18.55	12.79
26	0.0400	16.64	19.33	13.33
27	0.0385	17.31	20.11	13.87
28	0.0370	17.98	20.89	14.40
29	0.0357	18.64	21.67	14.93
30	0.0345	19.31	22.45	15.47
31	0.0333	19.98	23.24	16.00
32	0.0323	20.65	24.02	16.53
33	0.0313	21.31	24.80	17.06
34	0.0303	21.98	25.58	17.59
35	0.0294	22.65	26.36	18.13
36	0.0286	23.31	27.14	18.67
37	0.0278	23.98	27.92	19.19
38	0.0270	24.65	28.70	19.72
39	0.0263	25.32	29.48	20.27
40	0.0256	25.98	30.26	20.79

a. Including $f = 0$ and $f = 1$.

6 CHAPTER SIX

Electrochemical Characterization of 2,4-Dinitrotoluene in Aprotic and Protic Media

The widespread use of 2,4,6-trinitrotoluene (TNT) in explosive devices defines a great need for sensing devices for TNT and the byproducts of its manufacture. As an intermediate in commercial TNT production, 2,4-dinitrotoluene (DNT) is one of the most prevalent impurities in TNT. Moreover, the waste liquids from TNT manufacture contain a significant concentration of DNT. Because of their electroactive nitro groups, electrochemical detection is a promising route for construction of sensing devices of such compounds. In this work, the electrochemical reduction mechanism of DNT is investigated by cyclic voltammetry. In anhydrous solvents, DNT is shown to exhibit two well resolved one electron transfers. The radical anion formed by the reduction of DNT is shown to be sufficiently basic to deprotonate the weakly acidic methyl group of still unreacted DNT Moreover, we also show that in the presence of a pH buffer in acetonitrile, DNT is readily reduced to 2,4-bis(*N*-hydroxylamino)toluene in an irreversible eight proton, eight-electron transfer. This occurs at a substantially less negative potential than in the absence of protons. This indicates that the reduction of DNT in the presence of a source of protons is directly coupled to the protonation of DNT. The enhancement in signal observed for DNT in the presence of a proton source indicates that the incorporation of a proton source to electrochemical sensing setups will greatly enhance the sensitivity of DNT analysis.

6.1 Introduction

The detection of nitroaromatic explosives, such as the widely used 2,4,6-trinitrotoluene (TNT), is a subject of much research in view of both the detection of explosive devices and environmental remediation.[5,6,8,13,15,16,18,24,25,112,113,131,181,182] Due to the extremely low equilibrium vapor pressure of TNT, many detection efforts focus on the more readily vaporizing 2,4-dinitrotoluene (DNT).[6,112,113] Because the latter results in TNT production as a byproduct due to incomplete nitrification of toluene, DNT is nearly always present in TNT-based explosives.[182,183] Detection of DNT in aqueous samples is of additional importance because of its hepatocarcinogenicity.[111] The electroactive nature of the nitro substituents allow for the electrochemical detection of DNT.[28] Several explosive sensing devices have been presented in recent literature that rely upon electrochemical detection.[18,22-25,29,184] Despite the rather large amount of published work that takes advantage of the electroactivity of DNT, a surprisingly small amount of literature focuses on elucidating the mechanism for DNT reduction.

The polarographic characteristics of DNT in aqueous solution were shown to be rather similar to those of nitrobenzene in that each nitro group is reduced to an *N*-hydroxylamino group in a single four-proton, four-electron reduction wave.[28,185] This observation indicates that the cyclic voltammetry of DNT should also be very similar to that of nitrobenzene, thus providing a good starting point for proposing a mechanism for DNT reduction. Fortunately, the electrochemistry of nitrobenzene has been studied quite extensively.[28,186-190] In anhydrous acetonitrile and *N,N*-dimethylformamide, nitrobenzene is reduced electrochemically to produce a stable radical anion.[188,189] When liquid anhydrous ammonia is used as a solvent, the radical anion also accepts a second electron at a much more negative potential, producing a stable dianion.[186] In the case of 1,4-dinitrobenzene, two individual one-electron transfers are observed; however, it is unclear whether the radical nitrogen is again reduced or a diradical is formed.[191,192] In analogy to this work on related compounds, the following mechanism for the reduction of DNT is proposed here for aprotic media:

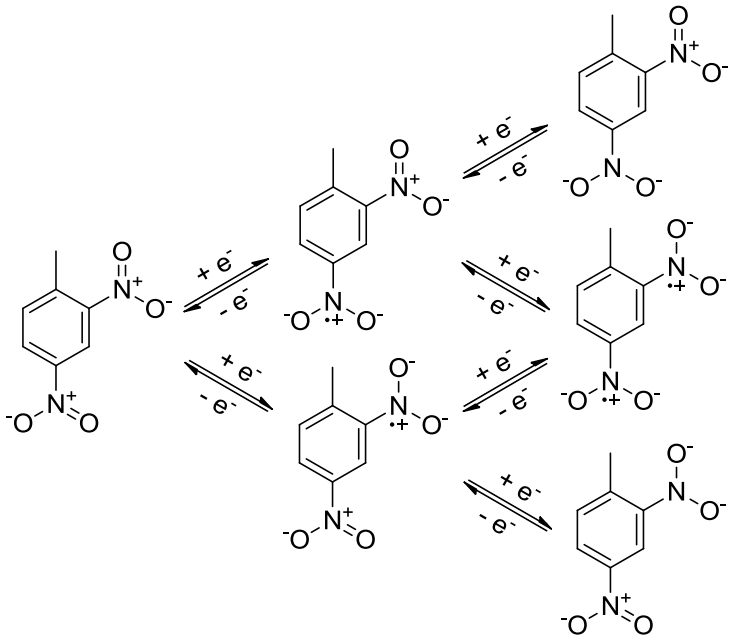

Figure 43: Proposed mechanism of DNT reduction in aprotic solutions.

This work shows that the reduction of DNT observed by cyclic voltammetry in acetonitrile undergoes a significant change upon the addition of a proton source. Analogously, previously published work showed that the polarographic reduction of nitrobenzene to a radical anion in anhydrous *N,N*-dimethylformamide decreases in intensity while a new reduction wave occurs that is attributed to the four step, four-electron production of *N*-phenylhydroxylamine upon the addition of a proton source.[188] In aqueous media, the reduction of nitrobenzene proceeds directly to the formation of *N*-phenylhydroxylamine.[186,187] In acidic solutions, *N*-phenylhydroxylamine then undergoes an additional two-proton, two-electron transfer at more negative potential that results in cleavage of the N–O bond to produce aniline.[186] Very recently, a computational study investigated the electrochemical mechanism and potentials of TNT reduction in aqueous solution, taking reference to the literature of experimental electrochemistry of various nitroaromatic compounds.[193] While the authors show that the nitro group in the 2 position of TNT is most easily reduced, it is not immediately clear whether this will also be true

for DNT. Thus, the mechanism presented in Figure 44 is proposed for the electrochemical reduction of DNT in proton-containing media.

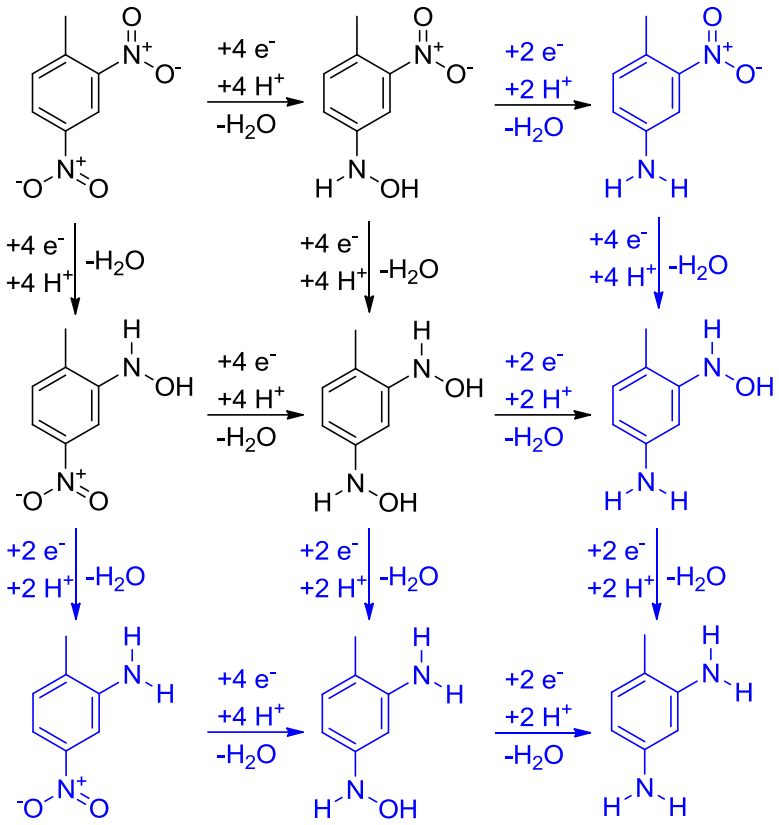

Figure 44: Possible reduction pathways to electrochemically produce 2,4-diaminotoluene from DNT in solutions with available protons.

For electrochemical reductions such as those depicted in Figure 43 and 44, it is important to note that all chemically reasonable routes to achieve the final product are likely followed simultaneously as competing processes. The total contribution of each path is dependent upon the pH of the solution along with the molecular properties of each intermediate.

In this work, we explore the electrochemical reduction mechanism of DNT in unbuffered acetonitrile and pH buffered acetonitrile. We show that DNT undergoes two well-resolved electron transfers in unbuffered acetonitrile as well as basic acetonitrile.

The radical anion formed in these solutions by the reduction of DNT is sufficiently basic to deprotonate the slightly acidic DNT, giving rise to the intense blue color indicative of deprotonated DNT.[176] In acetonitrile solutions buffered with a triethylamine/triethylammonium buffer, the two reduction waves coalesce into one irreversible reduction that is consistent with the production of 2,4-bis(*N*-hydroxylamino)toluene.

6.2 Experimental

Caution: Extreme care must be taken with organic solutions of tetrabutylammonium perchlorate and perchloric acid as these solutions may explode when heated or evaporated to dryness. All reagents were used as received without further purification unless otherwise noted. Anhydrous acetonitrile, electrochemical grade tetrabutylammonium perchlorate (NBu_4ClO_4), and 2,4-dinitrotoluene (97%) were obtained from Sigma-Aldrich (St. Louis, MO). pH-buffered acetonitrile solutions were prepared by adding appropriate amounts of reagent grade 70% $HClO_4$ from Fisher Scientific (Pittsburgh, PA) to a solution of 100 mM triethylamine (Sigma-Aldrich) in anhydrous acetonitrile/100 mM NBu_4ClO_4. All aqueous solutions were prepared with water that was previously deionized and charcoal-treated (≥18.2 MΩ cm specific resistance) with a Milli-Q PLUS reagent-grade water system (Millipore, Bedford, MA). The aqueous phosphate buffer components were of highest commercial purity and obtained from Sigma-Aldrich. Cyclic voltammetry experiments with acetonitrile were carried out with a CHI600C Potentiostat (CH Instruments, Austin, TX) while aqueous voltammetry experiments were performed with a Cypress Systems 1090 Potentiostat (Cypress Systems, Lawrence, KS). All electrochemical experiments were carried out using a three-electrode setup with a 1.6 mm-diameter Au disk (BAS, West Lafayette, IN) working electrode, a 0.25 mm Pt wire coil (99.998 %, Alfa Aesar, Ward Hill, MA) auxiliary electrode, and either a Ag/AgCl/saturated KCl reference electrode (BAS) for aqueous experiments or a Ag/(10 mM $AgNO_3$ + 100 mM NBu_4ClO_4) reference electrode

(BAS) for acetonitrile experiments. The Au working electrode was polished on Microcloth polishing pads using 5.0 μm Micropolish II deagglomerated alumina, both from Buehler (Lake Bluff, IL). After polishing, the electrode was rinsed thoroughly with deionized water and then ethanol, followed by drying under a stream of Ar. Prior to measurements, all voltammetry solutions were purged with UHP argon for 15 minutes while stirring vigorously to remove oxygen. UV–Vis spectra were measured with an Agilent 8453 UV–Vis spectrometer. All potentials referenced herein are with respect to Ag/Ag^+ for acetonitrile solutions and Ag/AgCl for aqueous solutions.

6.3 Results and discussion

6.3.1 Voltammetry with unbuffered acetonitrile

To determine whether, in the absence of a proton source, DNT would produce cyclic voltammograms (CVs) consistent with the two-step, two-electron transfer depicted in Figure 1, cyclic voltammetry of DNT was performed in unbuffered anhydrous acetonitrile. Typical CVs for DNT in acetonitrile/0.1 M NBu_4ClO_4 such as those shown in Figure 3 exhibit two redox couples centered at –1.30 and –1.68 V vs. Ag/Ag^+.

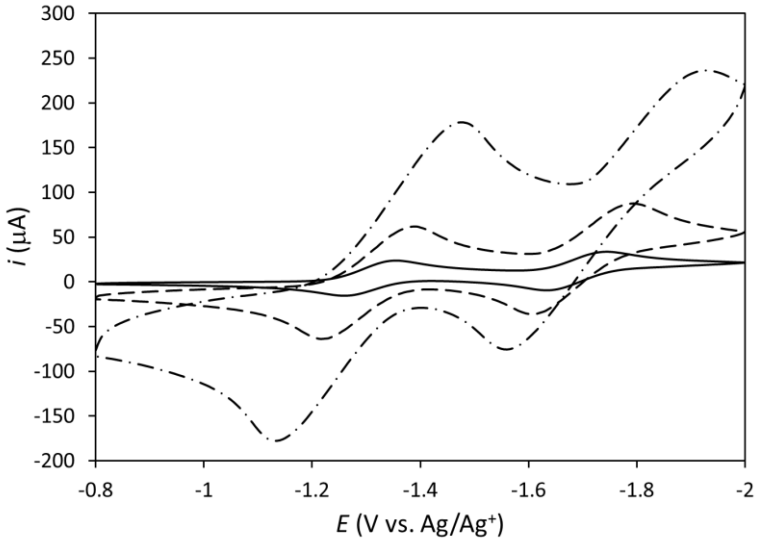

Figure 45: Cyclic voltammograms of 2.16 mM DNT in acetonitrile/100 mM NBu_4ClO_4 at scan rates of 100 (solid), 1000 (dashed), and 10,000 mV/s (dot-dashed). Working electrode: 1.6 mm diameter Au disk, reference: Ag/10 mM $AgNO_3$, auxiliary: Pt wire. T = 21 °C.

At scan rates of 100 mV/s and higher, the CVs of DNT in anhydrous acetonitrile are consistent with the electron transfer mechanism depicted in Figure 43, although it is impossible from this experimental data to determine which reduction path is followed. The increased separation of the cathodic and anodic peaks at higher scan rates is indicative of a moderately sluggish electron transfer between the electrode and DNT.[1] When the working electrode was operated at a potential sufficiently negative to reduce DNT, a substance of intense blue color was observed diffusing away from the electrode surface. This type of coloration was observed previously by Fornazini and coworkers; however, no explanation as to the source of the color was offered.[18] Subsequently, we conclusively showed that the blue color observed for solutions of DNT and basic compounds in dimethyl sulfoxide arises from the deprotonation of DNT.[176] Because the radical anion and subsequently formed dianion resulting from the reduction of DNT are both expected to be at least somewhat basic, it is likely that neutral, unreacted DNT is

deprotonated by electrochemically reduced DNT diffusing away from the electrode. To test this hypothesis, a solution of 10 mM DNT with 100 mM NBu_4ClO_4 was reduced at a constant potential of –2.0 V. The resulting product of the bulk reduction was not sufficiently stable to allow for isolation and purification. Therefore, an aliquot was removed after ten minutes and a visible absorption spectrum measured of this sample. This resulting spectrum was then compared to the visible spectrum of an acetonitrile solution of 0.2 mM DNT and 10 mM tetrabutylammonium hydroxide. These spectra are presented in Figure 46. For clarity, absorbances are shown normalized to their absorbance maxima.

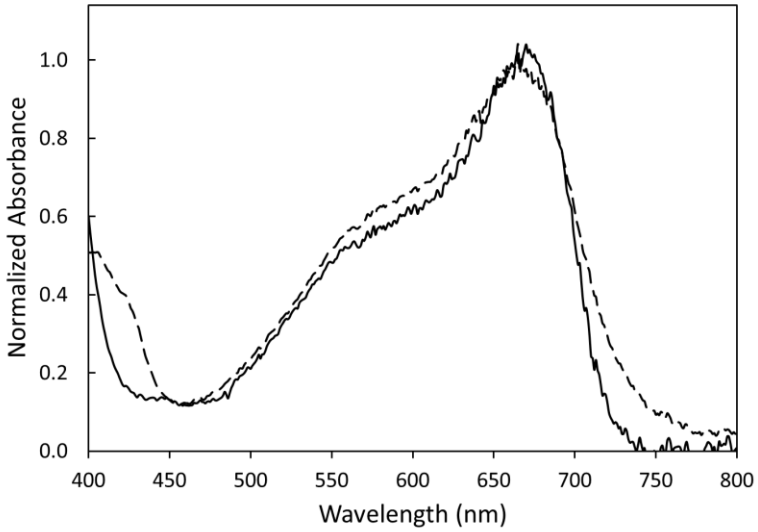

Figure 46: Normalized visible spectrum for an aliquot removed from an electrochemical cell after bulk reduction of DNT in acetonitrile (solid) and for a solution of 0.20 mM DNT with 10 mM NBu_4OH (dashed).

The spectra presented in Figure 46strongly suggest that the blue color emanating from the working electrode is a result of the deprotonation of unreacted DNT. As we show in the following section, protonation of the DNT radical anion results in further electrochemical reduction. Since unreacted DNT may serve as a proton source, the protonated form of electrochemically reduced DNT may then undergo the further

reactions outlined in Figure 44. Because the intermediate steps of this broader mechanism (and their reduction potentials and pKa values) are not clearly defined, quantitative fitting of CVs for DNT in unbuffered acetonitrile is difficult. Therefore, the electrochemical characteristics of DNT in buffered acetonitrile solutions are considered.

6.3.2 Voltammetry with pH buffered acetonitrile solutions

Because the radical anion formed when DNT is electrochemically reduced is capable of deprotonating DNT itself, cyclic voltammetry was performed with acetonitrile solutions of known H^+ concentration in order to gain a better understanding of the electrochemistry of DNT. Since hydrogen is reduced on gold in the potential range of interest,[194] these experiments were carried out with a large excess of triethylamine (100× DNT concentration) to keep the free H^+ concentration low. Initial experiments were performed with solutions containing 1.00 mM DNT along with 100 mM triethylamine. A CV of this solution is shown in Figure 47.

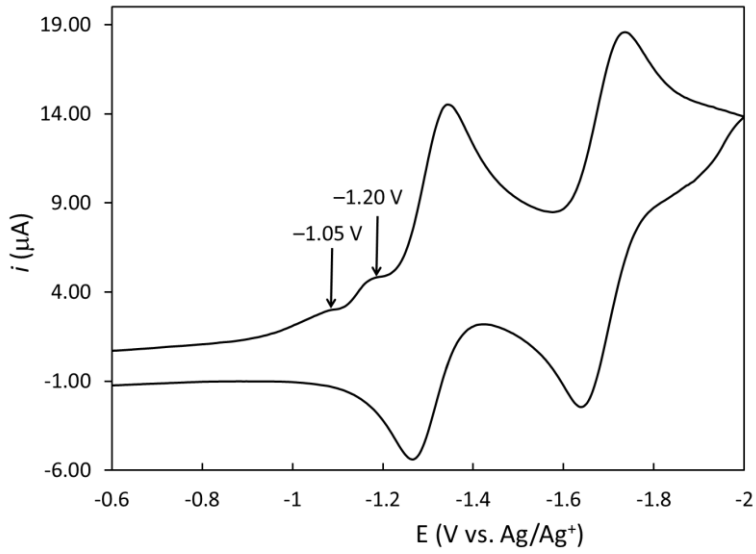

Figure 47: Cyclic voltammetry of 1.00 mM DNT in acetonitrile/100 mM NBu_4ClO_4 + 100 mM triethylamine. Working electrode: 1.6 mm diameter Au disk, reference: Ag/10 mM $AgNO_3$, auxiliary: Pt wire. Scan rate = 100 mV/s, T = 21 °C.

The appearance of small reductive current maxima at –1.05 and –1.20 V are a result of a slight increase of the proton concentration, likely due to a minor water contamination (See Figure 48). Aside from these two small peaks, the remainder of the CV is consistent with the nonprotic mechanism presented in Figure 1 in that the oxidative and reductive waves in the voltammogram have similar current magnitude. The potential separation of the oxidative and reductive peaks has decreased to 62 and 80 mV for the peaks centered at –1.30 and –1.68 V, respectively, at 100 mV/s. More importantly, no blue-colored products were observed during these experiments.

Subsequent experiments were performed with increasing concentrations of $HClO_4$, a well-known strong acid in acetonitrile (pK_a = –8.8),[195] to determine the effect of H^+ addition to the solution and the stoichiometry of the reaction of DNT with H^+. Cyclic voltammograms of 1.00 mM DNT in 100 mM triethylamine solutions containing a varying concentration of $HClO_4$ are presented in Figure 48. For clarity, only the first cycle is shown.

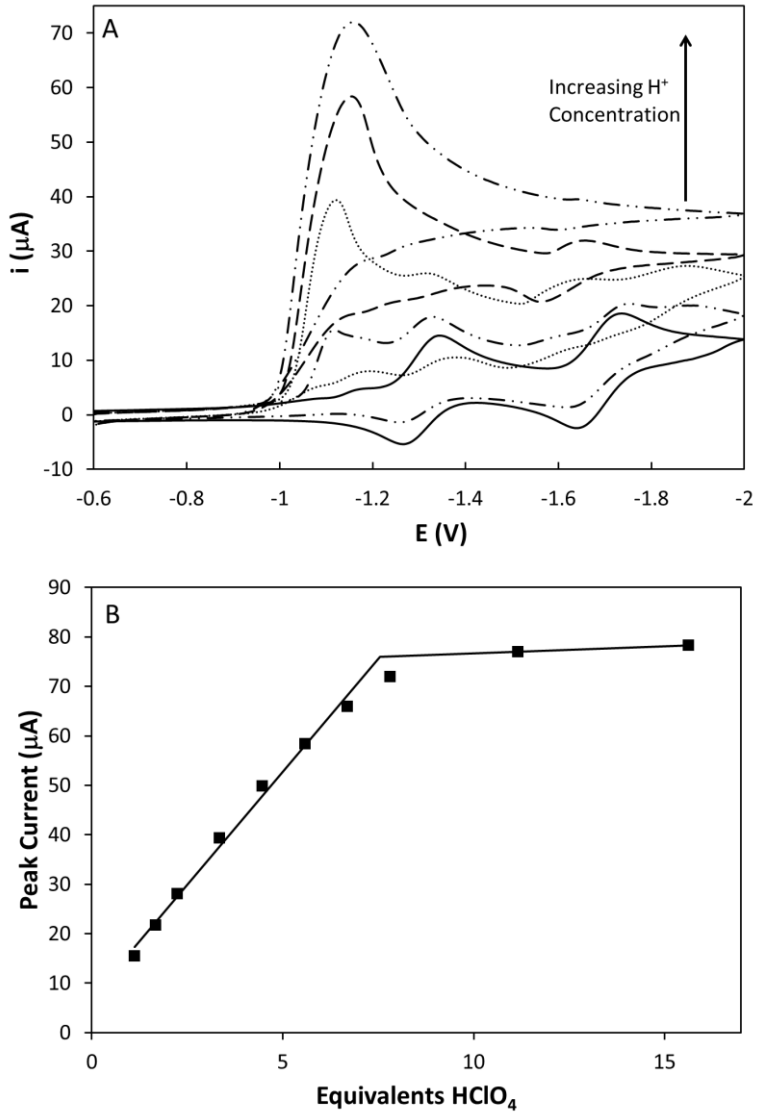

Figure 48: Cyclic voltammograms for 0–8 mM $HClO_4$ (A) and plot of peak current at –1.1 V with respect to $HClO_4$ concentration (B) for 1.00 mM DNT in acetonitrile/100 mM NBu_4ClO_4 + 100 mM triethylamine. Working electrode: 1.6 mm diameter Au disk, reference: Ag/10 mM $AgNO_3$, auxiliary electrode: Pt wire. Scan rate = 100 mV/s, T = 21°C.

As the concentration of added H^+ and thereby the ratio of triethylammonium and triethylamine is increased, a sharp increase in the magnitude of the irreversible peak located at –1.05 V is observed. The peaks located at –1.30 and –1.68 V slowly decrease in intensity until, at 8 equivalents of H^+, they become negligible in intensity. At concentrations of H^+ that are less than 7-fold excess to the concentration of DNT, a linear relationship is observed between the concentration of H^+ and the peak current observed at –1.05 V. No further substantial increase in peak current is observed when H^+ concentrations are greater than 8 times the concentration of DNT. This indicates that the overall reduction of DNT in the presence of the pH buffer triethylammonium/triethylamine requires 8 protons to progress to completion. In order to reduce DNT to 2,4-diaminotoluene as laid out in the scheme presented in Figure 44, a total of 12 electrons and 12 protons would be required. In fact, the only routes that utilize a total of 8 protons all stop with the production of 2,4-bis(*N*-hydroxylamino)toluene. Therefore, we conclude that, in the presence of triethylammonium/triethylamine buffers, DNT is reduced only to 2,4-bis(*N*-hydroxylamino)toluene at the potentials accessible in acetonitrile, as had previously been observed for DNT by polarography in aqueous solutions of neutral or alkaline pH.[28]

The reduction of DNT in the presence of triethylammonium/triethylamine buffer occurs at a potential substantially less negative than is observed in aprotic conditions. This indicates that free DNT is not the species being reduced but rather a product of the interaction of DNT with triethylammonium, likely the DNT–triethylammonium hydrogen bond complex. A similar effect is also observed for nitrobenzene in DMF at a dropping mercury electrode upon the addition of a proton source.[189] Conversely, if the reduction of DNT occurred before protonation, the onset of reduction would not occur until the applied potential has reached approximately –1.25 V (the potential at which DNT reduction is first observed in the aprotic experiments). In this case, an increase in the current observed at –1.30 V would be observed rather than the formation of a new discrete peak. Such alternative pathways to the complete reduction of DNT are likely the

source of several smaller peaks observed at intermediate potentials in Figure 48 for additions of 1–6 proton equivalents.

It is important to point out that, at triethylammonium concentrations less than 8 equivalents when compared to DNT, the observed CVs are characteristic of both protic and aprotic environments. This is most clearly evident in the CV measured with 1 mM added $HClO_4$. In this voltammogram, the peak at –1.05 V has increased substantially over that for aprotic environment while the reductions centered at –1.30 and –1.68 V are still clearly present. This may be explained as follows: upon the initial reduction of the DNT–triethylammonium complex, excess protons are rapidly consumed by the electrochemical reduction products. Because the electrochemical reduction products are localized near the electrode surface, a local pH change in the volume immediately adjacent to the electrode is observed. Once all of the triethylammonium available in this limited volume is deprotonated, the voltammogram begins to show characteristics similar to those of an aprotic environment.

Lastly, it is interesting note that the reduction of DNT to 2,4-bis(*N*-hydroxylamino)toluene in aqueous solutions takes place as two discrete reductions separated by approximately 100 mV in a polarographic experiment.[28] Moreover, the *chemical* reduction of DNT with Na_2S in an aqueous solution results in the formation of largely 2-nitro-4-aminotoluene, supporting the conclusion that the first reduction of DNT is thermodynamically more favorable than the second reduction.[196] By contrast, a single concerted reduction wave associated with this same reduction in acetonitrile is observed. Clearly, the difference in solvation between these two environments results in a rather large change in the separation of the first and second reduction potentials of DNT.

6.4 Conclusions

In this work, we have shown that, in anhydrous acetonitrile, 2,4-dinitrotoluene undergoes two individual one-electron transfers that are readily resolved by cyclic voltammetry. The product of the electrochemical DNT reduction is capable of quickly

deprotonating a second uncharged DNT molecule, producing the stable blue color indicative of deprotonated DNT. After abstracting a proton from DNT, the protonated species may then undergo further reduction, making quantitative mechanistic interpretation of the cyclic voltammograms difficult.

Upon addition of a triethylammonium/triethylamine buffer to the acetonitrile solution, the two reduction waves gradually decrease in intensity while one large reduction wave at a less negative potential than the waves associated with formation of the radical anion begins to form. This new reduction wave increases in intensity with the addition of additional protons until a triethylammonium concentration 8 times the concentration of DNT is present in the solution. This concentration of triethylammonium is consistent with the 8 e^-, 8 H^+ reduction of DNT to form 2,4-bis(*N*-hydroxylamino)toluene.

Furthering the understanding the reduction mechanism of DNT will assist in the development and implementation of electrochemical sensors for DNT. For example, taking advantage of the 8-electron transfer for DNT reduction in solutions containing a source of readily available protons will greatly improve the sensitivity of developed electrochemical DNT sensors.

7 CHAPTER SEVEN

Receptor-Based Detection of 2,4-Dinitrotoluene using Modified Three-Dimensionally Ordered Macroporous Carbon Electrodes

In part from:

Fierke, M. A.; Olson, E. J.; Bühlmann, P.; Stein, A. "Receptor-Based Detection of 2,4-Dinitrotoluene using Modified Three-Dimensionally Ordered Macroporous Carbon Electrodes" *Manuscript Submitted.*

This work was a collaboration between this author and M. A. Fierke, who carried out the synthesis, modification, and characterization of 3DOM carbon electrodes. Cyclic voltammetry experiments were shared between these two authors.

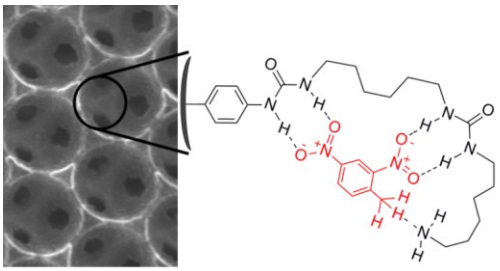

Detection of explosives, such as 2,4,6-trinitrotoluene (TNT), is becoming increasingly important. Here, 2,4-dinitrotoluene (DNT, a common analogue of TNT) is detected electrochemically. A receptor based electrode for the detection of DNT was prepared by modifying the surface of the walls of three-dimensionally ordered macroporous (3DOM) carbon. Nitrophenyl groups were first attached by the electrochemical reduction of 4-nitrobenzenediazonium ions, followed by potentiostatic reduction to aminophenyl groups. Chemical functionalization reactions were then performed to synthesize the receptor, which contains two urea groups, and a terminal primary amine. Detection of DNT using cyclic voltammetry was impeded by a large background current that resulted from the capacitance of 3DOM carbon. Detection by square wave voltammetry eliminated the background current and improved the detection limit. Unfunctionalized 3DOM carbon electrodes showed no response to DNT, wheras the receptor-modified electrodes responded to DNT with a detection limit of 10 μM. Detection of DNT was possible even in the presence of interferents such as nitrobenzene.

7.1 Introduction

The detection of explosives, including 2,4,6-trinitrotoluene (TNT), is an important analytical problem of relevance for the prevention of terrorism and for the detection of military explosives (including leftover landmines) and environmental hazards from improperly disposed explosives.[197] Rather than attempting to detect TNT directly, researchers often focus on detecting 2,4-dinitrotoluene (DNT).[5,6,112] DNT, which is a common impurity in TNT-based explosives,[14] exhibits a higher volatility than TNT, allowing for considerably more sensitive detection. In fact, DNT is the component of TNT-based explosives that canines are able to detect with very good sensitivity.[14,183]

Many methods of DNT detection have been reported, including photoluminescence and fluorescence quenching,[15,16] detection of reduction or degradation products,[17,19,198] vapor adsorption on a modified microcantilever,[20] electronic noses and sniffers,[5,21] electrochemical impedance detection,[199] and detection by combining capillary electrophoresis and electrochemical detection with a porous carbon-modified electrode.[23] For the purpose of miniaturization, electrochemical detectors are attractive for sensing explosives.[24-27,199] Electrode miniaturization offers many benefits, including reduced cost, which enhances the feasibility of creating sensor networks, and greater portability. Moreover, the adaptation of an electrochemical sensor to detect explosive compounds is rather straightforward, as their structures make them inherently redox active. A common theme in most published electrochemical sensors for DNT, however, is that their selectivity is determined largely by the redox potential of the analyte. The addition of a supramolecular receptor that specifically binds the analyte has the potential for greatly improving both the selectivity and sensitivity of detection.[200] In fact, molecular recognition schemes have previously been developed for the electrochemical detection of the related compound TNT.[9,201]

In this work, a receptor-modified, three-dimensionally ordered macroporous (3DOM) carbon electrode is used to detect DNT electrochemically. 3DOM carbon, a conductive material composed of glassy carbon walls that surround an ordered array of

interconnected pores (Figure 49), is a particularly attractive electrode material due to its highly accessible and relatively large surface.[202,203] For sensing applications, 3DOM carbon has previously been used as an electrode for solid-state ion-selective and reference electrodes, and extremely low detection limits and very stable responses were achieved.[95,204-206] As prepared, the walls of 3DOM carbon do not contain many functional groups,[204] and further functionalization is required to attach receptor molecules. The functionalization scheme used to modify the walls of the pores in 3DOM carbon is shown in Figure 49. After functionalization with nitrophenyl groups by diazonium reduction, the nitro groups are reduced to amino groups, which provide an aminophenyl functionalized surface that can be chemically modified by many different methods.[207] Here, 1,6-diisocyanato hexane was reacted with the aminophenyl groups, followed by reaction with 1,6-hexanediamine to give a receptor with two urea groups and a terminal aliphatic amine to interact with DNT.

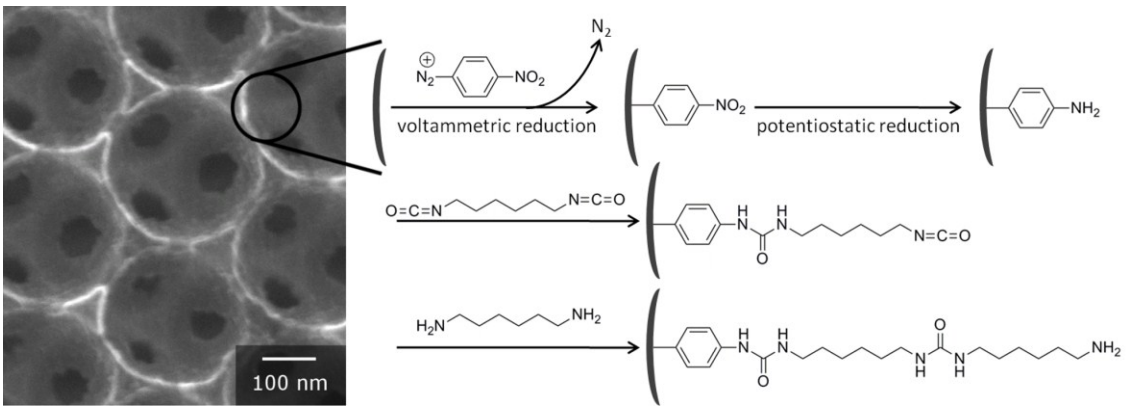

Figure 49: Scheme for functionalization of 3DOM carbon (left) to produce receptor-modified electrodes through electrochemical and chemical modification steps.

This receptor molecule was chosen on the basis of previous work, which conclusively showed that in DMSO solutions, the methyl group of DNT is deprotonated by bases such as amines.[176] In the case of the receptor that we designed herein, we expected that DNT would be deprotonated by the terminal amino group of the receptor. The resulting

deprotonated DNT would exhibit partial anionic character at each nitro group due to resonance. Because urea moieties are well known to be good hydrogen bond donors,[207] they are expected to interact rather strongly with the electron-rich nitro groups. By stabilizing the anionic nature of the nitro groups of deprotonated DNT, binding of DNT with the developed receptor would likely lower the pK_a of DNT and therefore further stabilize the DNT:receptor complex. The anticipated geometry of the DNT:receptor interaction is shown in Figure 50.

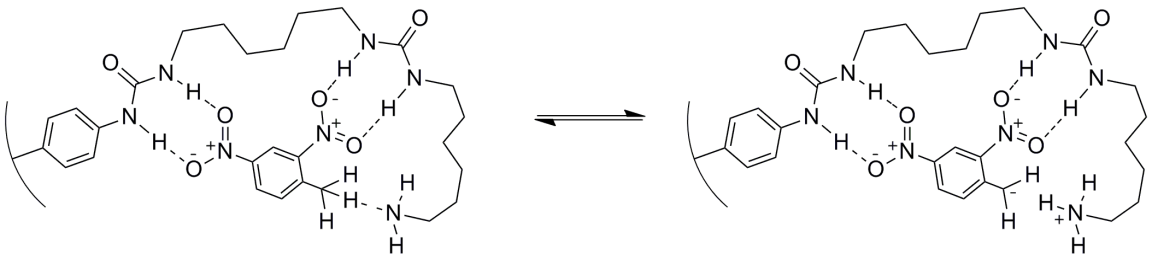

Figure 50: The anticipated interaction between DNT and the receptor on the surface of the 3DOM carbon.

In this article, we describe the synthesis and characterization of the receptor-modified 3DOM carbon electrodes and evaluate their performance as DNT sensors in cyclic voltammetry (CV) and square wave voltammetry (SWV) experiments. By SWV, a detection limit of 10 μM was established.

7.2 Experimental Section

7.2.1 Materials

All reagents were of the highest commercially available purity. Resorcinol, 4-nitrobenzenediazonium tetrafluoroborate, 1,6-diisocyanatohexane, 1,6-hexanediamine, boron trichloride (1.0 M in heptane), *t*-butyl lithium (1.7 M in pentane), 2,4-dinitrotoluene, and benzotrifluoride (α,α,α-trifluorotoluene) were from Sigma-Aldrich (St. Louis, MO), tetrabutylammonium chloride and tetrabutylammonium tetrafluoroborate were from Fluka (Milwaukee, WI), formaldehyde (37% in H_2O) was

from Fisher Scientific (Pittsburgh, PA), 1-bromo-3,5-bis(trifluoromethyl)benzene was from SynQuest Laboratories (Alachua, FL), unplasticized PVC sheets were from Goodfellow (Oakdale, PA), and Ni mesh was a gift from Dexmet (Branford, CT). All chemicals were used as received.

7.2.2 Synthesis of 3DOM Carbon Electrodes

3DOM carbon monoliths were synthesized as previously described.[205] In brief, colloidal crystal templates composed of 425 nm poly(methyl methacrylate) (PMMA) spheres were infiltrated with a base-catalyzed resorcinol-formaldehyde prepolymer. After heating at 85 °C for 3 days to crosslink the polymer, the infiltrated templates were pyrolyzed at 900 °C for 2 hours with a ramp rate of 5 °C·min^{-1} under flowing nitrogen to remove the PMMA template and carbonize the crosslinked resorcinol-formaldehyde polymer. After polishing the porous carbon with sandpaper to produce monoliths with typical dimensions of 5 mm × 5 mm × 0.5 mm, the monoliths were affixed to a nickel mesh current collector using resorcinol-formaldehyde carbon precursor that had been heated for ca. 20 min, followed by curing at 85 ˚C overnight to produce 3DOM carbon electrodes.

7.2.3 Nitrophenyl Functionalization of 3DOM Carbon Electrodes

Nitrophenyl functional groups on the walls of the pores in 3DOM carbon were produced electrochemically by an adapted version of a previously published method.[208,209] Functionalization of the porous electrode requires a high concentration of the diazonium salt because diffusion through the pores is not fast enough to allow for replenishment of the solution in the pores from the bulk solution. A non-aqueous reference electrode and a platinum wire counter electrode were placed in a 25 mL round bottom flask. Approximately 2 mL of the functionalization solution (an acetonitrile solution containing 0.1 M tetrabutylammonium tetrafluoroborate electrolyte and saturated with 4-nitrobenzenediazonium tetrafluoroborate) was added. After purging the solution

with argon for 10 minutes, the 3DOM carbon electrode was submerged in the solution. Bubbles immediately emerged from the carbon electrode, indicating wetting of the porous carbon by the electrolyte solution. The functionalization was carried out using cyclic voltammetry, with a window of +0.8 to –1.7 V vs. Ag/10 mM $AgNO_3$ (CH_3CN) and a sweep rate of 10 $mV \cdot s^{-1}$ for 2–4 cycles (until consecutive cycles overlapped well). After functionalization, the electrode was thoroughly cleaned by soaking in fresh acetonitrile several times.

7.2.4 Aminophenyl Functionalization of 3DOM Carbon Electrodes

The nitrophenyl functional groups on the walls of the 3DOM carbon were electrochemically reduced to aminophenyl functional groups. The modified electrode was placed in an aqueous 0.1 M phosphate buffer ($NaH_2PO_4 \cdot H_2O/Na_2HPO_4 \cdot 7H_2O$) solution (10 v/v% ethanol was added to facilitate wetting, pH = 7.1) with a double-junction Ag/AgCl reference electrode and a platinum wire counter electrode. A constant potential of –1.4 V versus the reference electrode was applied for two hours. The electrodes were then cleaned by soaking in fresh water/ethanol solution several times.

7.2.5 Reaction with 1,6-Diisocyanatohexane

The aminophenyl-modified electrodes were reacted with 1,6-diisocyanatohexane, forming a urea group between an isocyanate functionality and the $–NH_2$ of the aminophenyl on the surface of the carbon electrode. This process leaves a free isocyanate group on the end of the receptor. An aminophenyl functionalized electrode was placed in a small flask. Approximately 4 mL neat 1,6-diisocyanatohexane was added to the flask, completely covering the carbon component of the electrode. The flask was attached to a water-cooled condenser and heated in an oil bath at 120 °C for 24 h. The electrode was then removed from the flask and cleaned by soaking in fresh toluene several times.

7.2.6 Reaction with 1,6-Hexanediamine

A second urea group and a terminal amino group were formed by reacting the isocyanate-functionalized electrodes with 1,6-hexanediamine, forming the complete receptor. An isocyanate-functionalized electrode was placed in a small flask. Approximately 4 mL of a 10 w/w% solution of 1,6-hexanediamine in toluene was added. The flask was attached to a water-cooled condenser and heated in an oil bath at 120 °C for 24 h. The electrode was then removed from the flask and cleaned by soaking in fresh toluene several times.

7.2.7 Electrode Encasement

Before use, fully modified electrodes were encased in unplasticized poly(vinyl chloride) (PVC) to provide mechanical stability and electrical insulation. PVC sheets sealed with commercial PVC adhesive were used to encase the entire electrode, except for the functionalized 3DOM carbon and a small portion of the Ni mesh on the opposite end of the electrode construct (to allow for electrical contact).

7.2.8 Synthesis of NBu_4BArF_{24}

After optimization, a solvent/electrolyte combination of benzotrifluoride with tetrabutylammonium sodium tetrakis[3,5-bis(trifluoromethyl)phenyl]borate (NBu_4BArF_{24}) was selected.

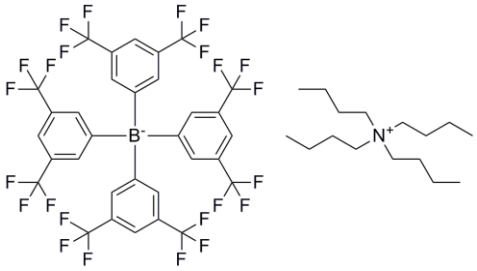

Figure 51: Structure of the electrolyte tetrabutylammonium tetrakis[3,5-bis(trifluoromethyl)phenyl]borate (NBu_4BArF_{24}).

Benzotrifluoride was chosen because it does not interact significantly with the receptor on the carbon surface, which would prevent detection of DNT. It also does not dissolve or soften the electrode encasement material. NBu_4BArF_{24} is soluble to 100 mM in benzotrifluoride and sufficiently lowers the resistance to allow electrochemical experiments to be carried out.

Sodium tetrakis[3,5-bis(trifluoromethyl)phenyl]borate was prepared as follows by adaptation of a previously described procedure for the synthesis of sodium tetrakis[3,5-bis(trifluoromethyl)phenyl]borate.[50] All synthetic steps were carried out in an argon atmosphere, unless otherwise noted. A 1.7 M solution of *t*-butyl lithium (76 mL, 130 mmol, 9.2 equiv) was added over 30 min by addition funnel to a stirred solution of 1-bromo-3,5-bis(trifluoromethyl)benzene (10 mL, 56 mmol, 4.7 equiv) chilled to –76 °C. After the solution was allowed to stir for 30 min, a 1.0 M BCl_3 solution (12 mL, 12 mmol, 1 equiv) was added dropwise by syringe over 10 min. Upon complete addition of the BCl_3 solution, the reaction mixture was warmed slowly to room temperature and stirred vigorously for an additional 2 h. The crude mixture was then slowly poured into 100 mL of NaCl-saturated water (the remaining steps are not air-sensitive) and vigorously mixed. This mixture was then extracted with diethyl ether (3×100 mL). The organic layers were combined, dried with anhydrous $MgSO_4$, and rotary evaporated to yield a pale yellow oil. This oil was dried at 100 °C under vacuum to produce a tan-yellow solid. The product was recrystallized 3 times from benzotrifluoride by addition of hexane to produce high purity $NaBArF_{24}$ as a fine white powder (40% yield). ^{1}H NMR (300 MHz, acetone-d_6, δ): 7.69 (s, *p*-Ar*H*, 4H), 7.81 (s, *o*-Ar*H*, 8H). These NMR shifts are in good agreement with previously published results for this compound.[210-212]

NBu_4BArF_{24} was synthesized by metathesis from tetrabutylammonium chloride and sodium tetrakis[3,5-bis(trifluoromethyl)phenyl]borate: 8.0 g of sodium tetrakis[3,5-bis(trifluoromethyl)phenyl]borate and 1.0 g of tetrabutylammonium chloride were added to a separatory funnel containing 300 mL water and 300 mL benzotrifluoride. The mixture was shaken until all of the salt dissolved. The organic layer was collected,

washed three times with 300 mL water, dried with $MgSO_4$, and filtered. The solvent was removed by rotary evaporation and further drying under vacuum at 75 °C for 48 h, yielding NBu_4BArF_{24} as a pale yellow, wax-like material in quantitative yield. ^{1}H NMR (300 MHz, acetone-d_6, δ): 1.00 (t, J_{HH} = 7.2 Hz, –CH_3, 12H), 1.46 (m, –CH_2CH$_3$, 8H), 1.86 (m, NCH$_2$CH_2–, 8H), 3.48 (m, NCH_2–, 8H), 7.69 (s, *p*-Ar*H*, 4H), 7.80 (s, *o*-Ar*H*, 8H).

7.2.9 Characterization

The nitrophenyl and aminophenyl functionalized 3DOM carbon samples were characterized by X-ray photoelectron spectroscopy (XPS). After removal from the Ni mesh, the carbon samples were mounted on the sample stage using conductive carbon sticky tape. XPS measurements were carried out on a Surface Science SSX-100 instrument with an Al anode (Kα X-rays at 1486.66 eV) operated at 10 kV and 20 mA. Measurements were performed at room temperature, with a pressure below 1×10^{-8} torr in the analysis chamber. FTIR spectra for all functionalized 3DOM carbon samples were obtained using KBr pellets in a Nicolet Magna-IR 760 spectrometer.

7.2.10 Electrochemical Measurements

All cyclic voltammetry measurements were performed at room temperature with a CHI600C Potentiostat (CH Instruments, Austin, TX) while square wave voltammetry experiments were performed with a Cypress Systems 1090 Potentiostat (Cypress Systems, Lawrence, KS). All electrochemical experiments utilized a three-electrode setup with a 3DOM carbon electrode as the working electrode, a Ag/10 mM $AgNO_3$ acetonitrile reference electrode (CH Instruments) and a 0.25 mm Pt wire coil (99.998 %, Alfa Aesar, Ward Hill, MA) as the auxiliary electrode. Each sample solution contained 100 mM NBu_4BArF_{24} in benzotrifluoride; DNT was introduced to the electrolyte solution by addition of stock solutions. Each sample was thoroughly purged of oxygen by

bubbling high-purity argon for 20 minutes prior to each measurement. An argon atmosphere was maintained over the solution during measurements. Scan rates and window sizes for each experiment are indicated below. For CV experiments, multiple cycles were performed, but only cycle 2 is shown for clarity. Electrodes were evacuated using a vacuum pump for at least one hour between uses to allow for better wetting with the solution for the next experiment.

7.3 Results and Discussion

7.3.1 3DOM Carbon Electrode Functionalization

3DOM carbon electrodes were first electrochemically functionalized with nitrophenyl groups by voltammetric reduction of 4-nitrobenzenediazonium (Figure 52). In the first cycle, a large, irreversible peak at –0.5 V was observed, and is attributed to the reduction of 4-nitrobenzenediazonium to its aromatic radical,[208,209] which then bonds with the surface of the carbon pore walls. In the subsequent voltammetric cycles, the peak decreased until it was no longer present in cycle 4, indicating maximum coverage of the 3DOM C surface with nitrophenyl groups. The number of cycles required to complete the reaction depended on the surface area of the 3DOM carbon monolith.

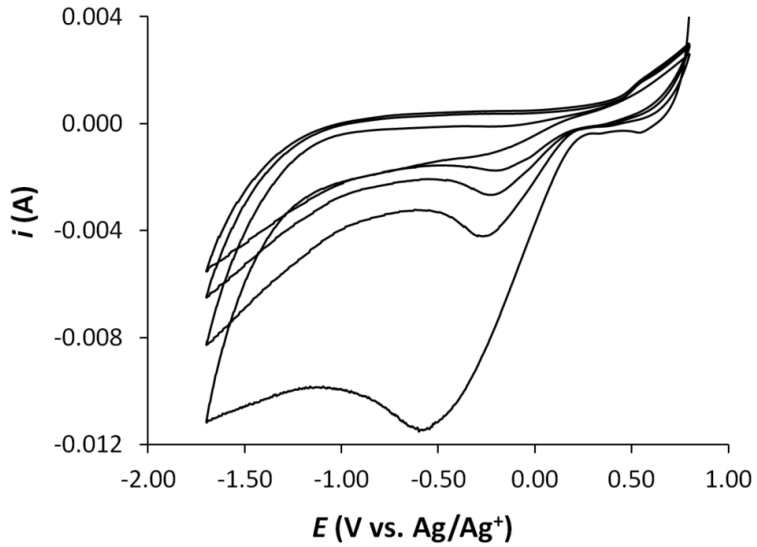

Figure 52: Voltammetric functionalization of a 3DOM carbon electrode with a saturated acetonitrile solution of 4-nitrobenzenediazonium tetrafluoroborate (with 0.1 M tetrabutylammonium tetrafluoroborate as the electrolyte), producing nitrophenyl functionalization on the pore walls of the carbon. A scan window of +0.8 to –1.7 V and a scan rate of 10 $mV \cdot s^{-1}$ were used.

The nitro groups on the nitrophenyl modified electrodes were then potentiostatically reduced at –1.4 V in an aqueous phosphate buffer solution. XPS was carried out on reduced and non-reduced samples to verify the reduction of nitro groups to amino groups (Figure 53). The bonding environment of nitrogen atoms can be determined by examining the N_{1s} region. Nitrogen atoms in nitro groups produce a peak at 406 eV whereas nitrogen atoms in amino groups produce a peak at 400 eV.[208] The XPS spectrum of nitrophenyl functionalized carbon exhibited peaks at both of these positions (Figure 53A). The peak at 406 eV indicates that the walls of the 3DOM carbon were successfully modified with nitrophenyl groups. The additional peak at 400 eV after grafting of nitrophenyl groups has been observed previously.[213-218] While it suggests the presence of reduced nitrophenyl groups on the surface of the carbon, the peak likely indicates that azo

groups were present on the functionalized surface,[215,216] possibly as part of a multilayer film.[218,219]

After potentiostatic reduction of the nitrophenyl modified electrode in an aqueous buffer, only one peak at 400 eV was observed in the XPS spectrum (Figure 53B), consistent with the presence of aminophenyl functional groups.[215,217,220]

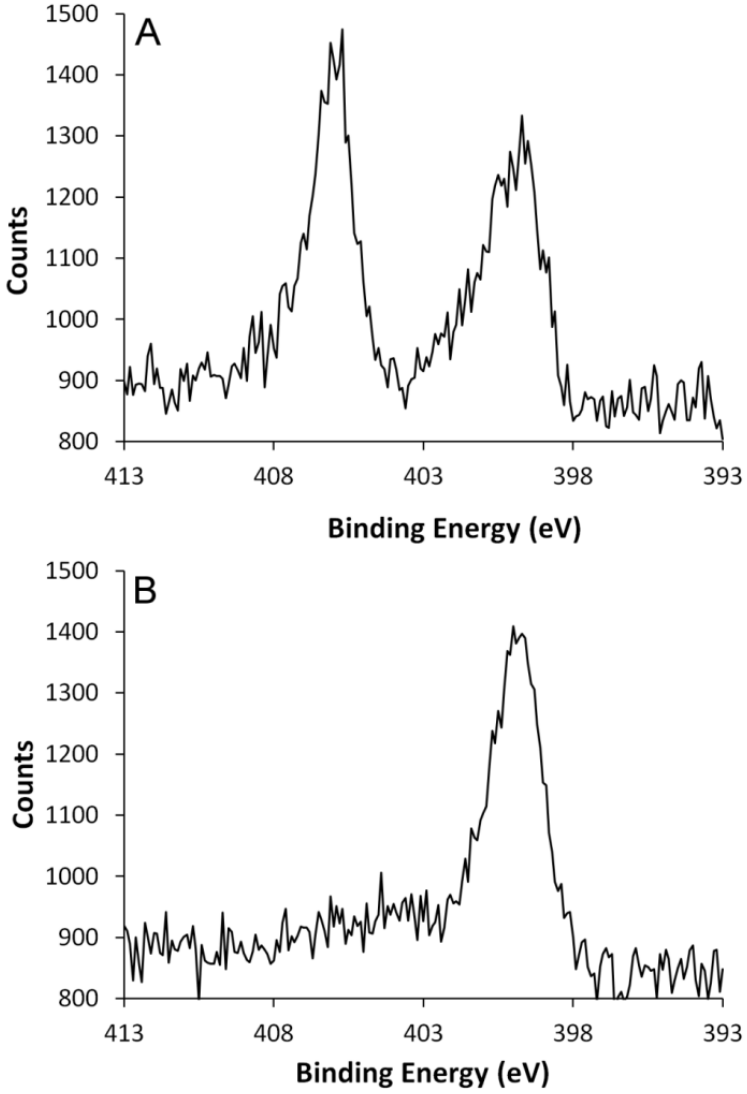

Figure 53: XPS spectra of the N_{1s} region of (A) nitrophenyl and (B) aminophenyl functionalized carbon.

After additional chemical functionalization to complete the synthesis of the receptor, FTIR spectroscopy was performed to confirm the presence of the desired functional groups (Figure 54). A low concentration of sample in the KBr pellets was required, as carbon absorbs strongly in the infrared.[221] However, the concentration was sufficient to achieve spectra with peaks characteristic of the functional groups attached to the surface of the 3DOM carbon walls. A sample of unfunctionalized 3DOM carbon was also characterized for comparison. The large peak at ~3400 cm^{-1} in each spectrum is due to water adsorbed on the surface of the carbon. In the unfunctionalized sample (Figure 54A), the peak at 1575 cm^{-1} is assigned to the skeletal structure of the 3DOM carbon.[222,223] The peaks at 1200 cm^{-1} and 1135 cm^{-1} result from C–O stretching in the oxygen-containing functional groups that exist on the as-made carbon.[204,224,225]

After voltammetric functionalization with nitrophenyl groups and potentiostatic reduction to aminophenyl groups, new peaks appear in the FTIR spectrum (Figure 54B). The peak at 1514 cm^{-1} is due to the aromatic C–C stretch of the aminophenyl group.[226] The expected amine N–H stretch at ~3400 cm^{-1} overlaps with the water peak. However, the NH_2 deformation peak at 1597 cm^{-1} is present.[226,227]

Reaction of the aminophenyl functionalized carbon with 1,6-diisocyanatohexane forms a urea group between the amine and an isocyanate group. The attached functionality also contains an aliphatic chain and a terminal isocyanate group. As with the aminophenyl functionalized sample, the FTIR spectrum of diisocyanate funtionalized 3DOM carbon (Figure 54C) exhibits an aromatic C–C stretch at 1514 cm^{-1}. The aliphatic portion of the functionality is confirmed by the C–H stretching peaks at 2920 and 2850 cm^{-1}. The C=O stretch of the urea group appears at 1668 cm^{-1}, and the NH_2 deformation peak of the urea group is at 1615 cm^{-1}.[226]

The further reaction of the diisocyanate functionalized 3DOM carbon with 1,6-hexanediamine forms another urea group with the remaining isocyanate group, adding another aliphatic chain, and leaving a free primary amine. As expected, the FTIR spectrum for the diamine functionalized sample (Figure 54D) contains the aromatic C–C

stretch at 1514 cm^{-1}, C–H stretches from the aliphatic chains at 2920 and 2850 cm^{-1}, the C=O stretch of the urea group at 1668 cm^{-1}, and the NH_2 deformation peak of the urea group at 1615 cm^{-1}.[226] No peaks for the free primary amine are visible. The peak at ~3400 cm^{-1} is overlapped by the adsorbed water peak.

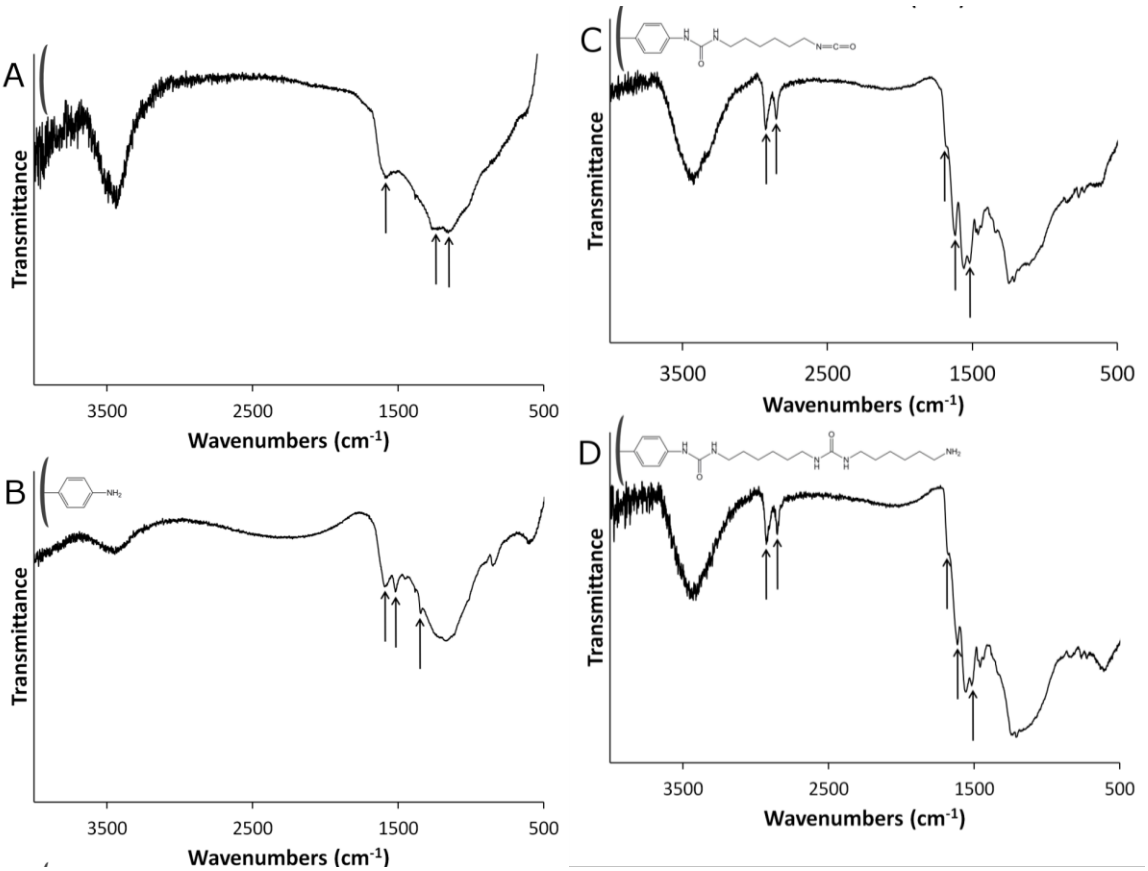

Figure 54: FTIR spectra of (A) unfunctionalized 3DOM carbon, and (B) aminophenyl-, (C) isocyanate-, and (D) diamine-functionalized 3DOM carbon. Insets show drawings of the carbon surface and the surface functionalities. The arrows point to the peaks described in the text.

7.3.2 Voltammetric Response to DNT

Initial characterization of the functionalized electrodes was performed with cyclic voltammetry to allow direct comparison to previously published CV methods for the detection of nitroaromatic molecules.[25,181] In one such study, a detection limit of 5 ppb for 2,4-DNT was achieved using cyclic voltammetry with a glassy carbon electrode modified with multi-walled carbon nanotubes. Several other nitroaromatic compounds could also be detected at higher detection limits.[228] A similar method was used to detect TNT and DNT with glassy carbon electrodes modified with ordered mesoporous carbon using adsorptive stripping voltammetry to achieve a detection limit of 1 ppb for 2,4-DNT.[229] Mesoporous silica (MCM-41) modified electrodes have also been used to detect 2,4-DNT and other nitroaromatic compounds.[30]

Before testing the fully-functionalized 3DOM carbon electrodes for their response to DNT, a gold electrode was used to investigate the reduction behavior of DNT in electrolyte solution (NBu_4BArF_{24} in benzotrifluoride) (Figure 55). After addition of 0.3 mM DNT to the electrolyte solution, two reduction waves appeared at –1.2 and –1.5 V vs. Ag/Ag^+. As expected, the magnitude of the peaks increased as the concentration of DNT in the solution increased to 0.6 mM. The presence of two reduction waves for DNT is consistent with previous work for nitrobenzene and 1,4-dinitrobenzene in acetonitrile.[230] In this previous work, a single reduction wave at –1.505 V vs. Ag/Ag^+ was observed for nitrobenzene while two reduction waves at –1.078 and –1.278 V vs Ag/Ag^+ were observed for 1,4-dinitrobenzene. Based on the behavior of the gold microelectrode, reduction peak(s) for DNT were expected at approximately –1.5 V for the modified 3DOM carbon electrode.

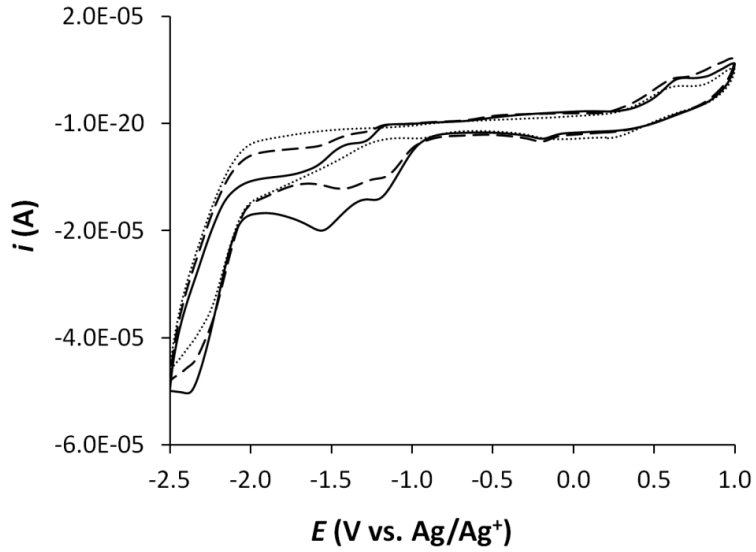

Figure 55: CV characterization of a gold electrode in benzotrifluoride/100 mM NBu_4BArF_{24} with varied DNT concentrations (····· 0 mM, – – – – 0.3 mM, and —— 0.6 mM). A scan window of –2.5 to +1 V starting at +0.2 V was used, with a scan rate of 100 $mV \cdot s^{-1}$. Only cycle 2 is shown.

When obtaining voltammograms of the fully-modified 3DOM carbon electrodes, a wide scan window (+2 to –5 V) was used to ensure that all possible peaks were observed. A slower scan rate (10 $mV \cdot s^{-1}$) was also required to obtain a well-shaped voltammogram. DNT concentrations of 0, 0.4, and 0.8 mM DNT were tested (Figure 56). After addition of 0.4 mM DNT, the current increased beginning at –1.0 V when compared to the background scan with 0 mM DNT. After addition of an additional 0.4 mM DNT (for a total of 0.8 mM DNT), a well-defined peak at about –1.7 V was observed. The magnitude of the peak continued to increase as the concentration of DNT in the solution was increased (data not shown).

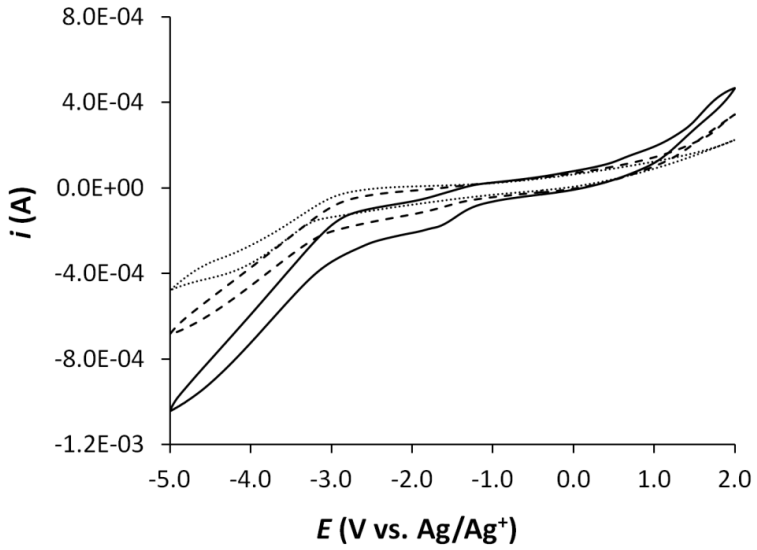

Figure 56: CV characterization of a fully functionalized 3DOM carbon electrode in benzotrifluoride/100 mM NBu_4BArF_{24} with varied DNT concentrations (····· 0 mM, – – – – 0.4 mM, and —— 0.8 mM). A scan window of –5 to +2 V starting at –0.4 V was used, with a scan rate of 10 $mV \cdot s^{-1}$. Only cycle 2 is shown.

7.3.3 Response of Unfunctionalized 3DOM Carbon

The response of unfunctionalized 3DOM carbon electrodes to DNT was tested in an identical manner to the functionalized electrodes (Figure 57). The first noticeable difference between the voltammograms of unfunctionalized and functionalized carbon is the total current, which is much larger for the unfunctionalized carbon. The electrochemical functionalization process blocks some micropores in the functionalized electrodes, lowering the surface area compared to the unfunctionalized electrodes. A baseline voltammogram (0 mM DNT) overlaps very well with voltammograms in solutions containing 0.2 and 0.6 mM DNT, indicating a lack of response of unfunctionalized 3DOM carbon electrodes to DNT. Detection of DNT occurred only after modification of the electrode, giving selective detection of DNT with this method. The system also did not respond to the common interferents phenol and nitrobenzene

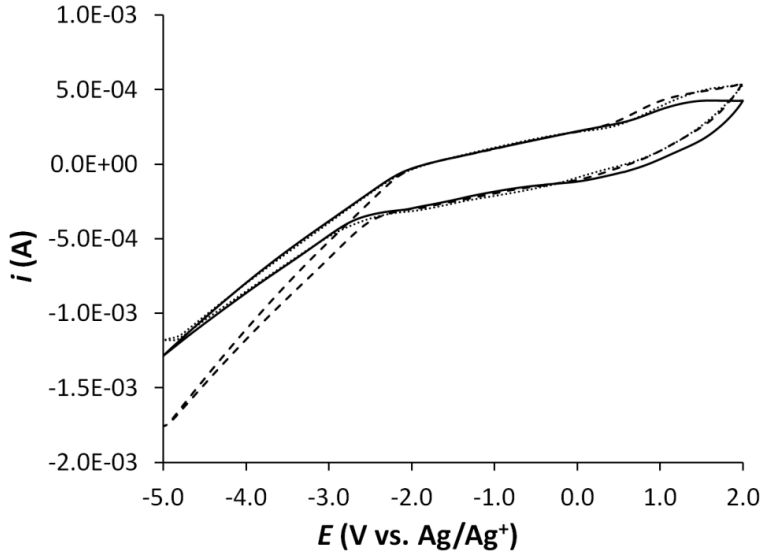

Figure 57: CV characterization of an unfunctionalized 3DOM carbon electrode in benzotrifluoride/100 mM NBu_4BArF_{24} with varied DNT concentrations (····· 0 mM, – – – – 0.2 mM, and —— 0.6 mM). A scan window of –5 to 2 V starting at –0.4 V was used, with a scan rate of 10 $mV \cdot s^{-1}$. Only cycle 2 is shown.

7.3.4 Detection of DNT in the Presence of Potential Interferents

Functionalized 3DOM carbon electrodes were tested for response to DNT in the presence of two potential interferents, nitrobenzene and phenol (Figure 58). After a baseline voltammogram (0 mM DNT) was measured, response to nitrobenzene was tested. In the presence of 1.0 mM nitrobenzene, no response was observed, and the total current decreased slightly due to the nitrobenzene blocking the surface. When the electrode was tested for response to DNT (0.6 mM) in the presence of 1.0 mM nitrobenzene, a peak at –2.5 V was observed, indicating a response to DNT even in the presence of nitrobenzene.

When a functionalized electrode was tested in the presence of phenol (1.0 mM), the total current decreased, as was observed in the nitrobenzene case, indicating no response to phenol. When DNT (0.6 mM) was added to the system, no response to DNT was

observed. It was hypothesized that the phenol was blocking the receptor sites. In order to test this hypothesis, the electrode was placed under vacuum overnight in order to remove the phenol, which has a high vapor pressure, from the electrode. After removal of the phenol, the receptor once again responded to DNT.

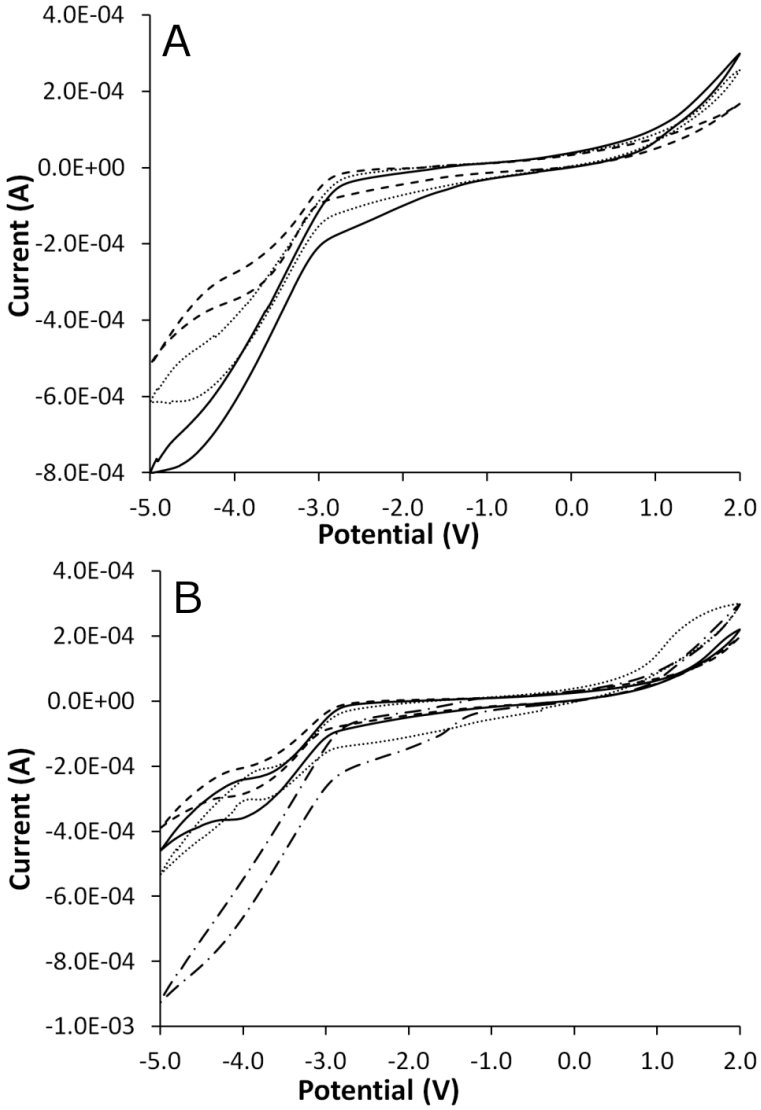

Figure 58: CV characterization of fully functionalized 3DOM carbon electrodes in the presence of interferents in benzotrifluoride/100 mM NBu_4BArF_{24}. A scan window of –5 to 2 V starting at –0.4 V was used, with a scan rate of 10 $mV \cdot s^{-1}$. Only cycle 2 is shown.

The interferents used were (A) nitrobenzene (····· 0 mM nitrobenzene, 0 mM DNT), (– – – – 1.0 mM nitrobenezene, 0 mM DNT), (—— 1.0 mM nitrobenzene, 0.6 mM DNT) and (B) phenol (····· 0 mM phenol, 0 mM DNT), (– – – – 1.0 mM phenol, 0 mM DNT), (— — 1.0 mM phenol, 0.6 mM DNT), (— · — 0 mM phenol, 1 mM DNT after vacuum removal of phenol).

Although cyclic voltammetry demonstrates a response of the fully-functionalized 3DOM carbon electrodes to DNT, the peak sizes are quite small. The rather poor limit of detection is not due to poor sensitivity of the technique, but rather an inability to distinguish between Faradaic and capacitive currents.[231] Because of the large capacitance of 3DOM C in an electrolyte solution,[204] the electrodes developed here are especially vulnerable to this limitation of cyclic voltammetry. Various techniques have been developed that allow for elimination of capacitive currents.[1] Of these, square wave voltammetry (SWV) is an extremely attractive technique for determination of analytes with electrodes that have rather large capacitance.[1,231] SWV has been well characterized in the literature.[232-235] In addition, it has been used in recent attempts to detect explosive compounds,[236,237] including a study utilizing carbon fiber electrodes.[25] Square wave voltammetry was used here to investigate the response of the electrodes to DNT while eliminating the signal from the capacitance of the electrode, with the goal of obtaining a lower detection limit.

7.3.5 Optimization of SWV Parameters

When using square wave voltammetry, the optimal square wave (SW) pulse length must first be determined. To this extent, a solution of 1 mM DNT was interrogated with varying pulse lengths. As shown in Figure 59, the peak current observed for the reduction of DNT increased with increasing pulse length up to 500 ms, where the current began decreasing with subsequent increases in pulse length. This observation may be explained as follows: at rather short pulse length, the current observed is largely capacitive[238] while

at rather long lengths, the DNT contained in the pores of the 3DOM carbon is largely consumed and the current observed results solely from diffusion to the surface of the electrode. Consequently, a 500 ms pulse length was used for all subsequent experiments.

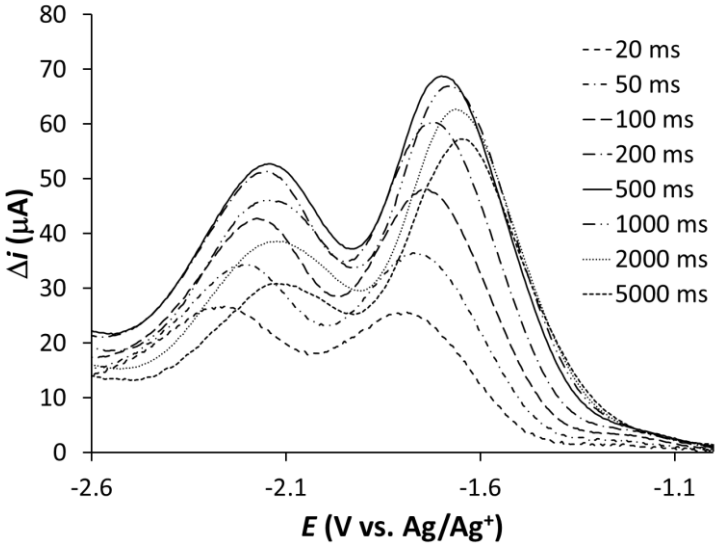

Figure 59: Square wave voltammograms of 1 mM DNT at a functionalized 3DOM carbon electrode in benzotrifluoride/100 mM NBu_4BArF_{24} with varied square wave pulse lengths (20–5000 ms). T = 20 °C, SW amplitude = 101 mV, potential step = 5 mV.

When using SWV, it is also necessary to determine the optimal SW amplitude. Shown in Figure 60 is the dependence of the peak current upon the SW amplitude.

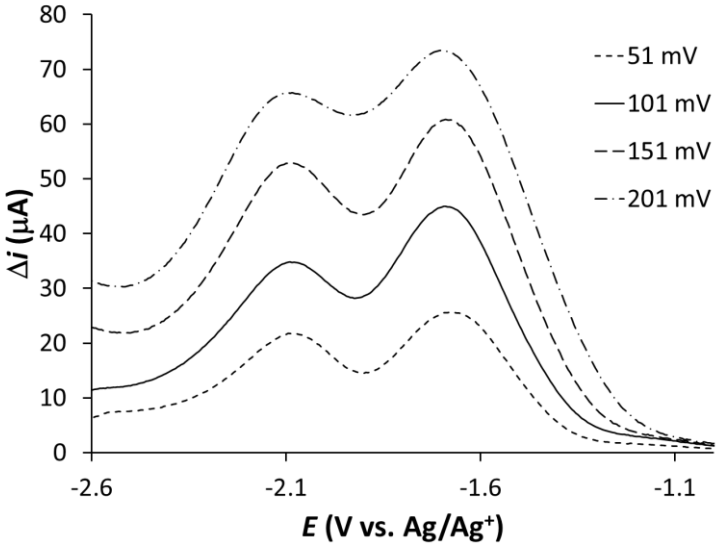

Figure 60: Square wave voltammograms of 1 mM DNT at a functionalized 3DOM carbon electrode in benzotrifluoride/100 mM NBu_4BArF_{24} with varied square wave amplitude (51–201 mV). T = 20 °C, SW pulse length = 500 ms, potential step = 5 mV.

As observed in Figure 60, the peak current for the reduction of DNT increased with increasing SW amplitude. Also, as the SW amplitude increased, there was a marked decrease in the resolution between the two reductions observed for DNT. These effects are consistent with the theory of SWV response.[231] While it may seem advantageous to choose an extremely large SW amplitude, the corresponding loss in resolution is undesirable for analytical applications. Therefore, an amplitude of 101 mV was chosen as a compromise between current sensitivity and resolution for all subsequent experiments.

7.3.6 Determination of Limit of Detection

The limit of detection for SWV was determined by addition of DNT. The relationship between the maximum current observed at –1750 mV and the concentration of DNT in solution is shown in Figure 61.

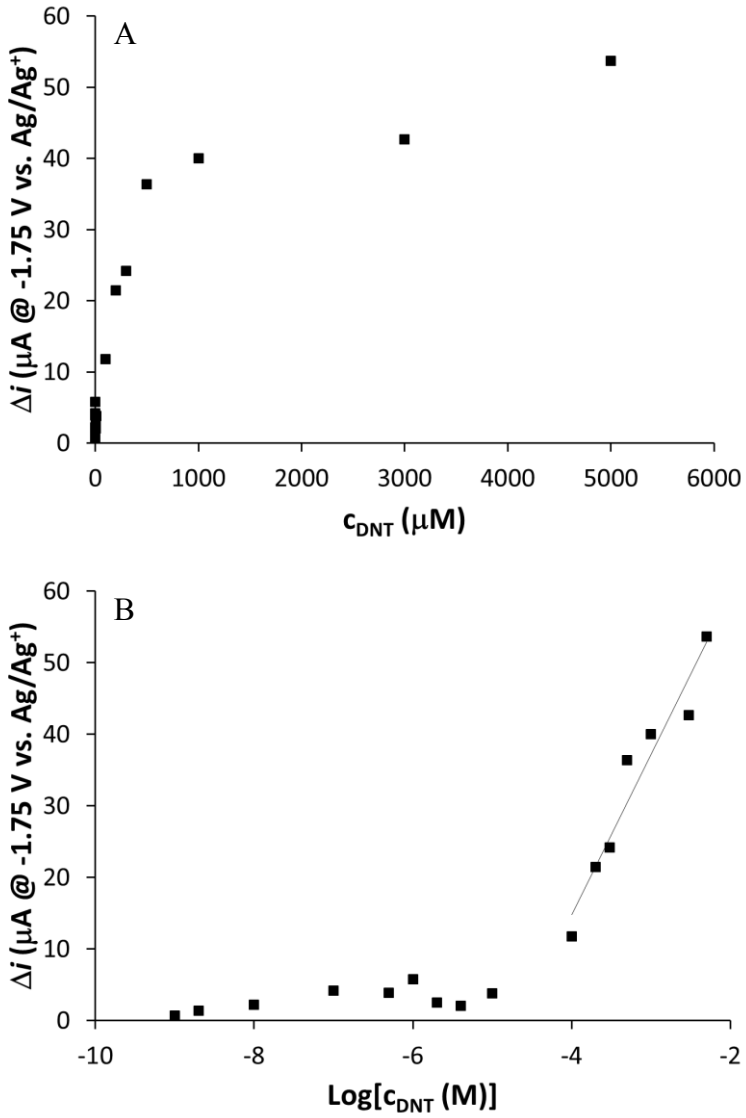

Figure 61: Dependence of the current observed by SWV at –1750 mV on (A) DNT concentration and (B) logarithm of DNT concentration at a functionalized 3DOM carbon electrode in benzotrifluoride/100 mM NBu_4BArF_{24}. T = 20 °C, SW pulse length = 500 ms, SW amplitude = 101 mV, potential step = 5 mV.

Inspection of the relationship between peak current and concentration observed in Figure 61 reveals that DNT may be adsorbed onto the surface of 3DOM C prior to

detection. As shown in Figure 61B, there is a linear relationship between the peak current and the logarithm of the DNT concentration above 10^{-4} M. This strongly suggests that *adsorbed* DNT is indeed being detected by SWV, as expected. A detection limit of 10 μM was obtained. This is comparable to a previously published detection limit of 5 μM for TNT in acetonitrile by SWV with a glassy carbon electrode.[24]

7.4 Conclusions

In this work, the pore walls of 3DOM carbon electrodes were successfully modified with DNT receptors. DNT was detected by cyclic voltammetry, but this requires a high concentration to give even a small peak due to the high surface area, and consequently large interfacial capacitance, of the 3DOM carbon electrode. To overcome this problem, square wave voltammetry was used, resulting in a detection limit of 10 μM for DNT. The linear response of the electrode when compared to the logarithm of the concentration of DNT indicates that receptor-bound DNT is being detected rather than DNT in solution. Moreover, the addition of receptor molecules to the surface of the 3DOM carbon electrodes provides selectivity for DNT over interferents such as nitrobenzene. These receptors were designed to take advantage of the slightly acidic nature of DNT while at the same time including hydrogen bond-donating sites to further stabilize the deprotonated DNT and thus increase the binding affinity for DNT.

8 CHAPTER EIGHT

Comparison of Reduction Potentials of Substituted Cations for Use in Electrochemical Capacitors

Electrochemical double layer capacitors, often referred to as supercapacitors, offer a promising route for low cost energy storage. The maximum working voltage of supercapacitors is limited by the accessible electrochemical window for the electrolyte used in the device. This work explores the relationship between the structure of the electrolyte cations and the cathodic limit. In the past, the electrochemical limits have been defined as the potentials at which a current density of an arbitrary value is achieved. This approach has led to ambiguity in the reported reduction potentials of cations from different literature sources. In this work, we propose a new method for defining the electrochemical limits for a solvent/electrolyte system. At applied potentials at which electrochemical consumption of the electrolyte occurs, mass transport of electrolyte to the electrode is dominated by migration and, consequently, the current increases proportionally to the applied potential. Our proposed method defines the electrochemical limit as the intercept of the linear portions of the current–voltage relationship at potentials above and below the onset of electrochemical electrolyte decomposition, as determined by linear sweep voltammetry. To demonstrate the advantages of the proposed method for the comparison of data obtained under experimentally diverse conditions, we investigated the reduction potentials for the tetramethyl-, tetrapropyl-, tetrabutyl-, and tetrahexylammonium electrolyte cations. The results show that with our new method the variation in reduction potential is less than 100 mV. On the other hand, using the traditional interpretation, the reduction limit for tetramethylammonium is 300 mV more negative than that for tetrahexylammonium, a difference that has nothing to do with the actual onset of reduction but is biased by the kinetics of ion migration thereafter.Moreover, we show that the reduction potential of a solution containing 75 mM tetrabutylammonium perchlorate as determined with the conventional method results in a cathodic limit 260 mV more negative than for a 600 mM solution of the same electrolyte. Using our proposed method, the concentration dependence of the reduction limit is nearly eliminated.

8.1 Introduction

When performing electrochemistry experiments involving the transfer of charge through a solution, specific care must be taken to choose solvent/electrolyte systems that are stable at the potentials that are interrogated.[1,2] The potential range in which a solvent/electrolyte system is stable is often referred to as the electrochemical window. Through use of organic solvents combined with lipophilic electrolytes such as the tetraalkylammonium salts of tetrafluoroborate, hexafluorophosphate, or perchlorate, electrochemical windows greater than 4 V are routinely achieved.[3] Such large potential windows are sufficient for most electrochemical experiments; however, electrochemical capacitor research has led to a large resurgence of interest in expanding the available electrochemical window further.[239-246]

Electrochemical double layer capacitors utilize the capacitance that every electrode–electrolyte boundary exhibits, which is dependent upon the material of which the electrode is constructed, the surface area of the electrode, and the size of the electrolyte ions.[1] In such devices, two large surface area electrodes are separated by either an electrolyte solution or an ionic liquid, much in the same way two plates are separated by a dielectric in a traditional plate capacitor.[245] Upon charging of the thus constructed capacitor, the electrolyte anions migrate toward and accumulate at the surface of the anode, while the cations approach the cathode.[243] Because of this mode of operation, there are two approaches to increasing the overall performance of the device: first, an increase of the capacitance of the electrode by increasing the number of ions that may approach the surface, and second, an increase in the bias potential to which the capacitor may be charged.[245,247] The number of ions that may approach the surface can be increased by either enlarging the surface area of the electrode or decreasing the ionic radius of the electrolyte ions, while the accessible bias potential may be increased by careful selection of the solvent and electrolyte. More specifically, the maximum bias potential that may be applied across the capacitor is the potential at which oxidation or reduction of the

electrolyte solution begins. If the applied potential consumes the electrolyte solution, the applied energy is irreveversibly lost rather than being stored.

In most cases, the anodic limit of the electrolyte is determined by electrochemical decomposition of the anion while the cathodic limit is determined by a reaction of the cation, although this is certainly not *always* the case (e.g., tetraphenylborate is reduced at a less negative potential than tetrabutylammonium).[3] Therefore, the process of selecting the most suitable electrolyte for these devices is often performed by analysis of the cathodic and anodic limits of the solvent/electrolyte system with a traditional three-electrode voltammetry setup.[248-250] In such experiments, a linear sweep voltammogram is taken until the end of the electrolyte window is observed. The definition of these limits is somewhat ambiguous, but is generally presented as the potential at which the current density, j, reaches a defined magnitude (often 0.5 or 1.0 mA/cm^2).[1,2]

With a view to increase the accessible cathodic potential for electrochemical capacitors, an extensive search of the literature was performed first to determine the best electrolyte–solvent systems described previously in the literature. The overview presented here comprises numerous noncyclic and cyclic ammonium, imidazolium, phosphonium, and bis(phosphine)iminium electrolytes but is limited to glassy carbon electrodes, due to catalytic effects that may arise at metal electrodes.[101,251] Second, the cathodic and anodic limits reported by various authors were compared with each other to illustrate the ambiguity of presenting these values as potentials observed at a rather large current. Lastly, a new method of defining these limits is presented and critically applied to several tetraalkylammonium electrolytes.

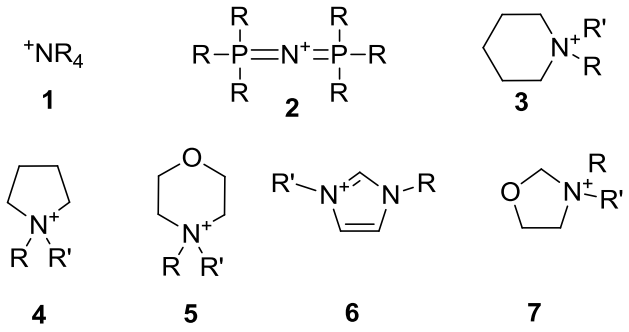

Figure 62: General structure of cations studied in this work. These cations fall in the following general categories: 1: ammonium, 2: bis(phosphine)iminium, 3: piperidinium, 4: pyrrolidinium, 5: morpholinium, 6: imidazolium, 7: oxazolidinium.

8.2 Experimental

All reagents were used as received without further purification unless otherwise noted. Anhydrous acetonitrile, anhydrous propylene carbonate, tetramethylammonium tetrafluoroborate, tetrapropylammonium bromide, tetrabutylammonium perchlorate, bis(triphenylphosphine)iminium chloride, tetraphenylphosphonium chloride, and tetrahexylammonium bromide were obtained from Sigma-Aldrich (St. Louis, MO). Tetrahydrofuran (Sigma-Aldrich) was distilled from Na/benzophenone under N_2 before use to remove trace water. The anhydrous solvents used in this work were stored and transferred under argon. All water was pre-deionized and further purified (≥18.2 MΩ cm specific resistance) with a Milli-Q PLUS reagent-grade water system (Millipore, Bedford, MA). Linear sweep and cyclic voltammetry experiments were carried out with a CHI600C Potentiostat (CH Instruments, Austin, TX). Sodium tetrakis[3,5-bis(trifluoromethyl)phenyl]borate was synthesized as described in Section 7.2.8. Tetramethylammonium tetrakis[3,5-bis(trifluoromethyl)phenyl]borate was prepared by metathesis from tetrapropylammonium bromide and sodium tetrakis[3,5-bis(trifluoromethyl)phenyl]borate, starting by distribution of equimolar amounts between 100 mL water and 100 mL diethyl ether. The organic phase was washed with water (3×20

mL), collected and dried with $MgSO_4$, followed by evaporation of the solvent with a rotary evaporator. The crude product was recrystallized from ethanol to give approximately 70% yield of the product as white crystals. It was characterized by ^{1}H NMR spectroscopy (500 MHz, $CDCl_3$, δ): 0.940 (t, J_{HH} = 7.4 Hz, CH_3, 12H), 1.57 (m, CH_2CH$_3$, 8H), 2.94 (m, NCH_2, 8H), 7.54 (s, *p*-Ar*H*, 4H), 7.68 (s, *o*-Ar*H*, 8H).

All electrochemical experiments were carried out with 300 mM solutions of the chosen electrolyte (with the exception of tetramethylammonium tetrafluoroborate, which is only soluble to 100 mM in propylene carbonate) using a three-electrode setup with a 3.0 mm-diameter glassy carbon (GC) disk working electrode (BAS, West Lafayette, IN), a 0.25 mm Pt wire coil (99.998%, Alfa Aesar, Ward Hill, MA) auxiliary electrode, and a Ag/(10 mM $AgNO_3$ + 100 mM NBu_4ClO_4) reference electrode (BAS). The working electrode was polished on Microcloth polishing pads using 5.0 μm Micropolish II deagglomerated alumina, both from Buehler (Lake Bluff, IL). After polishing, the electrode was rinsed thoroughly with deionized water and then ethanol, followed by drying under a stream of Ar. Prior to measurements, all solutions were purged with UHP argon for 15 min while stirring vigorously to remove dissolved oxygen. All potentials herein are with respect to Ag/10 mM Ag^+.

8.3 Results and discussion

8.3.1 Comparison of published cathodic limits

The electrochemical windows of 80 solvent–electrolyte systems are presented in Table 5.

Table 5: Table of reduction potentials reported in the literature

All potentials are relative to a Ag/10 mM Ag^+ in acetonitrile reference electrode. Abbreviations: PC: propylene carbonate, EC: ethylene carbonate, DMC: dimethyl carbonate, GC: glassy carbon

Cation	Anion	E_{red} (V)	E_{ox} (V)	Solvent	Electrode	Ref.
$((CH_3)_2CHCH_2)_3(CH_3)N^+$	PF_6^-	-4.25	2.91	Sat. in 1:1 EC:DMC	GC	243
$((CH_3)_2CH)_3(CH_3)N^+$	PF_6^-	-4.15	2.75	Sat. in 1:1 EC:DMC	GC	243
$(CH_3CH_2CH_2)_3(CH_3)N^+$	PF_6^-	-3.97	2.81	Sat. in 1:1 EC:DMC	GC	243
$(CH_3CH_2)_4N^+$	NbF_6^-	-3.9	2.8	650 mM in PC	GC	239
$(CH_3CH_2)_4N^+$	$B(C_6H_5)_4^-$	-3.9	0.2	650 mM in PC	GC	239
$(CH_3CH_2CH_2CH_2)_3(CH_3)N^+$	PF_6^-	-3.86	2.89	Sat. in 1:1 EC:DMC	GC	243
$(CH_3CH_2)_4N^+$	AsF_6^-	-3.8	3.0	650 mM in PC	GC	239
$(CH_3CH_2)_4N^+$	$C_4F_9SO_3^-$	-3.8	2.5	650 mM in PC	GC	239
$(CH_3CH_2)_4N^+$	$(CF_3SO_2)_2N^-$	-3.8	2.5	650 mM in PC	GC	239
$(CH_3CH_2)_4N^+$	ClO_4^-	-3.8	2.3	650 mM in PC	GC	239
$(CH_3CH_2)_4N^+$	$CF_3SO_3^-$	-3.8	2.2	650 mM in PC	GC	239
$(CH_3CH_2)_4N^+$	SbF_6^-	-3.7	3.3	650 mM in PC	GC	239
$(CH_3CH_2)_4N^+$	PF_6^-	-3.7	3.0	650 mM in PC	GC	239
$(CH_3CH_2)_4N^+$	BF_4^-	-3.7	2.8	650 mM in PC	GC	239
$(CH_3CH_2)_4N^+$	BF_4^-	-3.70	2.45	Sat. in 1:1 EC:DMC	GC	243
$(CH_3CH_2)_4N^+$	PF_6^-	-3.68	2.92	Sat. in 1:1 EC:DMC	GC	243
$(CH_3CH_2)_3(CH_3)N^+$	BF_4^-	-3.67	2.48	Sat. in 1:1 EC:DMC	GC	243

Cation	Anion	E_{red} (V)	E_{ox} (V)	Solvent	Electrode	Ref.
$(CH_3CH_2)_4N^+$	$CF_3SO_3^-$	-3.67	1.57	Sat. in 1:1 EC:DMC	GC	243
$(CH_3CH_2)_4N^+$	$(CF_3SO_2)_2N^-$	-3.66	1.83	Sat. in 1:1 EC:DMC	GC	243
$(CH_3CH_2)_4N^+$	AsF_6^-	-3.65	2.89	Sat. in 1:1 EC:DMC	GC	243
$(CH_3CH_2)_3(CH_3)N^+$	AsF_6^-	-3.65	2.74	Sat. in 1:1 EC:DMC	GC	243
$(CH_3CH_2)_3(CH_3)N^+$	$CF_3SO_3^-$	-3.65	1.45	Sat. in 1:1 EC:DMC	GC	243
$(CH_3CH_2)_3(CH_3)N^+$	$(CF_3SO_2)_2N^-$	-3.63	1.17	Sat. in 1:1 EC:DMC	GC	243
$(CH_3CH_2)_3(CH_3)N^+$	PF_6^-	-3.60	2.94	Sat. in 1:1 EC:DMC	GC	243
$((CH_3)_2CH)_2(CH_3CH_2)(CH_3)N^+$	PF_6^-	-3.60	2.83	Sat. in 1:1 EC:DMC	GC	243
$(CH_3CH_2CH_2CH_2)_3(CH_3)P^+$	PF_6^-	-3.56	2.97	Sat. in 1:1 EC:DMC	GC	243
$(CH_3CH_2)_3(CH_3)N^+$	PF_6^-	-3.45	2.90	Sat. in 1:1 EC:DMC	GC	243
$(CH_3CH_2)(CH_3)_3N^+$	PF_6^-	-3.40	2.80	Sat. in 1:1 EC:DMC	GC	243
$(CH_3CH_2)_4N^+$	BF_4^-	-3.36	3.24	1 M in PC	GC	240
$(CH_3CH_2)_4N^+$	PF_6^-	-3.36	3.24	1 M in PC	GC	240
$(CH_3CH_2)_4N^+$	$CF_3SO_3^-$	-3.36	3.24	1 M in PC	GC	240
$(CH_3CH_2)_4N^+$	ClO_4^-	-3.36	2.74	1 M in PC	GC	240
$(C_2H_5)_3(CH_3OCH_2CH_2)N^+$	$(CF_3SO_2)_2N^-$	-3.36	2.37	Neat	GC	252
$(CH_3)(C_2H_5)_2(C_4H_9)N^+$	$(CF_3SO_2)_2N^-$	-3.36	2.33	Neat	GC	252
$(CH_3)(C_2H_5)_2(CH_3OCH_2CH_2)N^+$	n-$C_4F_9BF_3^-$	-3.36	2.29	Neat	GC	252
$(CH_3)(C_2H_5)_2(C_4H_9)N^+$	$CF_3BF_3^-$	-3.35	2.40	Neat	GC	252
$(CH_3)(C_2H_5)_2(C_4H_9)N^+$	$C_2F_5BF_3^-$	-3.35	2.29	Neat	GC	252

Cation	Anion	E_{red} (V)	E_{ox} (V)	Solvent	Electrode	Ref.
$(C_2H_5)_3(CH_3OCH_2CH_2)N^+$	$CF_3BF_3^-$	-3.33	2.37	Neat	GC	252
N-methyl-*N*-butylpyrrolidinium	$C_2F_5BF_3^-$	-3.33	2.32	Neat	GC	253
$(C_2H_5)_3(CH_3OCH_2CH_2)N^+$	$C_2F_5BF_3^-$	-3.33	2.30	Neat	GC	252
$(CH_3)(C_2H_5)_2(CH_3OCH_2CH_2)N^+$	BF_4^-	-3.32	2.32	Neat	GC	252
$(CH_3)(C_2H_5)_2(CH_3OCH_2CH_2)N^+$	$CF_3BF_3^-$	-3.30	2.40	Neat	GC	252
$(CH_3CH_2)_4N^+$	$B(C_6F_5)_4^-$	-3.3	1.4	650 mM in PC	GC	239
N-butyl-*N*-methylpiperidinium	$C_2F_5BF_3^-$	-3.29	2.23	Neat	GC	253
$(C_4H_9)(CH_3)_3N^+$	$(CF_3SO_2)_2N^-$	-3.27	2.58	Neat	GC	252
$(CH_3)(C_2H_5)_2(CH_3OCH_2CH_2)N^+$	$(CF_3SO_2)_2N^-$	-3.25	2.42	Neat	GC	252
$(CH_3)(C_2H_5)_2(CH_3OCH_2CH_2)N^+$	n-$C_3F_7BF_3^-$	-3.25	2.36	Neat	GC	252
$(CH_3)(C_2H_5)_2(CH_3OCH_2CH_2)N^+$	$C_2F_5BF_3^-$	-3.24	2.37	Neat	GC	252
N-butyl-*N*-methyloxazolidinium	$C_2F_5BF_3^-$	-3.20	2.34	Neat	GC	253
N-methyl-*N*-propylpyrrolidinium	$(CF_3SO_2)_2N^-$	-3.07	2.57	Neat	GC	254
N-methyl-*N*-propylpyrrolidinium	$(CF_3SO_2)_2N^-$	-3.07	2.57	Neat	GC	255
$(CH_3)_2(C_2H_5)(CH_3OCH_2CH_2)N^+$	$(CF_3SO_2)_2N^-$	-3.05	2.43	Neat	GC	252
N-allyl-*N*-ethylmorpholinium	$(CF_3SO_2)_2N^-$	-3.04	2.34	Neat	GC	254
N-allyl-*N*-methylpyrrolidinium	$(CF_3SO_2)_2N^-$	-3.01	2.54	Neat	GC	254
N-2-hydroxyethyl-*N*-methylpyrrolidinium	$(CF_3SO_2)_2N^-$	-2.99	2.49	Neat	GC	255
N-ethyl-*N*-3-hydroxypropylpiperidinium	$(CF_3SO_2)_2N^-$	-2.96	2.49	Neat	GC	255
N-methoxymethyl-*N*-methylpyrrolidinium	$C_2F_5BF_3^-$	-2.95	2.32	Neat	GC	253

Cation	Anion	E_{red} (V)	E_{ox} (V)	Solvent	Electrode	Ref.
N-methyl-*N*-3-hydroxypropylpyrrolidinium	$(CF_3SO_2)_2N^-$	-2.92	2.54	Neat	GC	255
N-allyl-*N*-methylpiperidinium	$(CF_3SO_2)_2N^-$	-2.92	2.40	Neat	GC	254
N-allyl-*N*-ethylpiperidinium	$(CF_3SO_2)_2N^-$	-2.92	2.40	Neat	GC	254
N-methyl-*N*-methoxyethyl pyrrolidinium	$C_2F_5BF_3^-$	-2.91	2.32	Neat	GC	253
N-allyl-*N*-methylmorpholinium	$(CF_3SO_2)_2N^-$	-2.87	2.35	Neat	GC	254
$(CH_3)_2(C_2H_5)(CH_3OCH_2CH_2)N^+$	$CF_3BF_3^-$	-2.87	2.29	Neat	GC	252
N-2-hydroxyethyl-*N*-ethylpiperidinium	$(CF_3SO_2)_2N^-$	-2.86	2.58	Neat	GC	255
N-2-hydroxyethyl-*N*-methylpiperidinium	$(CF_3SO_2)_2N^-$	-2.86	2.50	Neat	GC	255
N-methyl-*N*-3-hydroxypropylpiperidinium	$(CF_3SO_2)_2N^-$	-2.85	2.57	Neat	GC	255
N-methyl-*N*-methoxyethyl piperidinium	$C_2F_5BF_3^-$	-2.77	2.34	Neat	GC	253
N-2-methoxyethyl-*N*-methylpiperidinium	$(CF_3SO_2)_2N^-$	-2.75	2.55	Neat	GC	255
N-2-methoxyethyl-*N*-methylpyrrolidinium	$(CF_3SO_2)_2N^-$	-2.73	2.55	Neat	GC	255
$(CH_3)_3(CH_3OCH_2CH_2)N^+$	n-$C_3F_7BF_3^-$	-2.67	2.32	Neat	GC	252
$(CH_3)_3(CH_3OCH_2CH_2)N^+$	$(CF_3SO_2)_2N^-$	-2.63	2.44	Neat	GC	252
N-butyl-*N*-methyl morpholinium	$C_2F_5BF_3^-$	-2.54	2.45	Neat	GC	253
bis(triphenylphosphine)iminium	Br^-	-2.47	0.64	650 mM in PC	GC	*a*
1-ethyl-3-methylimidazolium	$C_2F_5BF_3^-$	-2.42	2.23	Neat	GC	253
1-ethyl-3-methylimidazolium	$CF_3BF_3^-$	-2.41	2.22	Neat	GC	252
N-methyl-*N*-methoxyethyloxazolidinium	$C_2F_5BF_3^-$	-2.30	2.35	Neat	GC	253
$(CH_3CH_2)_4N^+$	$BCH_3(C_2H_5)_3^-$	-2.2	1.4	650 mM in PC	GC	239

Cation	Anion	E_{red} (V)	E_{ox} (V)	Solvent	Electrode	Ref.
$(CH_3CH_2)_4N^+$	$B(C_2H_5)_4^-$	-2.1	1.3	650 mM in PC	GC	239
$(CH_3CH_2)_4N^+$	$B(C_4H_9)_4^-$	-2.1	1.3	650 mM in PC	GC	239
N-methyl-*N*-methoxyethylmorpholinium	$C_2F_5BF_3^-$	-2.06	2.42	Neat	GC	253

[a] *This* work.

Upon first inspection, it is clear that tetraalkylammonium and tetraalkylphosphonium cations exhibit a much higher stability toward reductive decomposition than the remainder of the cations listed. To gain a more quantitative understanding of the effect of substitution around the cationic center, the reduction potentials of the cations were plotted against the number of heavy atoms around each cationic center (that is, the total number of carbons, nitrogens, and oxygens covalently linked to the ionic center of the molecule; see Figure 63).

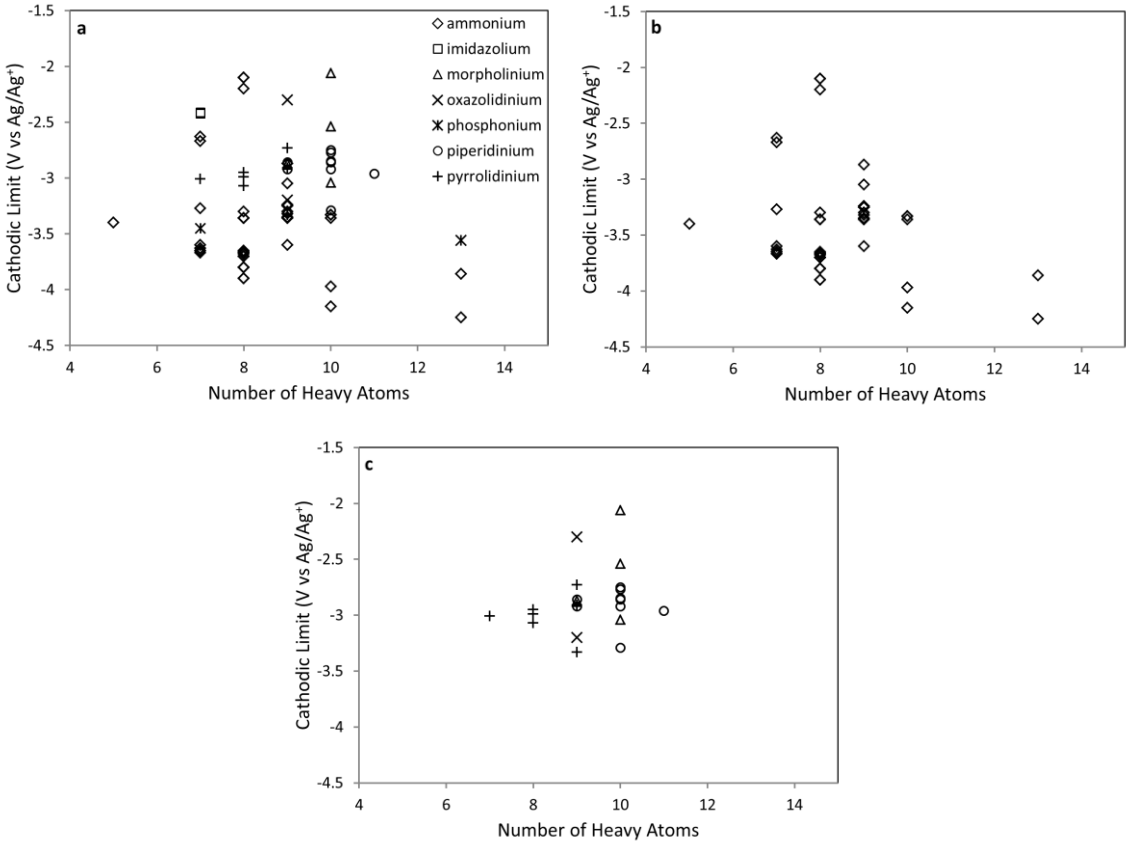

Figure 63: Plot of the cathodic limit with respect to the number of heavy atoms around the cation center for various classes of cations. Panel (a) contains all of the cathodic limits determined from the published sources listed in Table 5. For additional clarity,

Panel (b) is limited only to tetraalkylammonium cations and Panel (c) is limited to cyclic ammonium cations of the type 3, 4, 5, and 7 (see Figure 62).

Initial inspection of Figure 63 reveals that there is a loose correlation between the number of heavy atoms around the cation center and the observed cathodic limit. This dependence is especially pronounced in the larger tetraalkylammonium cations, which indicates that the more bulky ions are preferable when trying to access a large potential. Also, there are several ammonium salts that exhibit reduction potentials higher than –3.0 V. In these instances, the anion of choice is reduced at a less negative potential than the cation,[239,252] thus highlighting the significance of carefully selecting the anion used when studying the reduction potential of cations.

The introduction of a cyclic substituent to the central nitrogen of quaternary ammonium cations of the type **3, 4, 5,** and **7** clearly reduces the accessible cathodic limit. Based upon the observed cathodic limits for acyclic ammonium cations, the steric hindrance about the cation center appears to greatly influence how readily the cation is reduced. Therefore, it is likely that the loss in steric hindrance associated with introduction of a cyclic structure allows the cation centers to more closely approach the electrode and therefore be reduced. Surprisingly, there does not seem to be any observable correlation between the size of the ring and the cathodic limit of the electrolyte. Lastly, the introduction of aromatic systems that are covalently bound to the ionic center (see, e.g., the imidazolium cations, **6**) is clearly not desirable for accessing large electrochemical windows.

An additional conclusion that can be drawn from the data shown Figure 63 is that there is a wide spread of cathodic limits for ions that contain the same number of heavy atoms. In some cases, this effect is a result of variation in the overall bulkiness of the alkyl substituent (i.e., using an isobutyl rather than *n*-butyl substituent). However, there is also a rather large range of reported cathodic limits for individual cations. The most notable example of discrepancies for the same cation with differing salts is the case of

tetraethylammonium. In three studies from two different authors,[239,240,243] the cathodic limits for use of the tetraethylammonium cation ranges from –3.9 to –3.3 V vs. Ag/Ag^+. The spread of these literature results limits the more detailed interpretation of the effect of different substitution patterns and highlights the need for care when comparing the cathodic limits for cations as they are currently presented in the literature.

8.3.2 Measurement of reduction potentials for various cations

To better understand the effect of substituents upon the reduction of alkylammonium cations, the cathodic limits of the analogous series of tetramethyl-, tetrapropyl-, tetrabutyl-, and tetrahexylammonium cations were measured in this study using as the solvent propylene carbonate, which is commonly employed in electrochemical capacitors due to its ability to dissolve large concentrations of organic electrolyte along with its electrochemical stability.[241] Linear sweep voltammograms for these four cations are shown in Figure 64.

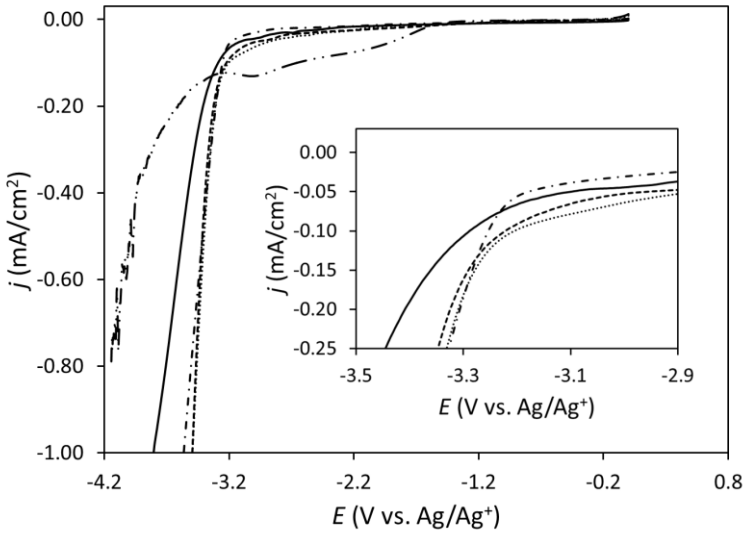

Figure 64: Linear sweep voltammograms showing the cathodic electrochemical limit of tetramethylammonium tetrafluoroborate (100 mM, solid), tetrapropylammonium bromide (300 mM, dashed), tetrabutylammonium perchlorate (300 mM, dot-dashed),

tetrahexylammonium bromide (300 mM, dotted), and sodium hexafluorophosphate (saturated, dot-dot-dashed) in propylene carbonate. Working electrode: glassy carbon, reference: Ag/10 mM $AgNO_3$, auxiliary: Pt coil. T = 21 °C.

Based upon a limiting current density, j, of 1.0 mA/cm^2, a criterion often used to define the electrochemical window, the cathodic limits for tetramethylammonium, tetrapropylammonium, tetrabutylammonium, and tetrahexylammonium are –3.80, –3.50, –3.56, and –3.50 V vs. Ag/Ag$^+$, respectively. To verify that the *solvent* was not the source of the cathodic limit, a linear sweep voltammogram of a saturated solution of sodium hexafluorophosphate in propylene carbonate was also measured (see Figure 64). In this voltammogram, significant current is observed between –2.0 and –3.0 V vs Ag/Ag$^+$, which is a result of reduction of the water introduced to the solution due to the hygroscopic nature of sodium hexafluorophosphate.[248] More importantly, a stable signal at a current density of 1 mA/cm^2 could not be achieved as the decomposition of propylene carbonate results in the formation of gas bubbles at the working electrode.[256] Consequently, the reduction potential for this system (as determined by the traditional method) cannot be reported. Despite this, the figure clearly shows that the cathodic limits observed for the tetraalkylammonium salts tested herein are due to the electrolyte rather than the solvent itself.

By defining the electrochemical limits as the potentials at which a fixed current density is achieved, these limits are dependent upon the rate at which the species that is the source of the limit is transported to the electrode. In any electrochemical system, analyte is carried to the electrode by three processes: convection, diffusion, and migration.[1] Since the solutions used in these experiments are unstirred, convection is assumed to be negligible. Therefore, the total measured current, i, is the sum of the diffusion (i_d) and migration (i_m) components. For a system with a cross-section area A, the current, i, carried by migration of an ion is determined by

$$i = \frac{z^2 F^2 ADC}{RT} \times \frac{\partial \phi}{\partial x} \tag{1}$$

where z is the charge of the ion, F is Faraday's constant, D is the diffusion coefficient of the ion, C is the concentration of the ion, R is the ideal gas constant, T is the solution temperature and $\partial\phi/\partial x$ is the potential gradient across the cell. The mobility of an ion, u, in an electric field is given by the Einstein-Smoluchowski equation,

$$u = \frac{|z|FD}{RT} \tag{2}$$

Inserting Equation 3 into Equation 2 gives the current carried by an individual ionic species, as

$$i = |z|FAuC \times \frac{\partial \phi}{\partial x} \tag{3}$$

As shown by Equation 3, the current carried by an ion through a solution is proportional to the potential applied to this solution. Because at large potentials migration is considerably faster than diffusion, the diffusion component may be ignored after the initial rise in current. Indeed, the current densities in Figure 64 are proportional to the applied potential when significant reduction of the cation is observed, as apparent from the linear dependence of the current density on the applied potential.

Close inspection of the potential range in which the *onset* of cation reduction begins to occur (inset, Figure 64) reveals that these ions all begin to show reductive current at approximately the same potential. This indicates that, despite the cathodic limits being very different, the true reduction potential of all tested cations are equivalent. The differences in cathodic limit are thus likely a reflection of differences in mobility. Moreover, tetramethylammonium tetrafluoroborate is present in a significantly lower concentration than the other three electrolytes tested due to its limited solubility. Because the limits of the electrochemical window are sensitive to differences in concentration as well as ion mobility, we propose the following alternative method for defining these limits:

1) Measure a linear sweep voltammogram in the potential range of interest.
2) Perform a linear regression analysis of the linear portions of the current–voltage relationship before and after the onset of oxidation/reduction of the electrolyte.
3) From the best fit equations produced by linear regression, determine the potential at which the two linear portions of the voltammogram intersect. This potential will be defined as the limiting potential for this system.

By applying this method to the data shown in Figure 3, cathodic limits of –3.35, –3.31, –3.26, –3.31, and –3.65 V vs. Ag/Ag^+ for tetramethylammonium, tetrapropylammonium, tetrabutylammonium, tetrahexylammonium, and sodium, respectively, were determined. By extrapolating the linear portions of the current both before and after the onset of the reduction of the cation, the observed effect of ion mobility is minimized.

For additional verification of the usefulness of this method, the cathodic limit was measured for solutions containing 75, 150, 300, and 600 mM tetrabutylammonium perchlorate. The resulting linear sweep voltammograms are shown in Figure 65.

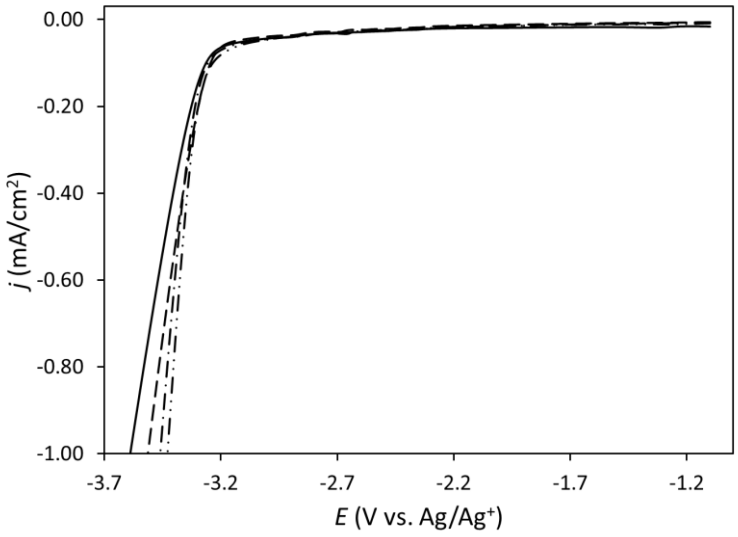

Figure 65: Linear sweep voltammograms to show the cathodic limits for 75 (solid), 150 (dashed), 300 (dot-dashed), and 600 (dot-dot-dashed) mM tetrabutylammonium perchlorate solutions in propylene carbonate. Working electrode: glassy carbon, reference: Ag/10 mM $AgNO_3$, auxiliary: Pt coil. T = 21 °C.

Treatment of the data shown in Figure 65 using the traditional definition of the electrochemical limits results in cathodic limits of –3.59, –3.51, –3.46, and –3.33 V for 75, 150, 300, and 600 mM tetrabutylammonium perchlorate, respectively. Clearly, the cathodic limit is highly biased toward the solution with lower electrolyte concentration. Alternatively, using our proposed method for defining the limits results in cathodic limits of –3.29, –3.27, –3.31, and –3.31 V for these concentrations.

8.4 Conclusions

Increasing the potential range that is accessible for electrolyte solutions is of utmost importance for improving the performance of electrochemical capacitors. Compilation of reduction potentials for various organic ions revealed that tetraalkylammonium cations are very resistant to electrochemical reduction. A loose correlation between the reduction potential of these ions and the overall bulkiness of the alkyl substituents was observed, suggesting that increasing the overall size and steric hindrance of the cation will further increase the potential range that may be accessed. However, the cathodic limits reported in the literature for individual cations vary in a wide range, suggesting that the common method of determining these potentials is unreliable due to the variability in solution resistance and cation mobility for different electrolyte systems.

We propose a new method for reporting the electrochemical limits of a solvent/electrolyte system. It involves performing linear regression in the two linear ranges of a linear sweep voltammogram, and thereby resembles the similar definition of the detection limit of ion-selective electrodes, as recommended by IUPAC.[257,258] The new method is much less sensitive to variations in ion mobility than the traditional method of assigning the limit as the potential at which an arbitrary current density is observed. Because accurate reporting of electrochemical windows is of great importance for both the development of electrochemical capacitors[245] and more traditional electroanalytical experiments,[244,249,259] the use of this method to re-examine previously reported electrochemical windows may be warranted. Moreover, further expansion of accessible

reduction potentials by employing sterically hindered cations (such as tetra-*t*-butyl-, tetraisobutyl-, and tetraisopropylammonium) is suggested by this work and will be carried out in the future.

9 CHAPTER NINE

Conclusions and Research Outlook

9.1 Summary of Results

The driving goal behind this work was the eventual development of a fluorous matrix-based sensor for 2,4-dinitrotoluene. The sensing of DNT is of importance for military, homeland security, and environmental remediation applications. Because the construction of a sensing device is a large undertaking, the work was broken down into smaller goals. The results of this work and its impact on development of a sensor for DNT are summarized below.

Because the ultimate goal of this work was to develop a sensor that utilizes a fluorous sensing matrix, we first developed a method for performing electrochemistry with a fluorous solvent. This work is presented in Chapter 2. By pairing the fluorophilic tetrakis[3,5-bis(perfluorohexyl)phenyl]borate with tetrabutylammonium, a viscous ionic liquid that is miscible with perfluoro(methylcyclohexane) is produced. At an electrolyte concentration of 80 mM, the specific solution resistance is reduced to 268 kΩ cm. This resistance is sufficiently low to allow for voltammetry in the fluorous phase. Quantitative fitting of the CVs for ferrocene revealed a standard rate transfer constant (k^o) that is substantially lower than in solvents typically used for cyclic voltammetry. This result is readily explained using Marcus Theory as a result of the size of the solvent molecule and the viscosity of the solution.

Because the electrolyte described in Chapter 2 is not commercially available, it became clear while performing this work that development of a cell for performing voltammetry with small volumes was necessary. Chapter 3 summarizes the construction and characterization of the small cell that was subsequently developed. Unlike previously published cells for small-volume electrochemistry, this cell is readily disassembled for cleaning and allows for use of different electrode materials. Moreover, this cell allows for routine electrochemistry in samples as small as 200 μL without deviation from ideal behavior.

Chapter 4 then explores the interaction of DNT with several alkylamines. The interaction of DNT with amines in DMSO gives rise to an intensely blue-colored

complex. In the past, this colored compound had been interpreted as so-called "Meisenheimer" complexes. Investigation of this interaction by ^{1}H NMR spectroscopy revealed that there was very little change in the spectrum for DNT upon the addition of an amine, contrary to expectation for a stable Meisenheimer complex. Principle component analysis of UV-Vis spectra for several DNT–amine solutions reveals that only one absorbing species of significant concentration is formed. Quantitative fitting of Job's plots for the DNT–amine system revealed that a 1:1 association complex cannot explain the colored species. Instead, fitting to a deprotonation reaction reveals extremely accurate fits for the system. This work reveals that care must be taken when interpreting the colored compounds observed for the interactions between nitroaromatic compounds and nucleophilic bases.

While performing the work in Chapter 4, it became clear that while a great deal of theory has been developed for interpreting the reactant stoichiometry of a Job plot, very little to interpret the products has been presented in the literature. In Chapter 5, the effect of product stoichiometry is explored for Job plots of systems with a 1:1 reactant ratio. We have developed a method for interpreting Job plots that may accurately distinguish between 1:1 association, 2:2 association, and displacement type equilibria. This method allows for the interpretation of molecular interactions at a level that could only otherwise be achieved with additional laborious experiments.

Chapter 6 investigates the electrochemical reduction characteristics of DNT. In anhydrous acetonitrile, DNT exhibits two largely reversible one-reduction transfers. While DNT is being reduced at the working electrode, an intense blue color is observed emanating from the working electrode. To confirm the origin of this blue color, bulk electrolysis of DNT was performed. While the product of this hydrolysis could not be isolated and purified, the UV-Vis absorption spectrum of the compound is indistinguishable from that of deprotonated DNT in acetonitrile. This strongly suggests that the DNT radical anion is sufficiently basic to deprotonate unreacted DNT in solution. Moreover, the protonated DNT radical anion undergoes further reduction, making the

CVs of DNT in anhydrous solution extremely complicated. Performing voltammetry with pH buffered acetonitrile solutions revealed that with a sufficiently concentrated source of protons, DNT is reduced to 2,4-(*N*-hydroxylamino)toluene in an eight-proton, eight-electron reduction.

Using the knowledge gained in Chapters 4 and 6, a receptor molecule for DNT was developed and covalently bonded to the surface of a three-dimensionally ordered macroporous carbon electrode. Using cyclic voltammetry, these electrodes were shown to exhibit enhanced sensitivity to DNT when compared to unmodified 3DOM carbon electrodes in benzotrifluoride. Moreover, the electrodes were also shown to be selective to DNT over phenol and nitrobenzene. Using square wave voltammetry to reduce the effect of the large capacitance of 3DOM carbon, a detection limit of 10 μM was obtained for DNT. This limit of detection is comparable to previously reported electrochemical DNT sensors but, due to the receptor molecules covalently linked to the electrode, selectivity over similar molecules is exhibited.

Lastly, a departure from detection of DNT is made in Chapter 8, where the effect of substituent structure on the electrochemical reduction potential of cations was explored. This work was intended to increase the accessible potential for supercapacitors; however, increasing the understanding of cation substituents in voltammetry experiments may aid in further development of electrolytes for performing electrochemistry with nonpolar solvents. We also suggest a new method for reporting the cathodic limit of solvent/electrolyte systems that is much less sensitive to the concentration and mobility of the anion of interested than the conventional method.

9.2 Future Work

As mentioned, the ultimate goal that has driven this research is the development of a fluorous matrix-based electrochemical sensor for DNT. Utilization of a fluorous matrix is desirable due to the extremely large increase in complex stability in fluorous solvents when compared to traditional organic solutions.[49,55] The sensor described in Chapter 8

utilizes the solvent benzotrifluoride, a common solvent used for bridging the gap between traditional organic and fluorous solvents.[52] Indeed benzotrifluoride is sufficiently nonpolar as to not occupy the receptor covalently linked to the 3DOM carbon electrode as was observed for more polar solvents such as acetonitrile.

While significant advances toward a fluorous matrix-based sensor have been made, there is still a significant amount of research to be performed. First and foremost, currently available electrolytes are incapable of sufficiently lowering the resistance of a fluorous solvent to allow voltammetry with an electrode larger than tens of micrometers in diameter. Clearly, a new fluorophilic electrolyte is required to lower the resistance sufficiently for electrochemistry with a larger chemically modified electrode. A possible solution to the high resistance of the fluorous solution may be to utilize a highly fluorinated ionic liquid as a solvent rather than an electrolyte in fluorous solution. Since the fluorophilic electrolyte used in Chapter 2 is already a viscous ionic liquid, it seems likely that minor modifications to the structure of this electrolyte may greatly decrease the viscosity. Current literature has shown that asymmetry and steric bulkiness in the alkyl substituents of the ionic components of an electrolyte decrease the melting point of the electrolyte.[260] Indeed, current research in the Bühlmann research group is endeavoring to produce a heavily fluorinated cation based on the structure $R_3P{=}N^+{=}PR'_3$. By variation of the alkyl moieties on these cations, their ability to pack with the currently available fluorophilic borate and therefore their melting points may be varied.

Alternatively, introducing asymmetry into a fluorophilic anion will also likely decrease the melting point of such fluorophilic electrolytes. Currently, synthesis of the fluorophilic borate utilized in Chapter 2 is performed by lithiation of four equivalents of 1-bromo-3,5-bis(perfluorohexyl)benzene followed by addition of one equivalent boron trichloride. As an alternative, three equivalents of 1-bromo-3,5-bis(perfluorohexyl)-benzene may be reacted with one equivalent of dichlorophenylborane (commercially available) according to the following scheme.

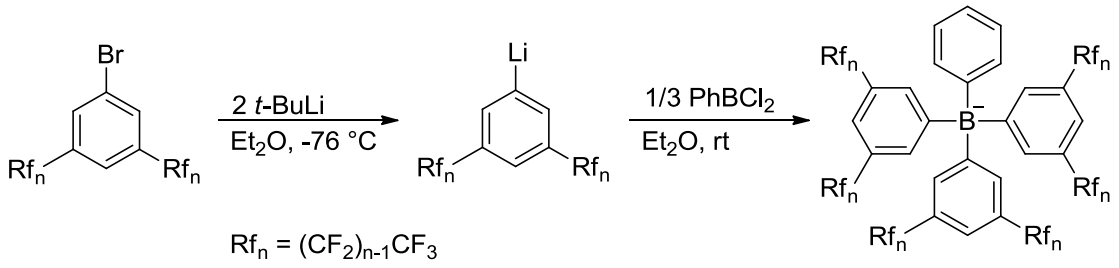

Figure 66: Suggested synthetic scheme for an asymmetric fluorophilic tetraphenylborate.

Should this synthetic scheme prove successful, the next logical step is to synthesize 3,5-bis(trifluoromethyl)phenyldichloroborane by following the synthetic scheme presented by Haubold and coworkers for synthesizing dichlorophenylborane.[261] Should an asymmetric borate be synthesized, the melting point of its salt with tetrabutylammonium is likely to be considerably lower than that of the symmetric compound.

Second, further exploration of the effects of alkyl substituents on ammonium cations will likely increase the potential range accessible for supercapacitors. The next logical step for research in this area is to begin synthesizing highly sterically hindered tetraisopropyl-, tetraisobutyl-, and tetra-*t*-butylammoniums cations for use in these systems. While very little variation of the cathodic limit was observed for an analogous series of tetra-*n*-alkylammoniums, the increased steric hindrance about the nitrogen center of the branched alkanes is more likely to shield the nitrogen from the electrode surface and therefore expand the cathodic limit of the electrolyte.

Third, the differences observed for the electrochemical reduction of DNT in pH-buffered organic and aqueous solutions are very difficult to reconcile experimentally. Therefore, computational modeling of this system is required to propose a more detailed mechanism for the reduction of DNT. Calculating the reduction potentials and pKa values for the intermediates formed during the electrochemical reduction of DNT will allow for detailed modeling of this system. While absolute reduction potentials are difficult to determine computationally due to solvation effects, computational modeling will allow for determination of these parameters *relative* to the other intermediates in the

reduction pathway. Moreover, gaining insight into the intermediates encountered during the reduction of DNT may allow for more intelligent design and implementation of electrochemical sensors for DNT. This modeling is already underway in collaboration with the Cramer research group.

Lastly, the development of fluorophilic electrolytes will open additional avenues for other modes of electrochemistry with fluorous phases. A great deal of work has been performed in the Bühlmann group in developing fluorous-matrix based ion selective electrodes.[50,53,54,95] These electrodes exhibit extremely large membrane resistances, requiring the use of extremely high input impedance potentiometers along with Faraday cages to reduce electronic noise. The suggested ions for fluorophilic electrolytes will also serve as new ionic sites for these sensing devices.

References

(1) Bard, A. J.; Faulkner, L. R. *Electrochemical Methods: Fundamentals and Applications*; 2nd ed.; Wiley: New York, 2001.

(2) Sawyer, D. T.; Sobkowiak, A.; Roberts, J. L. *Electrochemistry for Chemists*; 2nd ed.; Wiley: New York, 1995.

(3) Aurbach, D. *Nonaqueous Electrochemistry*; Marcel Dekker: New York, 1999.

(4) Connors, K. A. *Binding Constants: The Measurement of Molecular Complex Stability*; John Wiley & Sons: New York, 1987.

(5) Yinon, J. *Anal. Chem.* **2003**, 75, 99A-105A.

(6) Steinfield, J. I.; Wormhoudt, J. *Annu. Rev. Phys. Chem.* **1998**, 49, 203-232.

(7) Urbański, T. *Chemistry and Technology of Explosives*; Macmillan: New York, 1964; Vol. 1.

(8) Zang, J.; Guo, C. X.; Hu, F.; Yu, L.; Li, C. M. *Anal. Chim. Acta* **2011**, 683, 187-191.

(9) Shankaran, D. R.; Kawaguchi, T.; Kim, S. J.; Matsumoto, K.; Toko, K.; Miura, N. *Anal. Bioanal. Chem.* **2006**, 108, 1313-1320.

(10) Brooke, D. N.; Crampton, M. R. *J. Chem. Soc., Perkin Trans. 2* **1982**, 231-237.

(11) Dasary, S. S. R.; Singh, A. K.; Senapati, D.; Yu, H.; Ray, P. C. *J. Am. Chem. Soc.* **2009**, 131, 13806-13812.

(12) Karasch, C.; Popovic, M.; Qasim, M.; Bajpai, R. K. *Appl. Biochem. Biotech.* **2002**, 98-100, 1173-1185.

(13) Ponnu, A.; Edwards, N. Y.; Anslyn, E. V. *New J. Chem.* **2008**, 32, 848-855.

(14) Harper, R. J.; Almirall, J. R.; Furton, K. G. *Talanta* **2005**, 67, 313-327.

(15) Sohn, H.; Sailor, M. J.; Magde, D.; Trogler, W. C. *J. Am. Chem. Soc.* **2003**, 125, 3821-3830.

(16) Naddo, T.; Che, Y.; Zhang, W.; Balakrishnan, K.; Yang, X.; Yen, M.; Zhao, J.; Moore, J. S.; Zang, L. *J. Am. Chem. Soc.* **2007**, 129, 6978-6979.

(17) Eastwood, D.; Fernandez, C.; Yoon, B. Y.; Sheaff, C. N.; Wai, C. M. *Appl. Spectrosc.* **2006**, 60, 958-963.

(18) Forzani, E. S.; Lu, D.; Leright, M. J.; Aguilar, A. D.; Tsow, F.; Inglesias, R. A.; Zhang, Q.; Lu, J.; Li, J.; Tao, N. *J. Am. Chem. Soc* **2009**, 131, 1390-1391.

(19) Rodriguez, M. C.; Monti, M. R.; Argarana, C. E.; Rivas, G. A. *Talanta* **2006**, 68, 1671-1676.

(20) Pinnaduwage, L. A.; Thundat, T.; Hawk, J. E.; Hedden, D. L.; Britt, P. F.; Houser, E. J.; Stepnowski, S.; McGill, R. A.; Bubb, D. *Sens. Actuators B* **2004**, 99, 223-229.

(21) Albert, K. J.; Myrick, M. L.; Brown, S. B.; James, D. L.; Milanovich, F. P.; Walt, D. R. *Environ. Sci. Technol.* **2001**, 35, 3193-3200.

(22) Masunaga, K.; Hayama, K.; Onodera, T.; Hayashi, K.; Miura, N.; Matsumoto, K.; Toko, K. *Sens. Actuators B* **2005**, 108, 427-434.

(23) Nie, D.; Li, P.; Zhang, D.; Zhou, T.; Liang, Y.; Shi, G. *Electrophoresis* **2010**, 31, 2981-2988.
(24) Saravanan, N. P.; Venugopalan, S.; Senthilkumar, N.; Santhosh, P.; Kavita, B.; Prabu, H. G. *Talanta* **2006**, 69, 656-662.
(25) Agüí, L.; Vega-Montenegro, D.; Yáñez-Sedeño, P.; Pingarrón, J. M. *Anal. Bioanal. Chem.* **2005**, 382, 381-387.
(26) Honeychurch, K. C.; Hart, J. P.; Pritchard, P. R. J.; Hawkins, S. J.; Ratcliffe, N. M. *Biosens. Bioelectron.* **2003**, 19, 305-312.
(27) Huang, M.-J.; Leszczynski, J. *J. Mol. Struct. (Theochem)* **2002**, 592, 105-113.
(28) Pearson, J. *Trans. Faraday Soc.* **1948**, 44, 683-697.
(29) Zhang, H.-X.; Zhang, J.-H. *Can. J. Chem.* **2011**, 89, 8-12.
(30) Zhang, H.-X.; Cao, A.-M.; Hu, J.-S.; Wan, L.-J.; Lee, S.-T. *Anal. Chem.* **2006**, 78, 1967-1971.
(31) Van Benschoten, J. J.; Lewis, J. Y.; Heineman, W. R.; Roston, D. A.; Kissinger, P. T. *J. Chem. Educ.* **1983**, 60, 702-706.
(32) Ives, D. J. G.; Janz, G. J. *Reference Electrodes: Theory and Applications*; Academic Press: New York, 1961.
(33) Izutsu, K. *Electrochemistry in Nonaqueous Solutions*; Wiley-VCH: New York, 2002.
(34) Gritzner, G.; Kuta, J. *Pure Appl. Chem.* **1984**, 56, 461-466.
(35) Stewart, G.; Kuntzleman, T. S.; Amend, J. R.; Collins, M. J. *J. Chem. Educ.* **2009**, 86, 1080-1081.
(36) Honeychurch, M. J.; Rechnitz, G. A. *Electroanalysis* **1998**, 10, 285-293.
(37) Honeychurch, M. J.; Rechnitz, G. A. *Electroanalysis* **1998**, 10, 453-457.
(38) Matsuda, H.; Ayabe, Y. *Z. Electrochem.* **1955**, 59, 494.
(39) Barrière, F.; LeSuer, R. J.; Geiger, W. E. In *Trends in Molecular Electrochemistry*; Pombeiro, A. J. L., Amatore, C., Eds.; Fontis Media, Marcel Dekker: 2004, p 413-444.
(40) Fujita, I.; Chang, C. K. *J. Chem. Educ.* **1984**, 61, 913.
(41) Ching, S.; Dudek, R.; Tabet, E. *J. Chem. Educ.* **1994**, 71, 602-605.
(42) Maloy, J. T. *J. Chem. Educ.* **1983**, 60, 285.
(43) Limon-Petersen, J. G.; Dickinson, E. J. F.; Belding, S. R.; Rees, N. V.; Compton, R. G. *J. Electroanal. Chem.* **2010**, 650, 135-142.
(44) Dickinson, E. J. F.; Limon-Petersen, J. G.; Rees, N. V.; Compton, R. G. *J. Phys. Chem. C* **2009**, 113, 11157-11171.
(45) Abbott, A. P.; Claxton, T. A.; Fawcett, J.; Harper, J. C. *J. Chem. Soc., Faraday Trans.* **1996**, 92, 1747-1749.
(46) Abbott, A. P.; Harper, J. C. *J. Chem. Soc., Faraday Trans.* **1996**, 92, 3895-3898.
(47) Geng, L.; Ewing, A. G.; Jernigan, J. C.; Murray, R. W. *Anal. Chem.* **1986**, 58, 852-860.
(48) Hill, M. G.; Lamanna, W. M.; Mann, K. R. *Inorg. Chem.* **1991**, 30, 4687-4690.

(49) Gladysz, J. A.; Curran, D. P.; Horváth, I. T. *Handbook of Fluorous Chemistry*; Wiley & Sons: New York, 2005.
(50) Boswell, P. G.; Bühlmann, P. *J. Am. Chem. Soc.* **2005**, 127, 8958–8959.
(51) Boswell, P. G.; Lugert, E. C.; Rábai, J.; Amin, E.; Bühlmann, P. *J. Am. Chem. Soc.* **2005**, 127, 16976-16984.
(52) LeSuer, R. J.; Geiger, W. E. *J. Electroanal. Chem.* **2006**, 594, 20-26.
(53) Boswell, P. G.; Szijjarto, C.; Jurisch, M.; Gladysz, J. A.; Rabai, J.; Bühlmann, P. *Anal. Chem.* **2008**, 80, 2084-2090.
(54) Chen, L. D.; Mandal, D.; Pozzi, G.; Gladysz, J. A.; Bühlmann, P. *J. Am. Chem. Soc.* **2011**, 133, 20869-20877.
(55) O'Neal, K. L.; Zhang, H.; Yang, Y.; Hong, L.; Lu, D.; Weber, S. G. *J. Chromatogr. A* **2010**, 1217, 2287-2295.
(56) Ohrenberg, C.; Geiger, W. E. *Inorg. Chem.* **2000**, 39, 2948-2950.
(57) Brady, J. E.; Carr, P. W. *Anal. Chem.* **1982**, 54, 1751-1757.
(58) Lo Nostro, P.; Scalise, L.; Baglioni, P. *J. Chem. Eng. Data* **2005**, 50, 1148-1152.
(59) Robinson, E. A.; Schreiber, H. D.; Spencer, J. N. *J. Phys. Chem.* **1971**, 75, 2219-2222.
(60) Ci, X.; Myers, A. B. *J. Phys. Chem.* **1992**, 96, 6433-6442.
(61) Oberg, K. A.; Palleros, D. R. *J. Chem. Educ.* **1995**, 72, 857-859.
(62) Lephart, J. O. *Appl. Spectrosc.* **1980**, 34, 702-704.
(63) Heineman, W. R. *Anal. Chem.* **1978**, 50, 390A-402A.
(64) Horváth, I. T.; Rábai, J. *Science* **1994**, 266, 72-75.
(65) Dass, A.; Guo, R.; Tracy, J. B.; Balasubramanian, R.; Dougla, A. D.; Murray, R. W. *Langmuir* **2008**, 24, 310-315.
(66) Laurence, C.; Nicolet, P.; Dalati, M. T. *J. Phys. Chem.* **1994**, 98, 5807-5816.
(67) Good, W. D.; Doublin, D. R.; Scott, D. W.; George, A.; Lacina, J. L.; Dawson, J. P.; Waddington, G. *J. Phys. Chem.* **1959**, 1133-1138.
(68) Wu, D.; Chen, A.; Johnson, C. S. *J. Magn. Reson., Ser A* **1995**, 115, 123-126.
(69) Xu, S.; Ballard, L.; Kim, Y. J.; Jonas, J. *J. Phys. Chem.* **1995**, 99, 5787-5792.
(70) Baker-Jarvis, J.; Janezic, M. D.; Jones, C. A. *IEEE Trans. Instrum. Meas.* **1998**, 47, 338-344.
(71) Gregory, A. P.; Clarke, R. N. *IEEE Trans. Dielectr. Insul.* **2006**, 13.
(72) Krupka, J.; Derzakowski, K.; Janezic, M. D.; Baker-Jarvis, J. In *2004 Conference on Precision Electromagnetic Measurements Digest* London, 2004, p 469-470.
(73) von Hippel, A. R. *Dielectric Materials and Applications*; The M.I.T. Press: Cambridge, MA, 1954.
(74) Arai, M.; Binner, J. G. P.; Cross, T. E. *Electron. Lett* **1995**, 31, 115-117.
(75) Clarke, R. N.; Gregory, A. P.; Cannell, D.; Patrick, M.; Wylie, S.; Youngs, I.; Hill, G. *A Guide to the Characterisation of Dielectric Materials at RF and Microwave Frequencies*; The Institute of Measurement and Control, National Physical Laboratory: London, 2003.

(76) Marsella, J. A.; Gilicinski, A. G.; Coughlin, A. M.; Pez, G. P. *J. Org. Chem.* **1992**, 57, 2856-2860.
(77) Pud, A. A.; Shapoval, G. S.; Kukhar, V. P.; Mikulina, O. E.; Gervits, L. L. *Electrochim. Acta* **1995**, 40, 1157-1164.
(78) Baranski, A. S.; Winkler, K.; Fawcett, W. R. *J. Electroanal. Chem.* **1991**, 313, 367-375.
(79) Pournaghi-Azar, H.; Ojani, R. *Electrochim. Acta* **1994**, 39, 953-955.
(80) Sun, P.; Mirkin, M. V. *Anal. Chem.* **2006**, 78, 6526-6534.
(81) Fawcett, W. R. *Can. J. Chem.* **1981**, 59, 1844-1853.
(82) Breiter, M.; Kleinerman, M.; Delahay, P. *J. Am. Chem. Soc.* **1958**, 80, 5111-5117.
(83) Fawcett, W. R.; Opallo, M. *Angewandte Chemie International Edition in English* **1994**, 33, 2131-2143.
(84) Marcus, R. A. *Annu. Rev. Phys. Chem.* **1964**, 15, 155-196.
(85) Pyati, R.; Murray, R. W. *J. Am. Chem. Soc.* **1996**, 118, 1743-1749.
(86) Fawcett, W. R.; Foss, C. A. *J. Electroanal. Chem.* **1989**, 270, 103-118.
(87) Frolich, H. *Theory of Dielectrics*; Oxford University Press: Oxford, 1949.
(88) Lifanova, N. V.; Usacheva, T. M.; Zhuravlev, V. I. *Zh. Fiz. Khim.* **1992**, 66, 237-240.
(89) Clegg, A. D.; Rees, N. V.; Klymenko, O. V.; Coles, B. A.; Compton, R. G. *J. Electroanal. Chem.* **2005**, 580, 78-86.
(90) Buchner, R.; Hefter, G. T.; May, P. M. *J. Phys. Chem. A* **2006**, 103, 1-9.
(91) Wakai, C.; Oleinikova, A.; Weingärtner, H. *J. Phys. Chem. B* **2006**, 110, 5824.
(92) Kaatze, U. *J. Solution Chem.* **2006**, 26, 1049-1112.
(93) Weingärtner, H. *Z. Phys. Chem.* **2006**, 220, 1395-1405.
(94) Lugert, E. C.; Lodge, T. P.; Bühlmann, P. *J. Polym. Sci., Part B: Polym. Phys.* **2008**, 46, 516-525.
(95) Lai, C.-Z.; Joyer, M. M.; Fierke, M. A.; Petkovich, N. D.; Stein, A.; Bühlmann, P. *J. Solid State Electrochem.* **2009**, 13, 123-128.
(96) Vincent, J.-M. *J. Fluorine Chem.* **2008**, 129, 903-909.
(97) Hjeresen, D. L.; Schutt, D. L.; Boese, J. M. *J. Chem. Educ.* **2000**, 77, 1543-1547.
(98) Marteel-Parrish, A. E. *J. Chem. Educ.* **2007**, 84, 245-247.
(99) Anastas, P. T.; Warner, J. C. *Green Chemistry: Theory and Practice*; Oxford University Press: New York, 1998.
(100) Mabbott, G. A. *J. Chem. Educ.* **1983**, 60, 697-702.
(101) Donato, R. K.; Migliorini, M. V.; Benvegnú, M. A.; Dupont, J.; Gonçalves, R. S.; Schrekker, H. S. *J. Solid State Electrochem.* **2007**, 11, 1481-1487.
(102) Ferreira, H. E. A.; Daniel, D.; Bertotti, M.; Richter, E. M. *J. Braz. Chem. Soc.* **2008**, 19, 1538-1545.
(103) Tur'yan, Y. I. *Talanta* **1997**, 44, 1-13.
(104) Maizels, M.; Seliskar, C. J.; Heineman, W. R.; Bryan, S. A. *Electroanalysis* **2002**, 14, 1345-1352.
(105) Kolthoff, I. M.; Tomsicek, W. J. *J. Phys. Chem.* **1935**, 39, 945-954.

(106) Pharr, C. M.; Griffiths, P. R. *Anal. Chem.* **1997**, 69, 4673-4679.
(107) Datta, M.; Datta, A. *J. Phys. Chem.* **1990**, 94, 8203-8207.
(108) Karyakin, A. A.; Karyakina, E. E. *Sens. Actuators B* **1999**, B57, 268-273.
(109) Karyakin, A. A.; Gitelmacher, O. V.; Karyakina, E. E. *Anal. Lett.* **1994**, 27, 2861-2869.
(110) Lefrou, C. *J. Electroanal. Chem.* **2006**, 592, 103-112.
(111) Bond, J. A.; Rickert, D. E. *Drug Metab. Disp.* **1981**, 9, 10-14.
(112) Moore, D. S. *Rev. Sci. Instrum.* **2004**, 75, 2499-2512.
(113) Yinon, J. *Trends Anal. Chem.* **2002**, 22, 292-300.
(114) Wang, D.; Chen, A.; Jang, S.-H.; Yip, H.-L.; Jen, A. K.-Y. *J. Mater. Chem.* **2011**, 21, 7269-7273.
(115) Terrier, F.; Xie, H.-Q.; Farrell, P. G. *J. Org. Chem* **1990**, 55, 2610-2616.
(116) Qureshi, P. M.; Andrabi, S. M. A.; Saeed, A.; Ahmad, A. *Anal. Proc.* **1995**, 32, 273-274.
(117) Hunt, A. L.; Yong, S. C. K.; Alder, J. F. *Anal. Commun.* **1996**, 33, 323-325.
(118) Andrabi, S. M. A.; Atehar, S. *Asian J. Chem.* **2002**, 14, 1077-1079.
(119) Artamkina, G. A.; Egorov, M. P.; Beletskaya, I. P. *Chem. Rev.* **1982**, 82, 427-459.
(120) Strauss, M. J. *Chem. Rev.* **1970**, 70, 667-712.
(121) Terrier, F. *Chem. Rev.* **1982**, 82, 78-152.
(122) Jackson, C. L.; Gazzolo, F. H. *Am. Chem. J.* **1900**, 23, 376-396.
(123) Meisenheimer, J. *Justus Liebigs Ann. Chem.* **1902**, 323, 205-246.
(124) Crampton, M. R.; Gold, V. *J. Chem. Soc. B* **1967**, 23-28.
(125) Foster, R.; Fyfe, C. A. *Tetrahedron* **1966**, 22, 1831-1842.
(126) Fyfe, C. A. *Can. J. Chem.* **1968**, 46, 3047-3054.
(127) Ryzhova, G. L.; Rubtsova, T. A.; Vasil'eva, N. A. *Zh. Obshch. Khim.* **1966**, 36, 2031-2035.
(128) Schaeppi, Y.; Treadwell, W. D. *Helv. Chim. Acta* **1948**, 31, 577-588.
(129) Chiavarino, B.; Crestoni, M. E.; Fornarini, S.; Lanucara, F.; Lemaire, J.; Maitre, P. *Angew. Chem.* **2007**, 46, 1995-1998.
(130) Chiavarino, B.; Crestoni, M. E.; Fornarini, S.; Lanucara, F.; Lemaire, J.; Maitre, P.; Scuderi, D. *Chem. Eur. J.* **2009**, 15, 8185-8195.
(131) Haderlein, S. B.; Weissmahr, K. W.; Schwarzenbach, R. P. *Environ. Sci. Technol.* **1996**, 30, 612-622.
(132) Gheorghiu, L.; Seitz, W. R.; Arbuthnot, D.; Elkind, J. L. *Proc. SPIE* **1999**, 3853, 296-302.
(133) Jenkins, T., F.; Walsh, M. E. *Talanta* **1992**, 39, 419-428.
(134) Otto, M. *Chemometrics: Statistics and Computer Application in Analytical Chemistry*; Wiley-VCH: New York, 1999.
(135) Job, P. *Ann. Chim.* **1928**, 9, 113-203.
(136) Bruneau, E.; Lavabre, D.; Levy, G.; Micheau, J. C. *J. Chem. Educ.* **1992**, 69, 833-837.
(137) Likussar, W.; Boltz, D. F. *Anal. Chem.* **1971**, 43, 1265-1272.

(138) Betts, R. H.; Michels, R. K. *J. Chem. Soc.* **1949**, S286-S294.
(139) Likussar, W. *Anal. Chem.* **1973**, 45, 1926-1931.
(140) Vosburgh, W. C.; Cooper, G. R. *J. Am. Chem. Soc.* **1941**, 63, 437-442.
(141) Kolthoff, I. M.; Chantooni, M. K.; Bhomik, S. *J. Am. Chem. Soc.* **1968**, 90, 23-28.
(142) Crampton, M. R.; Robotham, I. A. *J. Chem. Res. (S)* **1997**, 22-23.
(143) Bernasconi, C. F. *Acc. Chem. Res.* **1978**, 11, 147-152.
(144) Bernasconi, C. F.; Muller, M. C.; Schmid, P. *J. Org. Chem.* **1979**, 44, 3189-3196.
(145) Marenich, A. V.; Cramer, C. J.; Truhlar, D. G. *J. Phys. Chem. B* **2009**, 113, 6378-6396.
(146) Cramer, C. J. *Essentials of Computational Chemistry: Theories and Models*; 2nd ed.; John Wiley & Sons: Chinchester, 2004.
(147) Wiitala, K. W.; Hoye, T. R.; Cramer, C. J. *J. Chem. Theory Comput.* **2006**, 2, 1085-1092.
(148) Ho, J. M.; Coote, M. L. *Theor. Chem. Acc.* **2010**, 125, 3-21.
(149) Uchimiya, M. *Aquat. Geochem.* **2010**, 16, 547-562.
(150) Zhao, Y.; Truhlar, D. G. *Theor. Chem. Acc.* **2008**, 120, 215-241.
(151) Hehre, W. J.; Radom, L.; Schleyer, P. V. R.; Pople, J. A. *Ab Initio Molecular Orbital Theory*; Wiley: New York, 1986.
(152) Zerner, M. C. In *Rev. Comp. Chem.*; Lipkowitz, K. B., Boyd, D. B., Eds.; VCH: New York, 1991; Vol. 2, p 313-365.
(153) Kelly, C. P.; Cramer, C. J.; Truhlar, D. G. *J. Phys. Chem. A* **2006**, 110, 2493-2499.
(154) Kelly, C. P.; Cramer, C. J.; Truhlar, D. G. *J. Phys. Chem. B* **2007**, 111, 408-422.
(155) Frisch, M. J.; Trucks, G. W.; Schlegel, H. B.*et. al*; Gaussian, Inc.: Wallingford, CT, 2010.
(156) Ostromisslensky, L. *Ber. Dtsch. Chem. Ges.* **1911**, 44, 268-273.
(157) Denison, R. B. *Trans. Faraday Soc.* **1912**, 8, 20-34.
(158) Schalley, C. A. *Analytical Methods in Supramolecular Chemistry*; Wiley-VCH: Weinheim, 2007.
(159) Harvey, A. E.; Manning, D. L. *J. Am. Chem. Soc* **1950**, 72, 4488-4493.
(160) Yoe, J. H.; Jones, A. L. *Ind. Eng. Chem. Anal. Ed.* **1944**, 16, 111-115.
(161) Hirose, K. *J. Incl. Phenom. Macro.* **2001**, 39, 193-209.
(162) Sayago, A.; Boccio, M.; Asuero, A. G. *Int. J. Pharm.* **2005**, 295, 29-34.
(163) Sayago, A.; Asuero, A. G. *Int. J. Pharm.* **2006**, 321, 94-100.
(164) Facchiano, A.; Ragone, R. *Anal. Biochem.* **2003**, 313, 170-172.
(165) Purohit, D. N.; Goswami, A. K.; Chauhan, R. S.; Ressalan, S. *Asian. J. Chem.* **1999**, 11, 123-129.
(166) Gil, V. M. S.; Oliveira, N. C. *J. Chem. Educ.* **1990**, 67, 473-478.
(167) Liou, L. R.; McNeil, A. J.; Ramirez, A.; Toombes, G. E. S.; Gruver, J. M.; Collum, D. B. *J. Am. Chem. Soc.* **2008**, 130, 4869-4888.
(168) Boccio, M.; Sayago, A.; Asuero, A. G. *Int. J. Pharm.* **2006**, 318, 70-77.
(169) Blanda, M. T.; Horner, J. H.; Newcomb, M. *J. Org. Chem.* **1989**, 54, 4626-4636.

(170) Klausen, K. S.; Langmyhr, F. J. *Anal. Chim. Acta* **1963**, 28, 355-340.
(171) Loontiens, F. G.; Regenfuss, P.; Zechel, A.; Dumortier, L.; Clegg, R. M. *Biochemistry* **1990**, 29, 9029-9039.
(172) O'Neal, K. L.; Geib, S.; Weber, S. G. *Anal. Chem.* **2007**, 79, 3117-3125.
(173) Schmuck, C.; Schwegmann, M. *J. Am. Chem. Soc.* **2005**, 127, 3373-3379.
(174) Heller, J.; Schwarzenbach, G. *Helv. Chim. Acta* **1951**, 34, 1876-1889.
(175) Likussar, W. *Anal. Chem.* **1973**, 45, 1926-1931.
(176) Olson, E. J.; Xiong, T. T.; Cramer, C. J.; Bühlmann, P. *J. Am. Chem. Soc.* **2011**, 133, 12858-12865.
(177) Qiao, Y.-H.; Lin, H.; Lin, H.-K. *Can. J. Chem.* **2006**, 84, 1155-1158.
(178) Perez-Casas, C.; Yatsimirsky, A. K. *J. Org. Chem.* **2008**, 73, 2275-2284.
(179) Phillips, K. N.; Lantz, C.; Buhlmann, P. *Electroanalysis* **2005**, 17, 2019-2025.
(180) Koseoglu, S. S.; Lai, C.-Z.; Ferguson, C.; Buhlmann, P. *Electroanalysis* **2008**, 20, 331-339.
(181) Krausa, M.; Doll, J.; Schorb, K.; Böke, W.; Hambitzer, G. *Propellants, Explosives, Pyrotechnics* **1997**, 22, 156-159.
(182) Harper, R. J.; Almirall, J. R.; Furton, K. G. *Talanta* **2005**, 67, 313-327.
(183) Phelan, J. M.; Barnett, J. L. *Proceedings of SPIE* **2002**, 4742, 532-543.
(184) Zhang, H.-X.; Cao, A.-M.; Hu, J.-S.; Wan, L.-J.; Lee, S.-T. *Anal. Chem.* **2006**, 78, 1967-1971.
(185) Bratin, K.; Kissinger, P. T.; Briner, R. C.; Bruntlett, C. S. *Anal. Chim. Acta* **1981**, 130, 295-311.
(186) Smith, W. H.; Bard, A. J. *J. Am. Chem. Soc.* **1975**, 97, 5203-5210.
(187) Cyr, A.; Hout, P.; Marcoux, J.-F.; Belot, G.; Laviron, E.; Lessard, J. *Electrochim. Acta* **1989**, 34, 439-445.
(188) Geske, D. H.; Maki, A. H. *J. Am. Chem. Soc.* **1960**, 82, 2671-2676.
(189) Carre, B.; Belin, P. *C. R. Acad. Sci.* **1973**, 276, 1365-1368.
(190) Zuman, P.; Fijalek, Z.; Dumanovic, D.; Suznjevic, D. *Electroanalysis* **1992**, 4, 783-794.
(191) Macias-Ruvalcaba, N. A.; Evans, D. H. *J. Phys. Chem. B* **2005**, 109, 14642-14647.
(192) Fry, A. J. *J. Electroanal. Chem.* **2003**, 546, 35-39.
(193) Chua, C. K.; Pumera, M.; Rulíšek, L. *The Journal of Physical Chemistry C* **2012**, 116, 4243-4251.
(194) Ciordano, M. C.; Macagno, V. A.; Sereno, R. *An. Asoc. Quim. Argent.* **1977**, 65, 71-84.
(195) Barrette, W. C.; Johnson, H. W.; Sawyer, D. T. *Anal. Chem.* **1984**, 56, 1890-1898.
(196) Barrows, S. E.; Cramer, C. J.; Truhlar, D. G.; Elovitz, M. S.; Weber, E. J. *Environ. Sci. Technol.* **1996**, 30, 3028-3038.
(197) Yinon, J. *Trends Anal. Chem.* **2002**, 21, 292–301.
(198) Forzani, E. S.; Lu, D.; Leright, M. J.; Aguilar, A. D.; Tsow, F.; Iglesias, R. A.; Zhang, Q.; Lu, J.; Li, J.; Tao, N. *J. Am. Chem. Soc.* **2009**, 131, 1390–1391.

(199) Masunaga, K.; Hayama, K.; Onodera, T.; Hayashi, K.; Miura, N.; Matsumoto, K.; Toko, K. *Sens. Actuators, B* **2005**, 108, 427–434.
(200) Lehn, J.-M. *Supramolecular Chemistry: Concepts and Perspectives*; Wiley-VCH: Weinheim, 1995.
(201) Yang, X.; Du, X.-X.; Shi, J.; Swanson, B. *Talanta* **2001**, 54, 439-445.
(202) Ergang, N. S.; Fierke, M. A.; Wang, Z.; Smyrl, W. H.; Stein, A. *J. Electrochem. Soc.* **2007**, 154, A1135–A1139.
(203) Wang, Z.; Fierke, M. A.; Stein, A. *J. Electrochem. Soc.* **2008**, 155, A658-A663.
(204) Fierke, M. A.; Lai, C.-Z.; Bühlmann, P.; Stein, A. *Anal. Chem.* **2010**, 82, 680-688.
(205) Lai, C.-Z.; Fierke, M. A.; Stein, A.; Bühlmann, P. *Anal. Chem.* **2007**, 79, 4621-4626.
(206) Zhang, T.; Lai, C.-Z.; Fierke, M. A.; Stein, A.; Bühlmann, P.; The Pittsburgh Conference: Orlando, 2012.
(207) Bühlmann, P.; Nishizawa, S.; Xiao, K. P.; Umezawa, Y. *Tetrahedron* **1997**, 53, 1647-1654.
(208) Delamar, M.; Hitmi, R.; Pinson, J.; Savéant, J.-M. *J. Am. Chem. Soc.* **1992**, 114, 5883–5884.
(209) Allongue, P.; Delamar, M.; Desbat, B.; Fagebaume, O.; Hitmi, R.; Pinson, J.; Savéant, J.-M. *J. Am. Chem. Soc.* **1997**, 119, 201-207.
(210) Nishida, H.; Takada, N.; Yoshimura, M.; Sonoda, T.; Kobayashi, H. *Bull. Chem. Soc. Jpn.* **1984**, 57, 2600–2604.
(211) Yakelis, N. A.; Bergman, R. G. *Organometallics* **2005**, 24, 3579-3581.
(212) Hill, M. G.; Lamanna, W. M.; Mann, K. R. *Inorg. Chem.* **1991**, 30, 4687–4690.
(213) Saby, C.; Ortiz, B.; Champagne, G. Y.; Bélanger, D. *Langmuir* **1997**, 13, 6805–6813.
(214) Liu, Y.-C.; McCreery, R. L. *J. Am. Chem. Soc.* **1995**, 117, 11254-11259.
(215) Yu, S. S. C.; Tan, E. S. Q.; Jane, R. T.; Downard, A. J. *Langmuir* **2007**, 23, 11074-11082.
(216) Hurley, B. L.; McCreery, R. L. *J. Electrochem. Soc.* **2004**, 151, B252-B259.
(217) D'Amours, M.; Bélanger, D. *J. Phys. Chem. B* **2003**, 107, 4811–4817.
(218) Doppelt, P.; Hallais, G.; Pinson, J.; Podvorica, F.; Verneyre, S. *Chem. Mater.* **2007**, 19, 4570-4575.
(219) Brooksby, P. A.; Downard, A. J. *J. Phys. Chem. B* **2005**, 109, 8791-8798.
(220) Ortiz, B.; Saby, C.; Champagne, G. Y.; Belanger, D. *J. Electroanal. Chem.* **1998**, 455, 75-81.
(221) Boehm, H. P. In *Graphite and Precursors*; Delhaes, P., Ed.; Gordon and Breach Science Publishers: Amsterdam, The Netherlands, 2001; Vol. 1, p 141-178.
(222) Prest, J. W. M.; Mosher, R. A. In *Colloids and Surfaces in Reprographic Technology*; Hair, M., Croucher, M. D., Eds.; American Chemical Society: Washington, 1982, p 225-247.
(223) Liu, L.; Qin, Y.; Guo, Z.-X.; Zhu, D. *Carbon* **2003**, 41, 331-335.
(224) Sainsbury, T.; Fitzmaurice, D. *Chem. Mater.* **2004**, 16, 3780-3790.

(225) Shaffer, M. S. P.; Fan, X.; Windle, A. H. *Carbon* **1998**, 36, 1603-1612.
(226) Pretsch, E.; Bühlmann, P.; Badertscher, M. *Structure Determination of Organic Compounds: Tables of Spectral Data*; 4 ed.; Springer: Berline, 2009.
(227) Silverstein, R. M.; Webster, F. X. *Spectrometric Identification of Organic Compounds*; 6 ed.; John Wiley & Sons, Inc.: Hoboken, 1998.
(228) Zhang, H.-X.; Zhang, J.-H. *Can. J. Chem.* **2011**, 89, 8–12.
(229) Zang, J.; Guo, C. X.; Hu, F.; Yu, L.; Li, C. M. *Anal. Chim. Acta* **2011**, 683, 187–191.
(230) Fry, A. J. *J. Electroanal. Chem.* **2003**, 546, 35–39.
(231) Helfrick, J. J. C.; Bottomley, L. A. *Anal. Chem.* **2009**, 81, 9041–9047.
(232) O'Dea, J. J.; Osteryoung, J.; Lane, T. *The Journal of Physical Chemistry* **1986**, 90, 2761-2764.
(233) O'Dea, J. J.; Osteryoung, J.; Osteryoung, R. A. *J. Phys. Chem.* **1983**, 87, 3911–3918.
(234) O'Dea, J. J.; Osteryoung, J.; Osteryoung, R. A. *Anal. Chem.* **1981**, 53, 695-701.
(235) O'Dea, J. J.; Wikiel, K.; Osteryoung, J. *J. Phys. Chem.* **1990**, 94, 3628–3636.
(236) Chuang, M.-C.; Windmiller, J. R.; Santhosh, P.; Ramírez, G. V.; Galik, M.; Chou, T.-Y.; Wang, J. *Electroanalysis* **2010**, 22, 2511-2518.
(237) Bozic, R. G.; West, A. C.; Levicky, R. *Sens. Actuators, B* **2008**, 133, 509–515.
(238) Osteryoung, J. G.; Osteryoung, R. A. *Anal. Chem.* **1985**, 57, 101A-110A.
(239) Ue, M.; Takeda, M.; Takehara, M.; Mori, S. *J. Electrochem. Soc.* **1997**, 144, 2684-2688.
(240) Ue, M.; Ida, K.; Mori, S. *J. Electrochem. Soc.* **1994**, 141, 2989-2996.
(241) Ue, M. *Electrochim. Acta* **1994**, 39, 2083-2087.
(242) Yang, Z.; Li, W.; Yu, S.; Zhang, N.; Gu, N.; Zhang, R.; Gao, L. *Z. Phys. Chem* **2009**, 223, 1437-1449.
(243) Xu, K.; Ding, M. S.; Jow, T. R. *J. Electrochem. Soc.* **2001**, 148, A267-A274.
(244) Maeshima, H.; Moriwake, H.; Kuwabara, A.; Fisher, C. A. J. *J. Electrochem. Soc.* **2010**, 157, A696.
(245) Kötz, R.; Carlen, M. *Electrochim. Acta* **2000**, 45, 2483-2498.
(246) Devarajan, T.; Higashiya, S.; Dangler, C.; Rane-Fondacaro, M.; Snyder, J.; Haldar, P. *Electrochem. Commun.* **2009**, 11, 680-683.
(247) Huggins, R. A. *Solid State Ionics* **1996**, 86–88, Part 1, 41-48.
(248) O'Mahony, A. M.; Silvester, D. S.; Aldous, L.; Hardacre, C.; Compton, R. G. *J. Chem. Eng. Data* **2008**, 53, 2884-2891.
(249) Buzzeo, M. C.; Hardacre, C.; Compton, R. G. *Chemphyschem* **2006**, 7, 176-180.
(250) Barrosse-Antle, L. E.; Bond, A. M.; Compton, R. G.; O'Mahony, A. M.; Rogers, E. I.; Silvester, D. S. *Chem Asian J* **2010**, 5, 202-230.
(251) Simonet, J.; Astier, Y.; Dano, C. *J. Electroanal. Chem.* **1998**, 451, 5-9.
(252) Zhou, Z.-B.; Matsumoto, H.; Tatsumi, K. *Chem. Eur. J.* **2005**, 11, 752-766.
(253) Zhou, Z.-B.; Matsumoto, H.; Tatsumi, K. *Chem. Eur. J.* **2006**, 12, 2196-2212.

(254) Wu, T.-Y.; Su, S.-G.; Wang, H. P.; Lin, Y.-C.; Gung, S.-T.; Lin, M.-W.; Sun, I.-W. *Electrochim. Acta* **2011**, 56, 3209-3218.
(255) Wu, T.-Y.; Su, S.-G.; Lin, K.-F.; Lin, Y.-C.; Wang, H. P.; Lin, M.-W.; Gung, S.-T.; Sun, I.-W. *Electrochim. Acta* **2011**, 56, 7278-7287.
(256) Eggert, G.; Heitbaum, J. *Electrochim. Acta* **1986**, 31, 1443-1448.
(257) Guilbault, G. G.; Durst, R. A.; Frant, M. S.; Freiser, H.; Hansen, E. H.; Light, T. S.; Pungor, E.; Rechnitz, G.; Rice, N. M.; Rohm, T. J.; Simon, W.; Thomas, J. D. R. *Pure Appl. Chem.* **1976**, 48, 127-132.
(258) Lindner, E.; Umezawa, Y. *Pure Appl. Chem.* **2008**, 80, 85-104.
(259) Ong, S. P.; Andreussi, O.; Wu, Y.; Marzari, N.; Ceder, G. *Chem. Mater.* **2011**, 23, 2979-2986.
(260) Zhou, Z. B.; Matsumoto, H.; Tatsumi, K. *Chem. Eur. J.* **2005**, 11, 752-766.
(261) Haubold, W.; Herdtle, J.; Gollinger, W.; Einholz, W. *J. Organomet. Chem.* **1986**, 315, 1-8.